UNIVERSITY OF CALIFORNIA, SAN DIEGO

Compressed Gas Solvent Based Electrolytes for Electrochemical Energy Storage Devices

A dissertation submitted in partial satisfaction of the
requirements for the degree

in

Materials Science and Engineering

by

Cyrus Sam Rustomji

Committee in charge:

Professor Sungho Jin, Chair
Professor Ying Shirley Meng, Co-Chair
Professor Prabhakar Rao Bandaru
Professor Olivia A. Graeve
Professor Yu Qiao

2015

The dissertation of Cyrus Sam Rustomji is approved, and it is acceptable in quality and form for publication on microfilm and electronically:

_____

_____

_____

_____
Co-Chair

_____
Chair

University of California, San Diego

2015

DEDICATION

To the cosmos, which has bred my curiosity for science, appreciation for nature's beauty, and my humility amongst them...

...to my family and friends, to who I owe an insurmountable debt of gratitude...

...and to beer, which has helped maintain my sanity throughout it all.

Cheers.

EPIGRAPH

You know you're in love when you can't fall asleep

because reality is finally better than your dreams.

—Dr. Seuss

TABLE OF CONTENTS

LIST OF FIGURES

LIST OF TABLES

ACKNOWLEDGEMENTS

Thanks to Tae Kyoung Kim, Jimmy Mac, Duyoung Choi, Chulmin Choi, Youngjin Kim, Elizabeth Caldwell, Professor Shirley Meng and Professor Sungho Jin for their direct involvement and much appreciated help, discussions and support for the project.

I would like to acknowledge Jimmy Mac, Chulmin Choi, Tae Kyoung Kim, Duyoung Choi, Ying Shirley Meng and Sungho Jin, who helped co-author the material that has been acceted for publication in Chapter 3 to the Journal of Applied Electrochemistry under the title "Thin-Film Electrochemical Sensor Electrode for Rapid Evaluation of Electrolytic Conductivity, Cyclic Voltammetry and Temperature Measurements". Further, I acknowledge financial support of this work by DOE ARPA-E Grant No. DE-AR0000379 and by Iwama Fund at UC San Diego and helpful discussions and fabrication assistance with the Nano3 Cleanroom staff Sean Parks and Ivan Harris at UC San Diego.

Thanks also to my doctoral committee, the UC San Diego Nano3 cleanroom staff Sean Parks and Ivan Harris at UC San Diego for their help in electrode fabrication, Frank Doljack, Kyle Kim, Peter So, Chad Johns and Hundi Kamath for their technical guidance and support, and to my friends and family for the laughs and kicks in the ass.

VITA

2015	Ph. D. in Material Science and Engineering, University of California, San Diego
2013-2015	Graduate Student Researcher, University of California, San Diego
2013-2014	Material Scientist, Space Micro
2010-2013	Material Scientist and Development Engineer, Cooper Bussmann
2007-2010	Graduate Student Researcher, University of California, San Diego
2008	M. S. in Material Science and Engineering, University of California, San Diego
2007	B. S. in Physics, University of California, Los Angeles
2005-2007	Undergraduate Research Assistant, University of California, Los Angeles

PUBLICATIONS

Cyrus S. Rustomji, Jimmy Mac, Chulmin Choi, Tae Kyoung Kim, Duyoung Choi, Ying Shirley Meng, Sungho Jin, "Thin-Film Electrochemical Sensor Electrode for Rapid Evaluation of Electrolytic Conductivity, Cyclic Voltammetry and Temperature Measurements", *Journal of Applied Electrochemistry*, accepted.

Rustomji, Cyrus S., et al. "Dye-Sensitized Solar Cell Constructed with Titanium Mesh and 3-D Array of TiO_2 Nanotubes", *The Journal of Physical Chemistry B* 114.45 (2010): 14537-14543.

ABSTRACT OF THE DISSERTATION

Compressed Gas Solvent Based Electrolytes for Electrochemical Energy Storage Devices

by

Cyrus Sam Rustomji

Doctor of Philosophy in Materials Science and Engineering

University of California, San Diego, 2015

Professor Sungho Jin, Chair
Professor Ying Shirley Meng, Co-Chair

The use of fluorinated compressed gas solvent based electrolytes for electrochemical energy storage devices is explored. These solvents have the potential to offer batteries and electrochemical double-layer capacitors significantly improved properties including higher voltage, higher power and wider operating temperature range. A thorough study of the conductivity and potential window behavior of a number of electrolytes has been done as well as exploration into the chemical reduction of these solvents. Using these

data, both battery and electrochemical double-layer capacitor devices were fabricated. The devices show exceptional behavior down to -70 °C with equal or improved energy densities. These results warrant a much wider exploration of the use of these solvents in next generation electrochemical energy storage devices.

Chapter 1

Electrochemical Energy Storage Device Fundamentals

Fundamentals of electrochemical energy storage devices, batteries and electrocehmical double-layer capacitors, are discussed. In particular, their similarities, differences, and the fundamental physics and chemistry behind what gives them their properties.

1.1 Energy Generation and Electrochemical Energy Storage

Since the 1800s, modern civilization has been manipulating the electron for practical use. Early examples include the light bulb and the electrical telegraph for rapid communication over vast distances. Electricity generation has been in use just as long,

typically involving transferring kinetic energy (ex. using steam from boiling water to turn a turbine) into electricity via electromagnetic induction. Other types of electricity generation, or ”renewable energy”, are generated from wind or radiation from the sun. With a deepening global crisis with climate change as a result of our dependence on the now diminishing supplies of fossil fuels, a push toward clean renewable energy is urgent.

With the increase in intermittent energy generation from renewable energy sources, a looming question of how to store this energy for when it is needed requiress a solution and, as it turns out, history has shown energy generation is much easier than energy storage. The types of energy storage devices are also numerous and range from pumped-storage hydroelectricity to flywheel energy storage with varying degrees of efficiency and cost.

Important energy storage technologies for mobile electronics and the rapidly emerging electric vehicle are electrochemical energy storage devices such as the battery and electrochemical double-layer capacitors (EDLCs). Both devices have many similarities and differences. Both devices utilize two electrodes to store electrical energy and an electrolyte solution to carry charge from one electrode to the other. Both utilize many of the same material technologies, such as current collectors, binder materials, separators, cell housings, and fabrication technologies such as electrode coating, mixing, welding of connections. However, the fundamental storage mechanism of both batteries and electrochemical capacitors are actually quite different.

1.1.1 Batteries

Batteries converts chemical energy contained in its active materials directly into electric energy by means of an electrochemical oxidation-reduction (redox) reaction [14]. This occurs via positively charged ion transfer from (deintercalation) one electrode and ion transfer into (intercalation) the opposite electrode, as seen in Fig 1.1. When this positively charged ion intercalates into an electrode, the charge must be balanced by a negatively charged electron entering the electrode. The electrode allows addition of this negative charge into the lattice often by means of reduction of a metallic atom, such as nickel, cobalt, magnesium, etc., to a lower oxidation state which is contained in the electrode material. The reduction of the metal lowers the overall potential of the electrode. Similarly, when the positively charged ion leaves an electrode material, a negatively charged electron also leaves to balance the overall charge, then the metallic atom is oxidized, raising the potential of the electrode in the process [17]. By pairing two electrodes together into an electrochemical cell and transferring ions from one to the other, one may increase (charge) and decrease (discharge) the cell voltage routinely (if the electrodes allow) in a rechargeable secondary battery. Commonly used ions for this type of reaction are positively charged protons or lithium ions, although sodium, magnesium, aluminum and others are also at some stage of development or use [18–20]. For the use of proton transfer, aqueous (acidic or basic) electrolytes are commonly used while the transfer of other ions typically use organic solvents.

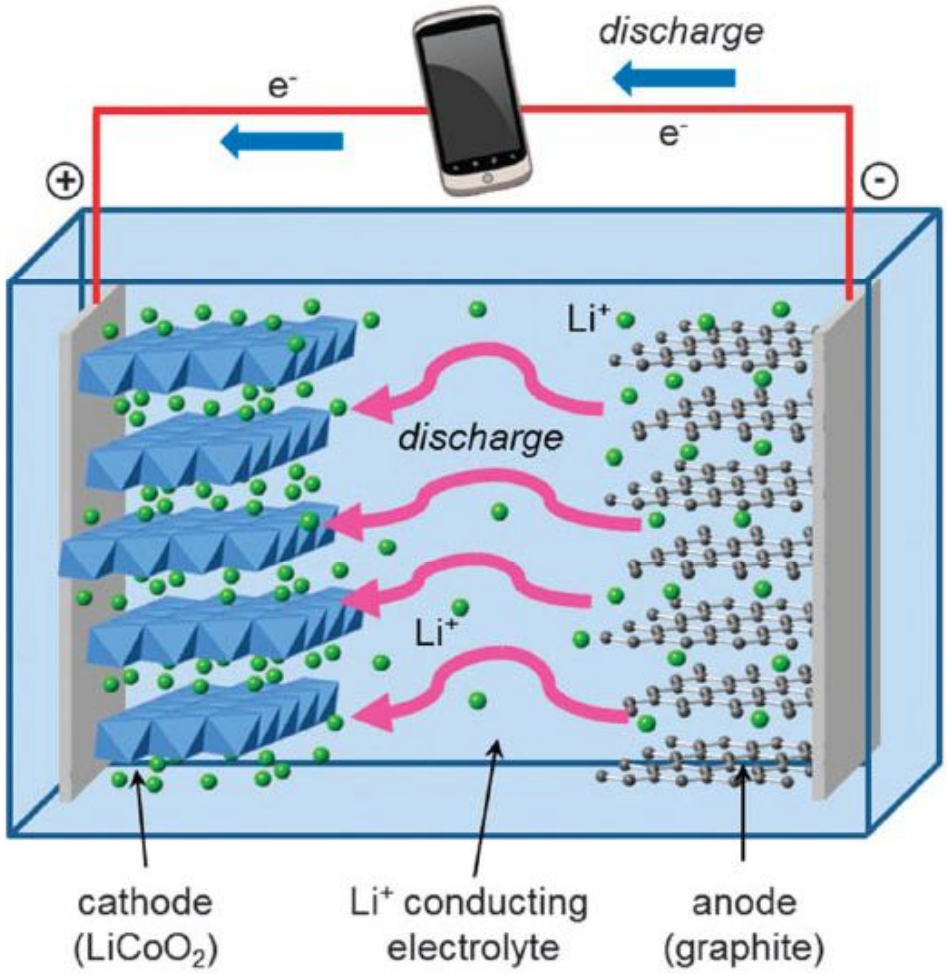

Figure 1.1: Schematic diagram of Li-Ion battery, showing flow of Li^+ cations and electrons during discharge [1].

The energy density of battery devices is given by

$$E = C \cdot V \tag{1.1}$$

where the E is the energy in Wh, C is the capacity in Ah and V is the nominal voltage of the device. The device capacity is essentially how much charge can be stored in the electrode material and the limiting electrode varies from technology to technology. The primary reason batteries have the ability to store so much energy is that intercalation ions

are stored within the bulk of the material, hence the entire volume of the active material is utilized to store energy. The cell voltage is determined by the redox potential of both anode and cathode and often changes by many hundreds of mili-volts through charge and discharge. Because the thermodynamic potential window of water is only 1.23 V, these aqueous based devices have a limited voltage. Higher voltages >2 V require use of organic solvent systems, which are commonly found in lithium-ion batteries. As seen in Table 1.1, since both aqueous and organic based technologies have similar capacities, the voltage of the device makes a significant difference in the overall energy density of the technology.

Table 1.1: Select secondary battery technologies and their capacity and energy densities. [14]

Anode	Cathode	Electrolyte	Cell Voltage V	Capacity Density $Ah \cdot kg^{-1}$	Energy Density $Wh \cdot kg^{-1}$
Pb	PbO	aqueous	2.0	120	70
Zn	AgO	aqueous	1.5	283	180
MH	NiOOH	aqueous	1.2	178	240
Li	MnO_2	organic	3.0	286	265
Li_xC_6	$Li_{(1-x)}CoO_2$	organic	4.1	100	400

1.1.2 Electrochemical Capacitors

Unlike batteries which store charge via a redox reaction, electrochemical capacitors store charge via an electrostatic attraction between charges at the electrode surface (electrons or holes) and oppositely charged ions within the electrolyte solution, shown in Fig. 1.2. Since these electrostatic bonds are very easy to form and break, charge and discharge can occur very rapidly and devices show very high power densities. Further, because there is no mechanical stress due to ionic intercalation seen in batteries, devices show extremely long cycle lives. However, because only the surface of the electrode is utilized to store charge, the volume of the electrode material goes unused and the overall energy density of the device is significantly lower than conventional batteries. Because of this, electrodes of very high surface area are required. Activated carbon, having a surface area of 2000-3000 $m^2 \cdot g^{-1}$ [21] is commonly used in commercial devices, however other carbons such as carbon nanotubes and carbon aerogels are also possibilities. Activated carbon, however, has many surface groups, considered impurities, which act as centers for charge transfer at high enough voltage, leading to significant leakage current. [2, 22].

The energy of electrochemical capacitors is given by

$$E = \frac{1}{2} \cdot C \cdot V^2 \tag{1.2}$$

where E is the energy in Joules, C is the capacitance in Farads and V is the voltage of the device. Since the energy goes as V^2, there is a big effort to increase the voltage of these devices in order to increase energy density. Because of "dirty" surface groups

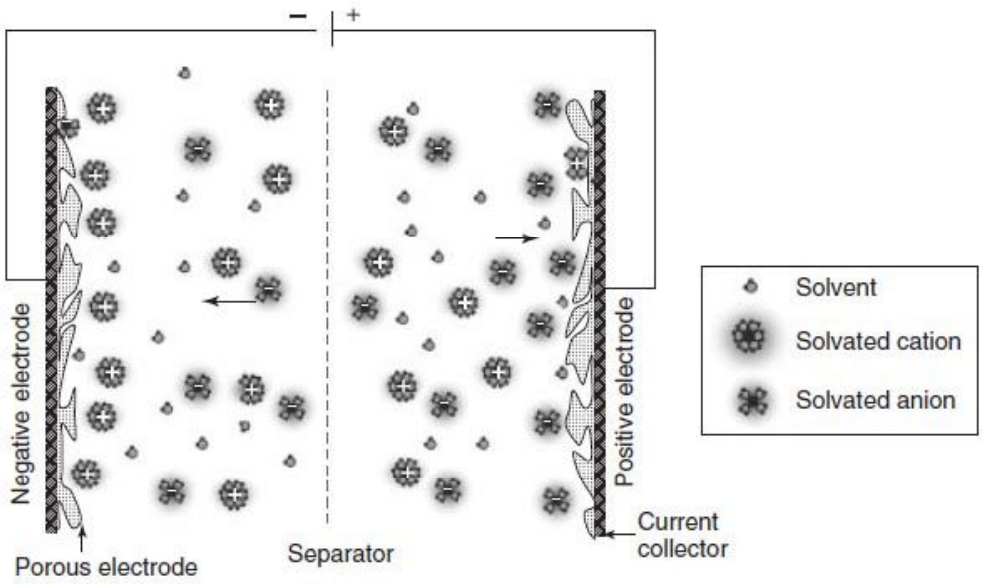

Figure 1.2: Schematic diagram of electrochemical capacitor [2].

commonly seen on activated carbon and the potential limit of the electrolytes used, the overall voltage of devices based on organic solvents is typically limited to 2.7 V, as seen in Table 1.2. If the voltage is able to match those of battery devices (ca. 4 V), a single electrochemical capacitor and battery may be placed in parallel as a hybrod device, offering excellent power and energy densities for numerous applications.

Table 1.2: Activated carbon based electrochemical capacitor based on aqueous or organic electrolytes and their capacitance and energy densities. [2]

Electrolyte	Cell Voltage /V	Capacitance F	Device Energy Density /Wh·kg^{-1}
aqueous	0.9	300	4
organic	2.7	125	8

1.2 Conclusion

Batteries and electrochemical capacitors are both essential electrochemical energy storage technologies to today's demanding applications. Both have similarities and many differences. The most obvious differences are the power and energy densities of the devices, which are compared wth various technologies as a Ragone plot in Fig. 1.3. Both technologies supplement each other in many applications; the long life and high power of EDLCs could aid batteries who's energy density and life suffers from high power output.

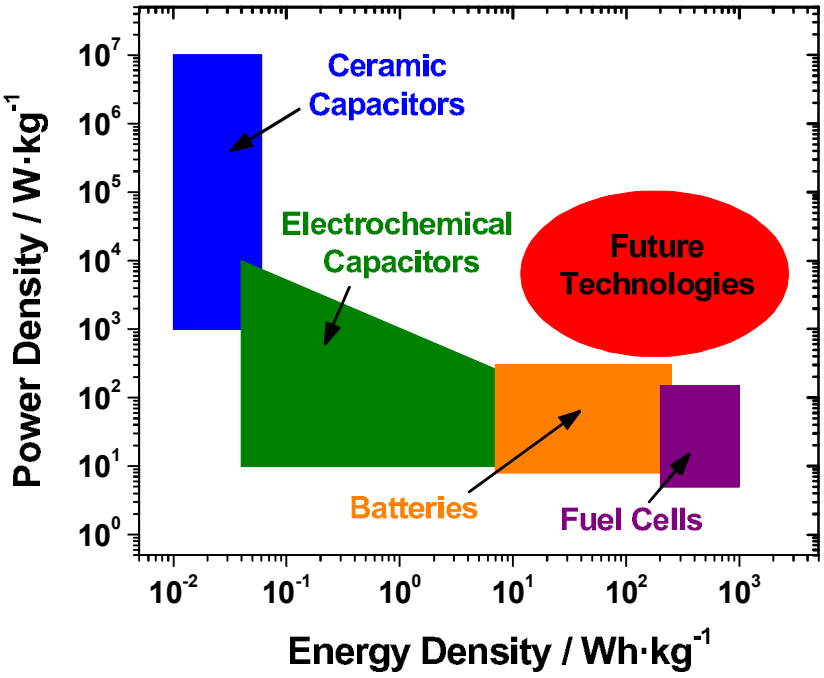

Figure 1.3: Ragone plot of energy storage devices.

One of the primary limitations of both technologies is the energy density for future applications such as automotives. It is generally agreed the electrolyte is limiting

the numerous electrodes available in both technologies. An elecvtrolyte with a wider range of potential stability could enable the use of high voltage device operation. In Chapter 2, the fundamental limitations of the electrolyte is discussed as well as possible pathways to improvement.

Chapter 2

Electrolytes Based on Compressed Gas Solvents

Conventionally used organic liquid solvents are commonly limited in their conductivity, potential window or temperature range. Further, the formation of a suitable solid-electrolyte interphase is an important requirement in lithium-ion batteries. No single solvent has been found to meet all these requirements and often more than one solvent, and smaller amounts of additives, are used to achieve desired device performance. Proposed here is a new class of electrolytes based on fluorinated compressed gas solvents which have the potential to meet these demanding requirements of electrochemical energy storage devices.

2.1 Introduction

Conventionally used organic liquid solvents are commonly limited in their conductivity, potential window or temperature range. Further, the formation of a suitable solid-electrolyte interphase is an important requirement in lithium-ion batteries. No single solvent has been found to meet all these requirements and often more than one solvent, and smaller amounts of additives, are used to achieve desired device performance. Proposed here is a new class of electrolytes based on fluorinated compressed gas solvents which have the potential to meet these demanding requirements of electrochemical energy storage devices. These solvents contain only strong C-F and C-H bonds, rendering the solvent both oxidation and reduction resistant. Further, viscosities are very low, lending themselves to high conductivity electrolytes. Lastly, melting points of these solvents are all $<$-100 °C, yielding devices that would have very low operating temperatures.

2.2 Conventional Organic Solvents

There are numerous anode and cathode materials with varying capacity and electrochemical potentials, however, it is generally accepted that the electrolyte limits adoption of many of these materials due to electrolyte decomposition. Though the electrolyte's salts have their own limitations, it is the solvent that typically limits the voltage which a device may operate at. Since energy is directly proportional to voltage, it is a primary goal of electrochemical energy storage device research to improve the solvent's electrochemical window to allow for increased voltages.

Many solvents offer a wide electrochemical potential window of stability, however, these solvents must simultaneously meet five primary requirements: [23]

1. Form highly conductive electrolyte solutions
2. High chemical stability
3. Wide electrochemical potential window for high stability
4. Wide temperature range
5. High safety

Among hundreds of conventional, and some specially synthesized solvents, none meet all these requirements. For instance, in electrochemical double-layer capacitors (EDLCs), two primary electrolytes are used; those based on propylene carbonate and those based on acetonitrile. Propylene carbonate is a safe, non-toxic solvent but offers limited conductivity, lower voltage devices and limited temperature range. Acetonitrile is a highly flammable and toxic solvent but offers exceptionally high conductivity, higher voltage devices, and operating temperatures as low as -40 °C, which is a common requirement for EDLC applications. Lithium-ion batteries (LiBs) have much more stringent solvent requirements than EDLCs, in that they must also form a highly stable, electrically insulating and Li^+ cation conductive solid electrolyte interface (SEI) with the anode and/or cathode. These SEI layers were first described by Peled et. al. [24] regarding the reduction of organic solvents on the surface of lithium metal creating a thin electrically insulating layer on the lithium metal to prevent further chemical reduction of the solvent.

As an example regarding the SEI requirement of solvents, early lithium-ion research dealt almost exclusively with the use of propylene carbonate as a non-aqueous solvent for lithium-ion batteries. However, due to the co-intercalation and eventual decomposition of this solvent on a carbon anode [3], high cyclability was never achieved. High efficiency for lithium intercalation and de-intercalation for a graphite anode was finally realized using a 1:1 mixture of propylene carbonate and ethylene carbonate mixture [25]. It was found that ethylene carbonate forms a solid electrolyte interphase with graphite that covers the entire graphite surface. Further, this interphase is both electrically insulating and ionically conducting, allowing passage of Li^+ cations but preventing any further electrochemical reduction of the solvent. The lithiation and de-lithiation of graphite in propylene carbonate and ethylene carbonate is shown in Fig. 2.1. This newly formed SEI layer finally allowed commercialization of modern lithium-ion batteries. It is remarkable to note that the difference of a single methyl group prevented the emergence of high energy density batteries nearly for four decades [3]. Ethylene carbonate is now ubiquitous in lithium-ion batteries as a necessary component of the electrolyte for good SEI formation.

Of course, SEI formation is required when the solvent's reduction or oxidation potential is greater than or less than that of anode or cathode potential, respectively. An ideal solvent would have high chemical stability at these electrode potentials and allow fast and efficient Li^+ cation intercalation and de-intercalation without an SEI layer creating a high impedance barrier. No such electrolyte has yet been found to meet these requirements.

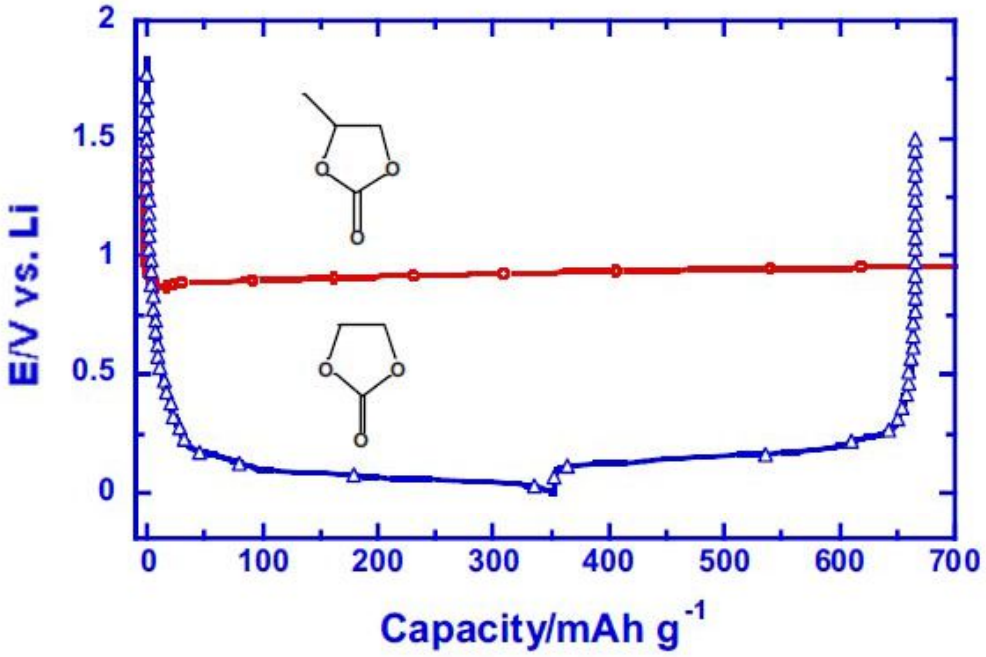

Figure 2.1: Voltage profiles of graphitic anodes in $LiPF_6$/EC and $LiPF_6$/PC during charge indicating reversible Li^+ intercalation chemistry at $<$0.30 V in the former, and the incessant reductive decomposition at 0.8 V in the latter [3].

2.3 Determination of Solid, Liquid, and Gas Phases of Molecular Compounds

The emergence of the lithium-ion battery was delayed for years perhaps by the short-sightedness of using ethylene carbonate since it is a solid at room temperature and an ”unobvious” candidate for use as a solvent. Since it’s introduction in the early 1990s, it remains an essential component in lithium-ion batteries, now for 25 years. It is perhaps, again, our short-sightedness today limiting us from finding another ”unobvious” solvent candidate which may allow us to use next-generation battery materials. It is useful to understand what makes a compound a solid, liquid, or gas at room temperature and

atmospheric pressure. Quite simply, it is the strength of molecule-to-molecule attraction that determines the state of matter it will take. In a solid, intermolecular attraction is strong and allows for very limited movement of individual molecules. Likewise, a liquid has lower intermolecular attraction, allowing for greater freedom of molecular movement, and a gas has even lower attraction. Typically, the attractive force between two permanent dipoles of a liquid or solid is the source of this intermolecular attraction. There are, however, many compounds such as, cyclohexane or heptane, that have a zero dipole, yet are still liquids are room temperature. The nature of this contradiction was explained in 1936 by F. London [26] with consideration to the quantum-induced instantaneous dipoles between the electron clouds of groups of molecules. Since the electron cloud of a molecule is in constant state of movement about a molecule, the cloud may induce repulsion of an adjacent molecule's electron cloud and induce an instantaneous dipole. This weak dipole moment is enough to create an attractive force between the two molecules of zero (or low) dipole moment and keep them in a liquid state. Further, this London Dispersion Force becomes stronger for larger atoms due to the increased polarizability of the atoms. This is demonstrated by the melting and boiling points of halogenated methanes, shown in Table 2.1, which increase in temperature with larger halogen atoms. The larger the halogenated atom, the larger the polarizability of that atom due to the larger dispersion of the electron cloud. The most notable difference in Table 2.1 is the in boiling points of CH_2F_2 and CH_2Cl_2, a difference of over 90 °C. This is because fluorine is an especially electronegative element and has exceptionally low polarizability, substantially lowering the attractive London Dispersion Force between

adjacent molecules. Lastly, the magnitude of this force also increases with increasing molecular surface area since this implies a greater area to which adjacent molecules may induce these instantaneous molecular dipoles. It should be noted that the London Dispersion forces falls under the category of van der Waals force, which is the sum of all forces between two molecules but commonly only references the forces due to the permanent molecular dipoles.

Table 2.1: Melting and boiling points of halogenated methanes.

Molecule	Melting Point / °C	Boiling Point / °C
CH_2F_2	-136	-52
CH_2Cl_2	-97	40
CH_2Br_2	-53	96
CH_2I_2	5	181

2.4 Fluorinated Compressed Gas Solvents

Ethylene carbonate was mostly overlooked till the 1970 [27] for use as a solvent and not till 1990 as a serious component for lithium-ion batteries [25] because it is a solid at room temperature due to the high dielectric constant of this compound. Likewise, there may be solvents that are gaseous at room temperature, yet still show a reasonably high dielectric constant. If such a solvent, or group of solvents, existed, it is reasonable to believe it would have the following characteristics:

1. One or more fluorine atoms for very low polarizability to be gaseous and high polarity for a relatively high dielectric constant.
2. Be a small molecule with low surface area for low London Dispersion Force intermolecular attraction.
3. Have a relatively low vapor pressure to contain easily as a liquid solvent under pressure.

An ideal solvent of this nature may be hydrogen fluoride, however, it is far too hazardous and corrosive a solvent to use in any commercial, or even lab-scale, device. The next series of qualifying compounds would have either a C-F, N-F, or O-F bond(s). Since it is desired to have a compound that has high electronegativity primarily on the fluorine atom(s), the moderately high electronegativity of the nitrogen and oxygen atoms is not desired, and therefore the C-F bond is seen as ideal. This leads to the use of fluorinated hydrocarbons as the primary candidate for a gaseous solvent. The primary candidates for this group of solvents is shown in Fig. 2.2.

The stability of the molecule is highly desirable and should not readily react or polymerize with increased temperature or a catalyst. For this reason, only alkanes with a saturated hydrocarbon structure are considered. Solvents with a relatively high dipole moment are desirable since these generally show a relatively high dielelctric constant, which is desired for solubilizing salts. Lastly, these gaseous solvents are well known to be potent green house gases. Even though these compounds would ideally be contained in a sealed vessel and never expelled into the atmosphere (even after device

HYDROCARBON BASE	CHEMICAL FORMULA	CHEMICAL NAME	STABILITY	DIPOLE MOMENT	GWP
METHANE	CH4	METHANE	GOOD	0	25
	CH3F	FLUOROMETHANE	GOOD	1.85	92
	CH2F2	DIFLUOROMETHANE	GOOD	1.97	675
	CHF3	TRIFLUOROMETHANE	GOOD	1.65	12000
	CF4	PERFLUOROMETHANE	GOOD	0	7390
ETHANE	C2H6	ETHANE	GOOD	0	5.5
	C2H5F	FLUOROETHANE	GOOD	1.94	12
	C2H4F2	DIFLUOROETHANE	GOOD	2.27	124
	C2H3F3	TRIFLUOROETHANE	GOOD	2.32	4470
	C2H2F4	TETRAFLUOROETHANE	GOOD	N/A, MODERATE?	1430
	C2HF5	PENTAFLUOROETHANE	GOOD	1.54	3500
	C2F6	PERFLUOROETHANE	GOOD	0	12200
PROPANE	C3H8	PROPANE	GOOD	0	3.3
	C3H7F	FLUOROPROPANE	GOOD	2.05	N/A, MODERATE?
	C3H6F2	DIFLUOROPROPANE	GOOD	N/A, MODERATE?	N/A, MODERATE?
	C3H5F3	TRIFLUOROPROPANE	GOOD	N/A, MODERATE?	HIGH (?)
	C3H4F4	TERTAFLUOROPROPANE	GOOD	N/A, HIGH?	HIGH (?)
	C3H3F5	PENTAFLUOROPROPANE	GOOD	N/A, MODERATE?	1030
	C3H2F6	HEXAFLUOROPROPANE	GOOD	N/A, MODERATE?	9810
	C3HF7	HEPTAFLUOROPROPANE	GOOD	1.62	3320
	C3F8	PERFLUOROPROPANE	GOOD	0	8830
ETHYLENE	C2H4	ETHYLENE	MODERATE	0	3.7
	C2H3F	FLUOROETHYLENE	MODERATE	1.43	N/A, LOW?
	C2H2F2	TRANS-1,2-DIFLUOROETHYLENE	MODERATE	N/A, MODERATE?	N/A, LOW?
	C2H2F2	CIS-1,2-DIFLUOROETHYLENE	MODERATE	2.42	N/A, LOW?
	C2H2F2	1,1-DIFLUOROETHYLENE	MODERATE	1.38	N/A, LOW?
	C2HF3	TRIFLUOROETHYLENE	MODERATE	1.4	N/A, LOW?
	C2F4	TETRAFLUOROETHYLENE	MODERATE	0	N/A, LOW?
PROPENE (HFOs)	C3H2F4	2,3,3,3-TETRAFLUOROPROPENE	MODERATE	N/A, MODERATE?	N/A, LOW?
	C3H2F4	1,3,3,3-TETRAFLUOROPROPENE	MODERATE	N/A, MODERATE?	N/A, LOW?
ACETYLENE	C2H2	ACETYLENE	LOW	0	N/A, LOW?
	C2HF	FLUOROACETYLENE	LOW	0.73	N/A, LOW?
	C2F2	DIFLUOROACETYLENE	LOW	0	N/A, LOW?

Figure 2.2: The relative stability, dipole moment and global warming potential for a range of fluorohydrocarbons.

end of life), it is desired to use solvents of low global warming potential. Therefore, a short-list of reasonable candidtates include fluoromethane (FM), difluoromethane (DFM), fluoroethane (FE), difluoroethane (DFE), 1,1,1,2-tetrafluoroethane (TFE), and 2-fluoropropane (FP), shown in Fig. 2.3. The physical properties of these compounds are also listed in Table 2.2 and their pressure temperature curves shown in Fig. 2.4.

2.4.1 Conductivity

Fig. 2.5a compares the dielectric constants of conventional solvents with the representative difluoromethane compressed gas solvent. Conventional solvents have high

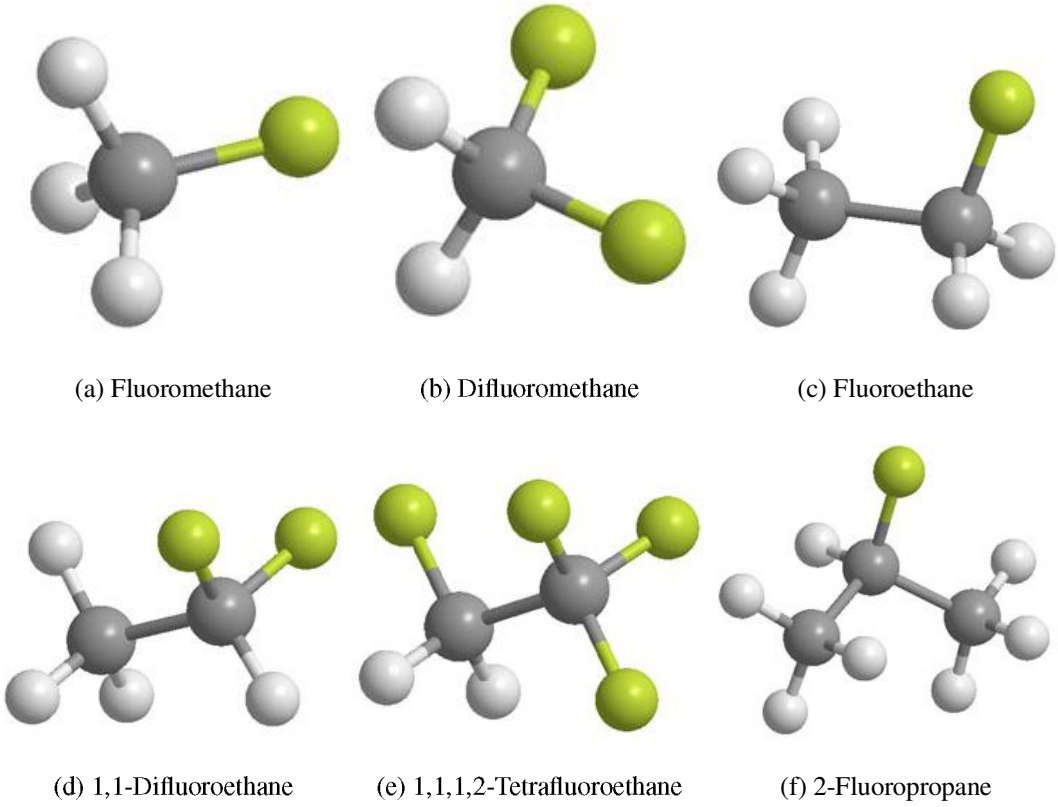

Figure 2.3: Fluorinated compressed gas solvents studied.

dielectric constants (PC = 65, EC = 90, H_2O = 80), while acetontrile has a moderate dielectric constant (ACN = 37). Other commonly used solvents (DMC, DEC, EMC) have very low dielectric constants and are primarily used as co-solvents to lower the viscosity of electrolyte solutions for higher conductivity. Difluoromethane, however, has a dielectric constant of 15, which is comparatively lower but should still be high enough to solubilize salts. Its chlorinated analog, dichloromethane, has a substantially lower dielectric constant of 8.9, due to the less electronegative chlorine atoms. If the dielectric constant of these compressed gas solvents is too low, it is expected the mobility

Table 2.2: Physical properties of fluorinated compressed gas solvents studied.

Solvent	Melting Point (°C)	Boiling Point (°C)	Critical Temp. (°C)	Critical Pressure (psi)	Vapor Pressure (psi)	Global Warming Potential
FM	-138	-78	45	910	478	92
DFM	-136	-52	78	780	220	695
FE	-143	-37	102	730	110	12
1,1-DFE	-117	-25	114	652	74	124
1,1,1,2-TFE	-103	-26	101	589	83	1430
2-FP	-138	-78	-	-	-	-

of ions in the electrolyte would be reduced, due to higher ion-ion interaction and lower the overall electrolytic conductivity. However, ionic mobility is also increased with lower solvent viscosities, also compared in Fig. 2.5b. Difluoromethane has an exceptionally low viscosity of 0.11 cP (at room temperature in the liquid state, as a compressed gas) compared to other low polar solvents (DMC = 0.59 cP, DEC = 0.75 cP, and EMC = 0.65 cP). Most notably, it is still three times lower than acetonitrile (ACN = 0.34 cP), which is often used in highly conductive electrolytes due to its very low viscosity. A very crude method to determine qualitatively the conductivity of a electrolyte solution would be to compare the solvents' ε/η factor, the solvent's relative dielectric constant divided by its viscosity, shown in Fig. 2.5c. Remarkably, difluoromethane shows the highest ε/η factor of 133, followed by acetonitrile (ACN = 108) and water (H_2O = 89.9). Of course,

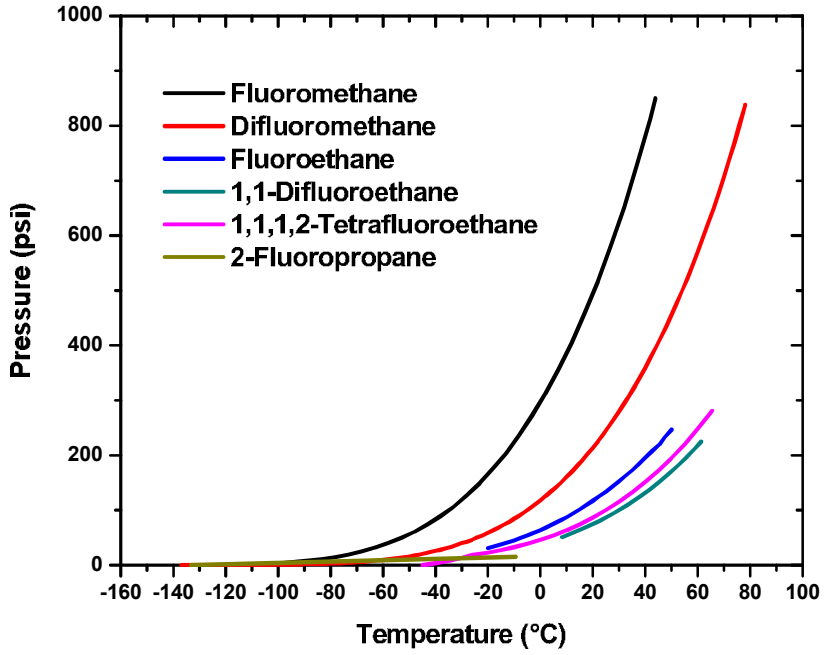

Figure 2.4: Pressure vs. temperature curves for selected fluorinated compressed gas solvents. [4–9]

aqueous electrolytes typically show significantly higher electrolytic conductivity than organic solvent based electrolytes due to the ”proton hopping mechanism”, which is not taken into account in this crude model. However, the fact that difluoromethane shows a comparable ε/η factor to acetontirle warrants further exploration.

2.4.2 Electrochemical Stability Window

In addition to the high conductivity of the electrolyte solution, a wide electrochemical potential window is also required. Having strong molecular bonds that are difficult to break will increase the potential window of the solvents. As is well known,

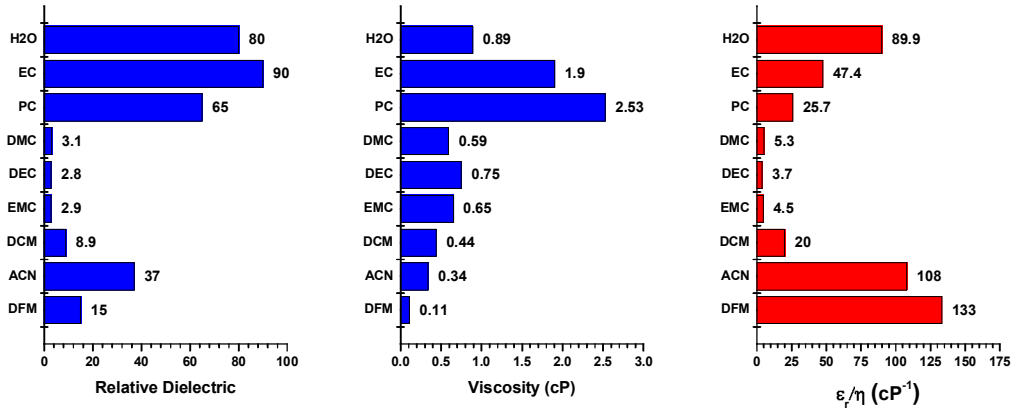

(a) (b) (c)

Figure 2.5: (a) Relative dielectric, (b) viscosity, and the (c) ε/η factor of conventional solvents compared to the fluorinated compressed gas solvent difluoromethane. All values are at 20 °C except the viscosity of EC, taken at 40 °C.

C-H bonds and C-F bonds are some of the strongest in organic chemistry. Further, the stability increases with the number of fluorine atoms bound to the same carbon atom. This increase of stability is reflected in the lengths of the C–F bonds in the series CH_3F (140 pm), CH_2F_2 (137 pm), CHF_3 (135 pm), and CF_4 (133 pm) [28]. To computationally verify the electrochemical stability of these molecules, the HOMO-LUMO energies of the primary compressed gas solvent candidates were computed by DFT and compared to conventional solvents, shown in Fig. 2.6. Remarkably, all the compressed gas solvents show substantially lowered reduction and increased oxidation potentials compared to conventional solvents, lending themselves to wider electrochemical windows. High voltage cathode materials are commonly cited to be limited by the oxidation potential at 4.5 V vs. Li [29] of the electrolyte. The increased oxidation potential of these compressed gas solvents with increased oxidation potentials could potentially enable the use of these

cathodes.

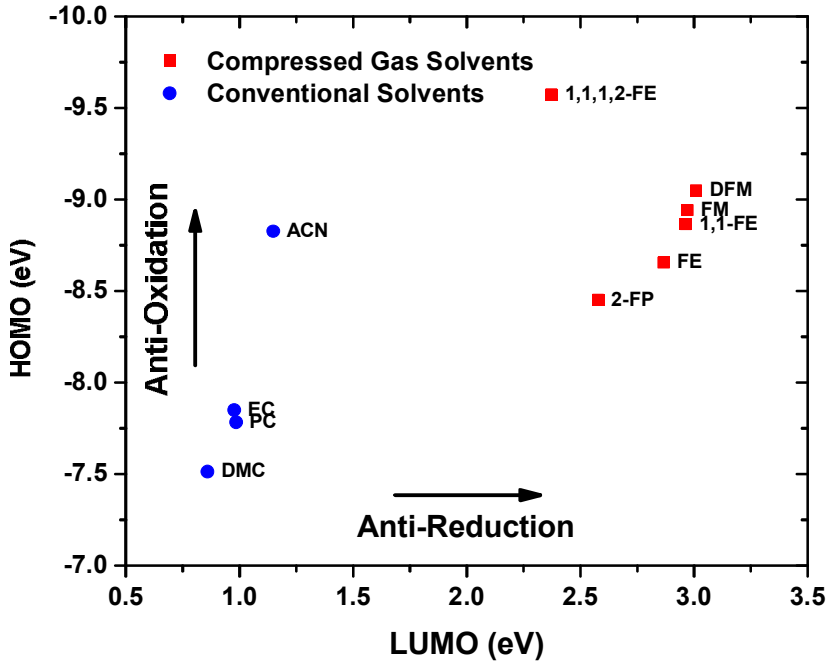

Figure 2.6: DFT calculations of HOMO-LUMO energy levels of common solvents compared to fluorinated comressed gas solvents. Calculations made in ChemBio 3D with B3LYP Basis Set at the 6-311 + G(d,p) level.

2.4.3 Temperature Range

Another advantage to using compressed gas solvent based electrolytes would be the substantially increased temperature window in the low temperature region. Currently, lithium-ion batteries are limited to about -20 °C [23] due to an increase in the electrolyte resistance. The electrolyte resistance increase is due primarily to salt precipitating out of the solvents and freezing of the solvent, limiting their potential in the automotive market, having a low temperature operation requirement of 80% discharge capacity retention at

-40 °C [30]. The liquid range of these conventionally used solvents and the proposed compressed gas solvents are shown in Fig. 2.7. All the propsed compressed gas solvents have melting points <-100 °C, greatly extending the operating temperature of a device using such a solvent. At temperatures higher than their boiling point, the solvents would be contained in the liquid state under their own vapor pressure in a hermetically sealed vessel.

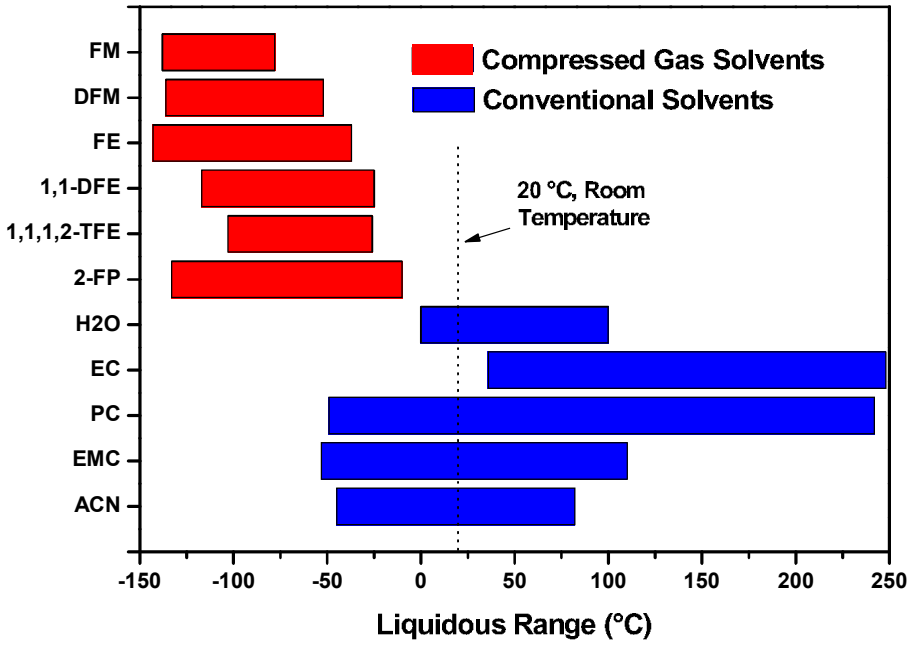

Figure 2.7: Liquidous temperature range of conventional solvents compared to the proposed compressed gas solvents.

2.4.4 Global Warming Potential

In general, these fluorinated compressed gas solvents have a high absorption in the infra-red range, often many times stronger than carbon dioxide. Because of this, they are known to be potent green house gases. Since the global warming potential (GWP, a factor showing the green house warming effect relative to carbon dioxide) might be a point of concern for use of these solvents in any device, a comparison of the ”stored” and ”emitted” GWP content in a traditional gasoline vehicle, a compressed natural gas vehicle, and a hypothetical vehicle based on a battery utilizing a compressed gas solvent based electrolyte is shown in Table 2.3. The GWP stored content of the CGS based vehicle was estimated by the amount of electrolyte used in a Tesla vehicle and relative volumetric densities of the used liquid electrolyte and the CGS (fluoromethane) based electrolyte. Firstly, it is important to note the GWP content of the vehicle should never be emitted into the atmosphere and, therefore, not act as a green house gas. Interestingly, the GWP content of the hypothetical CGS vehicle is on the same order of magnitude of the stored compressed natural gas vehicle. Further, the methane compressed gas the CNG vehicle utilizes is stored at a significantly higher pressure, about 3600 psi [31] vs. about 500 psi for the proposed solvents.

2.5 Conclusion

It has been demonstrated qualitatively that electrolytes based on fluorinated compressed gas solvents warrants investigation due to the promise of potentially high

Table 2.3: Comparison of the stored and yearly emitted GWP contents of three different automotive vehicles.

Vehicle	GWP Stored (CO_2 eq. kg)	GWP Emitted (CO_2 eq. kg/yr)
Gasoline	0	4750
Natural Gas	513	3563
Compressed Gas Solvent	4140	0

conductivity, wide electrochemical stability windows and extended temperature range. Lastly, these solvents are all non-hazardous and safe. However, some of the solvents are flammable under the right concentrations in atmosphere, but may be rendered non-flammable with proper co-solvent mixing. What has not been discussed here is whether or not these solvents form a suitable SEI layer on battery electrodes. Whether these SEI layers are required or not (depending on the oxidation and reduction potentials of the solvent) is still under investigation, but chemical reduction of these solvents and their products is thoroughly explored in Chapter 7.

Chapter 3

Thin-Film Electrochemical Sensor Electrode for Rapid Evaluation of Electrolytic Conductivity, Cyclic Voltammetry and Temperature Measurements

A thin-film electrochemical sensor electrode capable of electrolytic conductivity, cyclic voltammetry and temperature measurements of electrolyte solutions has been fabricated and characterized. The electrode fabrication and calibration is detailed, showing accuracies of $\pm 6\%$ for electrolytic conductivity measurements over the range of

0.1–100 $mS \cdot cm^{-1}$ and temperature measurement within ± 2 °C from -60 °C to 95 °C. The electrode's capabilities are verified with standard Li-ion battery and electrochemical double-layer capacitor electrolytes, to which the measured data match well with literature values. Lastly, demonstration of the electrode's capabilities is shown with determination of cyclic voltammetry curves and electrolytic conductivity over a range of temperatures for other electrolyte solutions. Integration of these three measurement tools into a single, low-cost, high accuracy, rapid measurement electrode can greatly simplify quantitative characterization of novel electrolytes developed in the electrochemical energy storage field.

3.1 Introduction

There is currently a large effort to increase the energy density of batteries and electrochemical double layer capacitors (EDLCs) for applications ranging from electronics to powering vehicles. While developing higher voltage and capacity electrodes is necessary to increase the energy density of batteries, it is generally accepted the electrolyte limits the adoption of these new electrodes [10, 17, 23, 32]. Similarly, the electrolyte breakdown can limit the maximum voltage and energy density of an electrochemical double-layer capacitor [2, 22, 33]. In addition to developing a wider potential electrolyte, the electrolytic conductivity must also be high enough for the device to deliver suitable power. Lastly, the potential window and conductivity of electrolytes over a broad range of temperatures are important parameters in determining the end performance of a device. These

measurements are frequently performed separately with different equipment [10, 33–35], however, having a single measurement electrode to measure both the potential window and conductivity without need for different measurement apparatus would be a useful tool to quickly collect data on a number of electrolyte solutions.

Despite being routine methods, there is often some difficulty in electrolytic conductivity and cyclic voltammetry measurements of electrolyte solutions. Electrolytic conductivity measurements are highly sensitive to the temperature, cell constant, electrode fouling, measurement frequency and circuitry [36, 37] and can be costly or difficult to maintain. Further, commercial equipment may give inaccurate readings over a large range of conductivities [38]. Cyclic voltammetry measurements are often made difficult by a need for careful placement of electrodes in solution and the high cost of noble metal electrodes. Making accurate temperature measurements of the electrolyte solution during data collection also requires that the solution come to thermal equilibrium with the thermal measurement point, which could take several minutes. Attempting to place the temperature probe inside the solution near the measurement electrode could also lead to unavoidable interference with diffusion currents across the solution under study, lowering the accuracy of measurements. Finally, an expensive or difficult to synthesize electrolyte commonly limit researchers in the number of experiments they may run due to the limited volume of solution available to work with [35, 39].

While thin-film conductivity sensors could simplify these measurements, they have been investigated primarily for sea water sensing [40–42]. Combination of electrolytic conductivity measurements with cyclic voltammetry capability has been inves-

tigated for lab-on-a-chip devices for applications in environmental monitoring in sea water [37], but an integrated temperature sensor with these capabilities has not been studied previously. Further, detailed fabrication and calibration analysis of these electrodes, and application with electrolytes for electrochemical energy storage, has not been shown. Presented here is the fabrication, calibration characterization and demonstration of a new multifunctional, low cost thin-film electrochemical sensor electrode capable of electrolytic conductivity and cyclic voltammetry measurements with simultaneous temperature measurement via an on-chip resistance temperature detector (RTD) sense device, tools which have not previously been integrated into a single electrode.

3.2 Materials and Methods

3.2.1 Electrode Fabrication

While there are a range of thin-film materials to fabricate a thin-film electrode, such nickel or copper, many of these may oxidize easily and be difficult to maintain a clean surface. Gold is an excellent electrode material, but typically shows a lower limit than platinum to the applied oxidation potential. Platinum was chosen as the active film in the fabricated electrodes since this material (1) shows good chemical inertness over a wide potential range, (2) is easy to clean and with no oxide surface formation and (3) has a very linear temperature coefficient of resistance, ideal for the integrated RTD device.

Electrode wafers were made by typical semiconductor fabrication techniques. Borosilicate glass slides (75 x 50 x 1 mm, average surface roughness R_a = 9 nm, Fisher

Scientific) were used as wafer substrate and were cleaned by successive sonication in acetone, isopropanol, and ethanol, dried under a stream of nitrogen gas and heated to 125 °C on a hot plate for 5 minutes to dehydrate the surface, followed by an O_2 plasma clean for 5 minutes at 200 W power and 200 mT pressure (Technics PEIIB Planar Etcher). Photoresist (Futurrex NR9 1500PY) was then applied to the wafer via spin coating and the electrode pattern was then transferred via photolithography (Karl Suss MA6 Mask Aligner) followed by thin-film sputter deposition (Denton Discovery 18) onto the patterned wafer. A 10 nm thick titanium adhesion layer was first sputter deposited followed by a platinum metal layer of various thicknesses, followed by lift-off by sonication in acetone. Cleaning of the wafer by sonication in solvent, drying, O_2 plasma clean and application of photoresist was then repeated, as described above. A second pattern, exposing only the RTD and base of the electrochemical electrodes for passivation, was then transferred to the photoresist. Passivation of portions of the platinum film was done by sputter deposition of a second 10 nm thick titanium adhesion layer followed by a 250 nm thick silicon dioxide passivation layer. All thin-film sputter depositions were done in an argon atmosphere with a base pressure of 5 μT and a sputter pressure of 2.5 mT for titanium and platinum and 4.5 mT for silicon dioxide. Electrode patterning and dimensions are shown in Fig. 3.1a, and with more detail of the platinum electrodes configurations used in electrolytic conductivity measurements shown in Fig. 3.1b. Thin-film thickness measurements (Veeco Dektak 150) were an average of five data points over a wide area with uncertainties given as the maximum deviation from the average measurement.

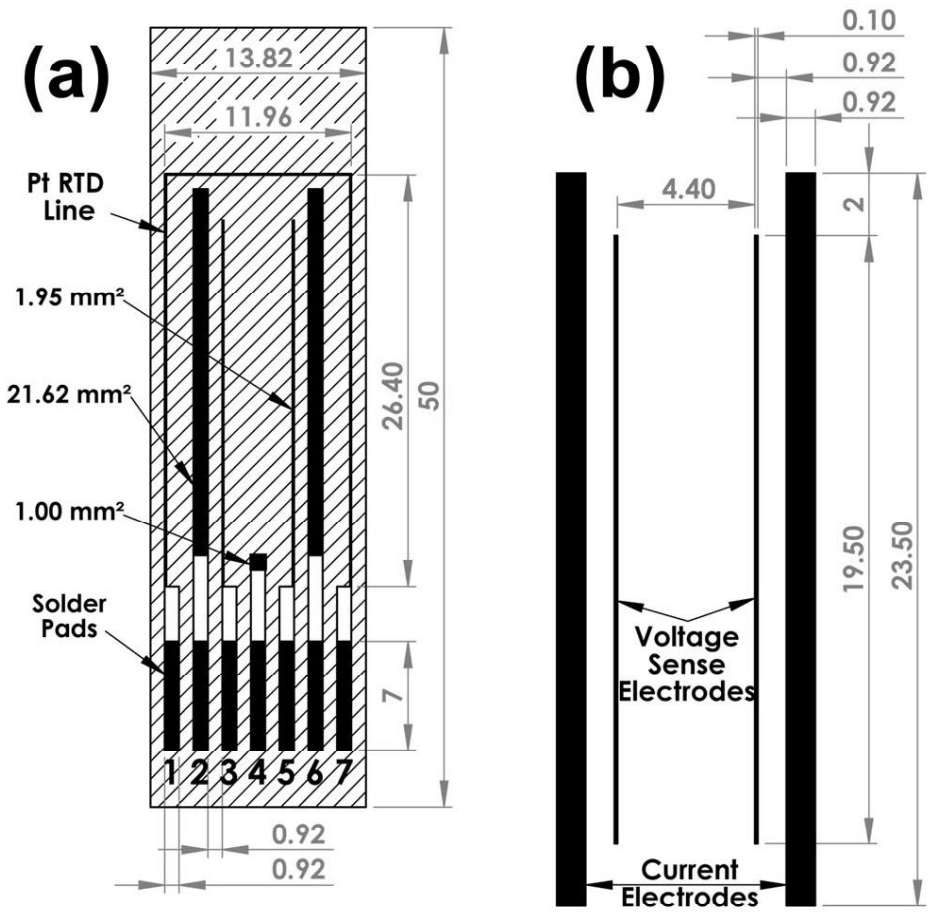

Figure 3.1: a) Patterning and dimensions for thin-film electrochemical sensor electrode and b) dimensional detail of the electrodes used for electrolytic electrochemical conductivity measurements.

After fabrication, the wafer was diced into individual electrodes; typically one wafer yielded four electrodes. The diced electrodes were then annealed in a tube furnace under an argon atmosphere at 350 °C for 2 hours with a ramp rate of 5 °C·min^{-1}. Electrical connections were made to the fabricated electrode by soldering Kapton insulated wires to platinum solder pads. The solder joints were then sealed with two separate epoxies. First, a flexible epoxy (Armstrong A-12) was applied and cured on the glass substrate, followed by application and curing of a harder epoxy (Loctite 20NS). Epoxy

curing was typically done at ca. 80 °C. The use of the dual-epoxy system prevents cracking of the glass substrate at extreme temperatures due to the thermal expansion mismatch between the epoxy and glass. Care was taken during epoxy application to make sure the solder joints and solder pads were completely insulated with epoxy and that the active platinum electrode areas were not covered by any epoxy. Kapton insulated wires and Loctite 20NS epoxy were both used for their good chemical resistance to solvents and thermal stability.

3.2.2 Measurement Apparatus

Block diagrams of electrical connections between the fabricated electrode and the measurement equipment, along with the corresponding solder pad number designations, are shown in Fig. 3.2. While the RTD device had its own separate electrical connections, electrolytic conductivity and cyclic voltammetry measurements shared electrical connections and were switched between equipment for measurement. For RTD measurements, two wires were soldered to each electrode pad #1 and #7 for four-wire resistance measurements, made by an Agilent 34970A Data Acquisition Unit with a 34902A Multiplexer Module, shown in Fig. 3.2a. The RTD was calibrated by placing a Type-K thermocouple (Omega Engineering) in intimate contact with the electrode and making simultaneous temperature and RTD resistance measurements across a range of temperatures. The thermocouple measurement was accurate to ± 2 °C and was most significant source of error in RTD measurements.

Cyclic voltammetry measurements were made by connection of the counter, work-

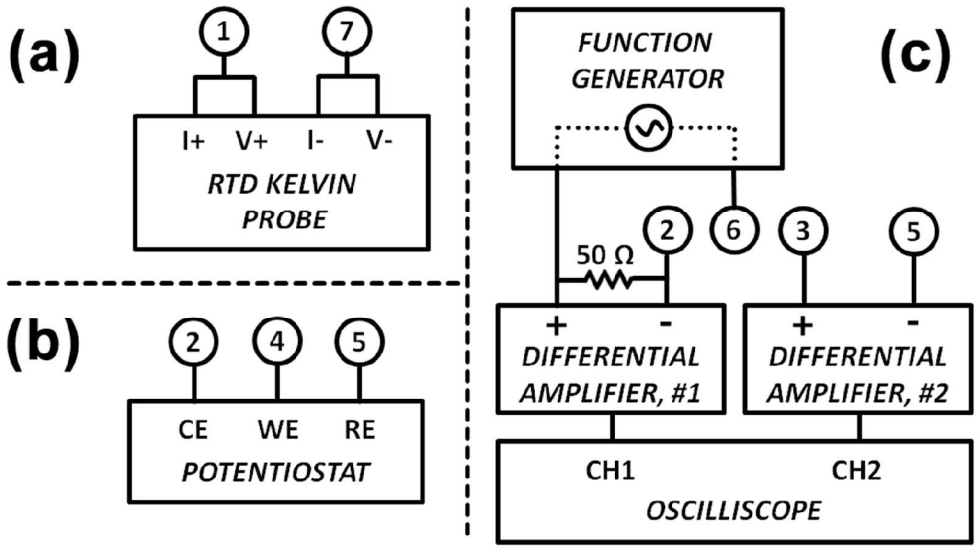

Figure 3.2: Block diagrams showing electrical connections between the electrode pads and measurement equipment for a) RTD, b) cyclic voltammetry and c) electrolytic conductivity measurements.

ing and reference electrodes, electrode pads #2, 4, 5, respectively, to a Bio-Logic SP200 potentiostat, shown in Fig. 3.2b. The counter, working and reference electrodes had geometric areas of 21.62, 1.00 and 1.95 mm^2, respectively. On occasion, a separate lithium metal reference electrode was introduced into solution, connected to a separate wire, while the platinum reference electrode was unused for cyclic voltammetry measurements. Since the small size of the electrodes could introduce a significant voltage drop [43], iR-drop software compensation was used for all cyclic voltammetry measurements.

Electrolytic conductivity measurements were made using a custom built impedance analyzer, schematically shown in Fig. 3.2c. A floating AC current signal from an Agilent 33120A 15 MHz Function Generator was passed through the electrolyte solution via the current electrodes, pads #2 and #6. Two separate electrodes, pads #3 and #5, were used to sense the voltage between the current electrodes, typically 10-20 mV_{rms}. Current

measurements were made by measurement of the voltage drop across a 50 Ω thin-film resistor which the AC current was passed through. A thin-film current-sense resistor was used since it has little capacitive or inductive behavior at the frequencies measured. The geometric areas of the current and voltage electrodes were 21.62 mm^2 and 1.95 mm^2, respectively. To reject common noise, amplify the voltage signals and avoid ground loops through the electrolyte, the voltage across both the current-sense resistor and across the sense electrodes were measured differentially through two separate Tektronix ADA400A Differential Preamplifiers, which then sent the voltage measurements to a Tektronix TDS1000 Oscilloscope. It was verified the preamplifiers did not significantly attenuate the signals across the frequencies used. Cell constant calibrations were done from 1 MHz to 100 Hz, while electrolytic conductivity measurements were typically done at a frequency of 1 kHz, which generally showed a phase angle between -5 to 0° for all measurements.

Electrolytes were all prepared under argon atmosphere and bubbled with argon gas to remove trace oxygen for at least 5 minutes immediately prior to using. The measurement electrode was fixed to a screw-on cap of a 20 mL glass vial, in which the electrolyte solution was contained and all measurements were performed. Careful placement of the electrode in the center of the vial was done in order to avoid changing fringe-field effects from modifying the calibrated cell constant for electrolytic conductivity measurements. Electrolyte solution volume was kept constant for all experiments and covered the entire measurement electrode's surface. After electrolyte and electrode preparation, the assembly was transferred to a temperature chamber where measurements

were performed.

Data acquisition and hardware control were done via LabView software. Typically, temperature and electrolytic conductivity measurements were made at a rate of one data point every few seconds. This allowed for rapid measurements of electrolytic conductivity over a wide range of temperatures.

3.2.3 Chemicals

For electrolytic conductivity measurements, the electrode cell constant was calibrated with potassium chloride conductivity standards (NIST-traceable) from Cole Parmer. Tetraethylammonium tetrafluoroborate ($TEABF_4$, electrochemical grade,$>$99%), tetrabutylammonium hexafluorophosphate ($TBAPF_6$, electrochemical grade, $>$99%), lithium hexafluorophosphate ($LiPF_6$, battery grade, $>$99.99%), ethylene carbonate (anhydrous, $>$99%), dimethylcarbonate (anhydrous, $>$99.9%), tetrahydrofuran (anhydrous, $>$99.9%), dichloromethane (anhydrous, $>$99.8%), propylene carbonate (anhydrous, $>$99.7%) and acetonitrile (anhydrous, $>$99.9%) were all purchased from Sigma-Aldrich.

3.3 Results and Discussion

3.3.1 Resistance Temperature Detector Calibration

To verify consistent sputter deposition rates of the thin-films, platinum and titanium adhesion layer thickness measurements were made with various platinum deposition

times, shown in Fig. 3.3. An excellent linear relation is found ($R^2 > .999$) for platinum deposition times from 50 to 300 seconds with a deposition rate of 0.87 ± 0.02 nm·sec^{-1}. The titanium adhesion layer deposition was held constant through all depositions and is found to be 10.74 ± 4.18 nm thick. The low surface roughness of the glass substrate was not expected to create discontinuities in the platinum RTD element. However, since any inadvertent discontinuities in the thin-film that might arise from insufficient film thickness would lower measurement accuracy and give less linearity between resistance and temperature readings, the effect of RTD element film thickness on electrical resistance was studied. Calibration curves of multiple RTD elements of different platinum thin-film thicknesses are shown in Fig. 3.4 for a temperature range of -60 to +95 °C. The calibration curves for all film thicknesses show excellent linearity ($R^2 > .999$ for all curves) over the entire temperature range measured, as is commonly exhibited by platinum RTDs [44]. A good indication of uniformity and purity of the platinum RTD may be shown by the value of the thermal coefficient of resistance (TCR), calculated by

$$TCR = \frac{1}{R_{ref}} \cdot \frac{dR}{dT} \tag{3.1}$$

where R_{ref} in Eqn. 3.1 is the resistance at a reference temperature of 25 °C. Despite the good linearity of the platinum RTD elements, the calculated values of the TCR, shown in Table 3.1 for various platinum film thicknesses, differs by roughly a factor of two from the accepted value of 3926 ppm·K^{-1}. This difference may be due to the relatively thin film thickness, diffusion of the titanium adhesion layer through the platinum and grain

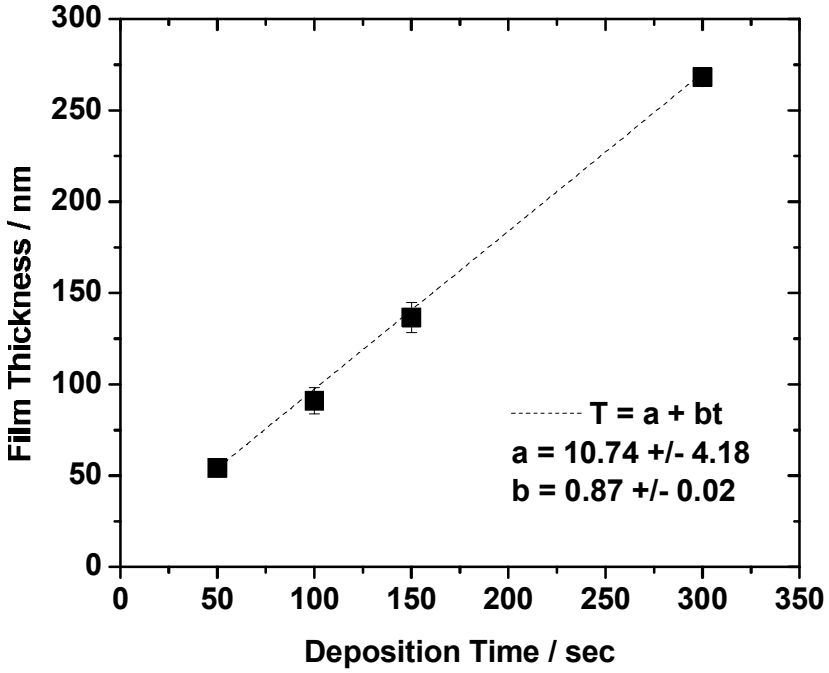

Figure 3.3: Thin-film thickness as a function of platinum sputter deposition time with a titanium adhesion layer, as described in Section 3.2.1 of the text.

boundaries that may exist in the thin-film RTD.

The resistance stability of two different RTDs of thicknesses of 136 and 268 nm at 85 °C in air is shown in Fig. 3.5. The RTDs show less than 0.015% change in resistance over 80 hours at this elevated temperature, showing the excellent temperature stability of the devices. Further, the largest fluctuations in the devices are correlated to the night-day temperature change in the laboratory from which the measurement electronics have a slight measurement change, showing the actual stability of the RTDs are likely much better. Routine cleaning by sonication in solvents, gentle wiping and soaking in various solvents at elevated temperatures similarly showed little or no change in the RTD

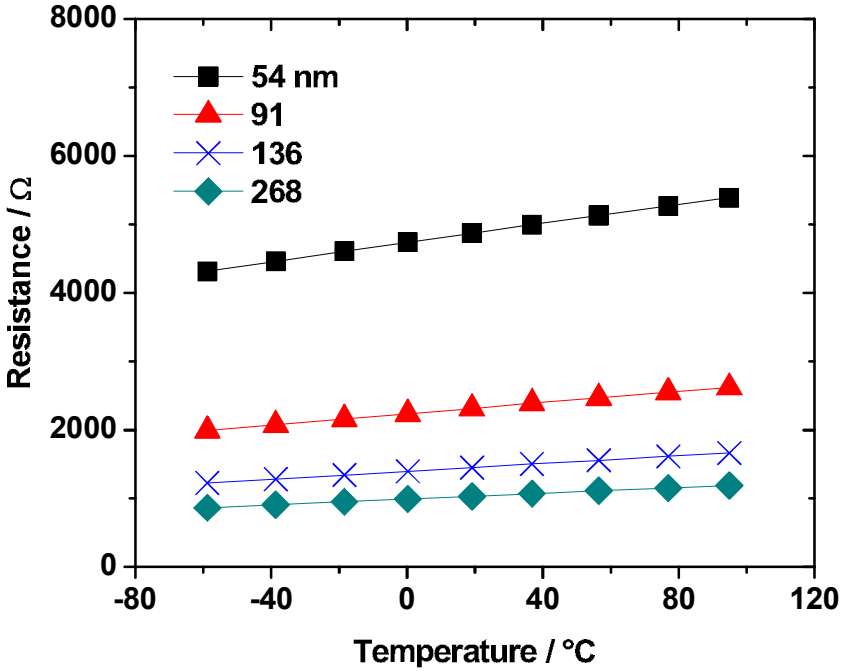

Figure 3.4: Resistance as a function of temperature for four RTDs of various platinum thin-film thicknesses.

calibration. Thus, the highly stable properties of the platinum RTD allow it to be reused routinely without need for repeated calibration.

3.3.2 Electrolytic Conductivity Calibration

In contrast to metals, in which electrons are the primary charge carriers, electrolytes conduct current through transport of ions, therefore typical DC electrical resistance measurements are not possible. In order to minimize capacitive effects via charge build up at the electrode surface, an AC method must be utilized for electrolytic conductivity measurements. For the thin-film electrochemical sensor electrode, a four-electrode

Table 3.1: Platinum RTD properties calculated from data in Fig. 3.4

Thickness/nm	Resistance at 25 °C/Ω	dR/dT	TCR/ppm·K^{-1}
54	4870	7.00	1437
91	2313	4.10	1772
136	1450	2.84	1961
268	1030	2.12	2060

measurement method, rather than a two-electrode measurement method, was chosen for conductivity measurements in order to avoid electrode contamination with reduced or oxidized species at the electrode surface and have higher measurement accuracy across a wide range of solution conductivities. To make electrolytic conductivity measurements, an alternating current is passed through the electrolyte between two outer electrodes and the voltage drop is sensed between two inner electrodes. The voltage sense electrodes were configured to be significantly narrower than the current electrodes such that the electrolytic current induced was as uniform as possible across the voltage sense electrodes.

Two electrodes passing a current through an electrolyte solution may simply be modeled as two RC circuits in series. The first RC circuit comprises of the electrolyte resistance and bulk electrolyte capacitance, R_b and C_b, followed by the second RC circuit comprised of the charge-transfer resistance and double layer capacitance, R_{ct} and C_{dl}, between the electrode and electrolyte interface. Depending on the particular values of these resistive and capacitive components, one or two semi-circles may be formed in the

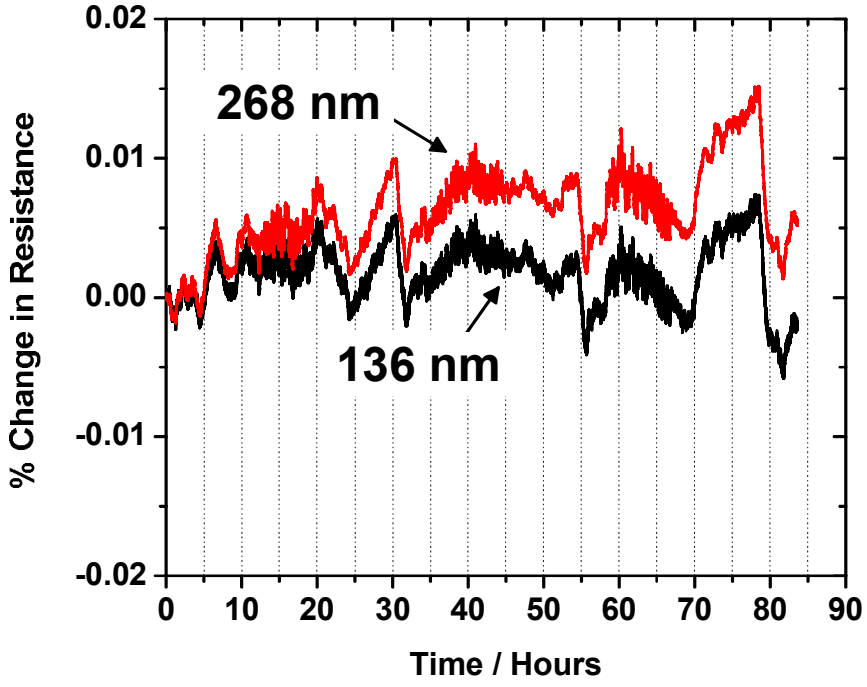

Figure 3.5: Resistance stability of two platinum RTD elements over time while held at 85 °C in air.

corresponding Nyquist plot. The measured bulk electrolyte resistance would correspond to the real component of the impedance where the phase goes to zero toward the end of the first semi-circle.

To calibrate the cell constant of the measurement electrode, four different potassium chloride electrolyte conductivity standards of 0.1, 1, 10 and 100 $mS \cdot cm^{-1}$ were used and impedance and phase measurements were recorded across a range of frequencies from 1 MHz to 100 Hz. Fig. 3.6a shows the phase angle of the impedance vector vs. frequency and it is seen that higher conductivity solutions go to zero phase angle at progressively higher frequencies. Similarly, higher conductivity solutions show less

change in the real component of the impedance, Z', over a wider frequency range, as shown in Fig. 3.6b. These features are common in electrolyte solutions, as explained elsewhere [36]. A Nyquist plot for each calibration solution is shown in Fig. 3.6c with the points near zero phase angle, where resistance measurements are taken, marked with the corresponding frequency. Some features shown in the Nyquist plots, such as negative real impedance and inductive behavior, are commonly seen in such measurements and are generally disregarded as artifacts from the measurement hardware [36].

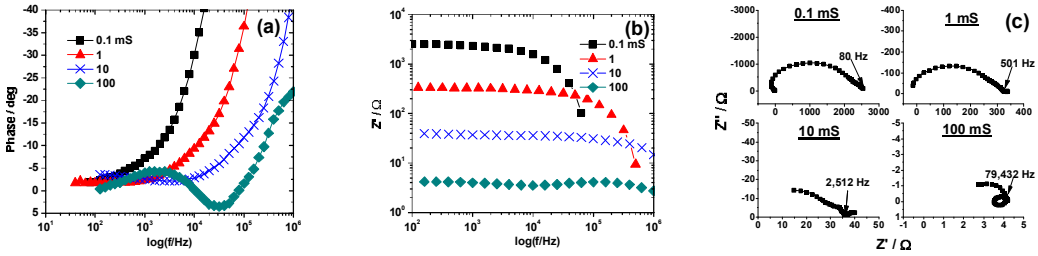

Figure 3.6: a) Phase and b) real impedance measurements vs frequency and c) Nyquist plots of standard KCl electrolytic conductivity calibration solutions at 25 °C.

The cell constant, needed to determine the conductivity of an electrolyte, is very dependent on the geometrical configuration and surface area of the measurement electrodes, as well as the geometry and material (electrically insulating or conducting) of the electrolyte container, and calibration is generally done routinely before measurements. By correlating the measured electrolytic resistance, units of Ω, of each solution to the solutions NIST-traceable calibrated conductivity (κ), units of $S \cdot cm^{-1}$, one may determine the measurement electrode's cell constant, K, units of cm^{-1}. Typically, the simple relation is given as

$$k = K \cdot R^{Q} \tag{3.2}$$

where R is the measured electrolyte resistance and, typically, $Q = -1$. Equation 2 is used to fit the electrolytic resistance data points in Fig. 3.7 for each calibration solution with the fit parameters detailed in Table 3.2. When the constant Q is set to -1, as routinely done through the literature [45,46], the error of the fit is found to be approximately 0.14% and 60% at solution conductivities of 100 and 0.1 mS·cm^{-1}, respectively. While this broad range of conductivity is not typically easy to measure accurately even with commercially available equipment [38], measurement accuracy across the full range of conductivities should be improved. By allowing the constants Q and K to be simultaneously fit to the measured data, a significantly improved accuracy is obtained. Fitting constant Q to only a slightly different value, $Q = -1.071$, improves the accuracy to within $\pm$ 6% error over all conductivity solutions used, accounting for four orders of magnitude, as detailed in Table 3.3. It is possible this new fitting parameter for finding the cell constant could greatly improve accuracy of other conductivity measurement equipment over a wider range of electrolyte conductivities. Although not studied in detail, it is believed the fitting parameter Q is highly dependent on fringe field effects created by the container size and shape holding the electrolyte solution.

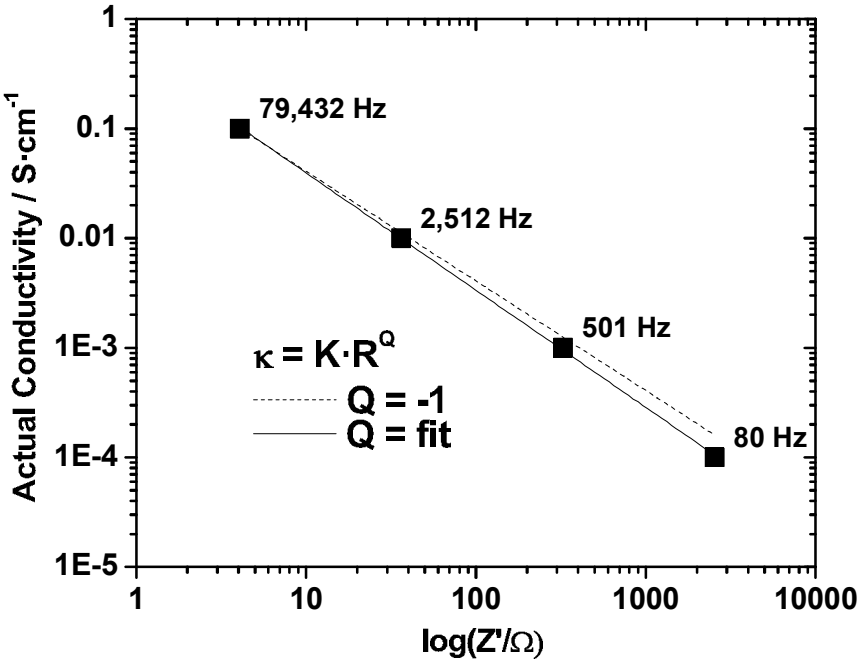

Figure 3.7: Measured electrolyte resistance vs. actual conductivity of the standard KCl electrolytic conductivity calibration solutions at 25 °C with the corresponding measurement frequency.

3.3.3 Verification of Measurement Electrode Calibration

To verify the measurement electrode's electrolytic measurement accuracy over a wide range of conductivities and temperatures, measurements of a standard lithium battery electrolyte (1.0 M $LiPF_6$ in ethylene carbonate and dimethylcarbonate, 1:1 by wt.) and a standard electrochemical double-layer capacitor electrolyte (1.0 M $TEABF_4$ in acetonitrile) were made and compared to literature values [10–12], shown in Fig. 3.8a. The accuracy of the measurements, over a wide conductivity from 3 to 76 $mS \cdot cm^{-1}$ and from -35 to 75 °C, are in close agreement with the literature values. The percent difference in the conductivity measurement as compared with literature values is shown

Table 3.2: Cell constant values fit to the equation $k = K \cdot R^Q$

Parameter	$Q = -1$	$Q =$ fit
K	0.407 ± 0.003	0.463 ± 0.001
Q	-1.000	-1.071 ± 0.002

Table 3.3: Percent error of calculated conductivity with actual conductivity.

Conductivity/mS·cm^{-1}	$Q = -1$	$Q =$ fit
0.1	-60.19	-4.51
1	-25.09	5.60
10	-12.01	1.28
100	0.14	-2.75

in Fig. 3.8b. The measurement error for the lithium based electrolyte is less than 4%, within the $\pm$ 6% error determined earlier for the calibrated thin-film electrode. However, the error for the acetonitrile based electrolyte is in 6-7% error with literature values. This discrepancy is probably due to the measurement error in the comparative data, which is not given in their work [11, 12].

Cyclic voltammetry curves of the lithium based electrolyte were also performed in order to verify electrode behavior at higher current densities at a range of temperatures, as shown in Fig. 3.9 (only anodic currents shown for clarity). The sharp change in current near 0 V vs. Li is due to the lithium plating onto the platinum electrode, and the small peak at 0.7 V vs. Li is due to lithium stripping off of the platinum electrode. Other

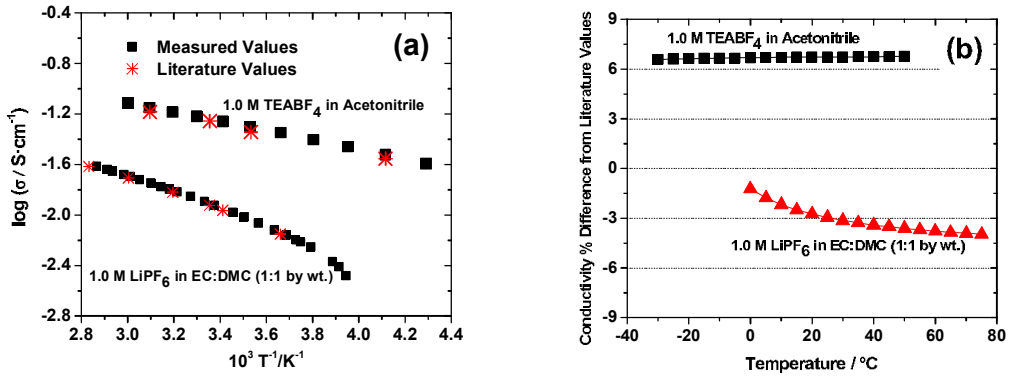

Figure 3.8: a) Comparison of and b) percent difference between measured and literature values of two common electrolyte solutions over a wide temperature range. Literature data replotted in (a) with permission from references [10–12].

features at 2.0 and 3.5 V vs. Li are thought to be due to impurities (O_2, H_2O, etc.) in the electrolyte [12, 47]. Cyclic voltammetry curves were also taken at various temperatures, also shown in Fig 9. There is a clear increase in current at higher temperatures due to the increased diffusion within the electrolyte and a lower energy barrier for chemical reactions to occur. Cyclic voltammetry studies at various temperatures is an excellent method to observe electrochemical kinetics with detail, though it is not a common technique used in the literature.

3.3.4 Characterization of Electrolytes with Thin-Film Electrochemical Sensor Electrode

A group of four electrolytes were used to demonstrate the ability to determine the potential window and electrolytic conductivity with the thin-film measurement electrode. The four electrolytes all consisted of 0.1 M tetrabutylammonium hexafluorophosphate in

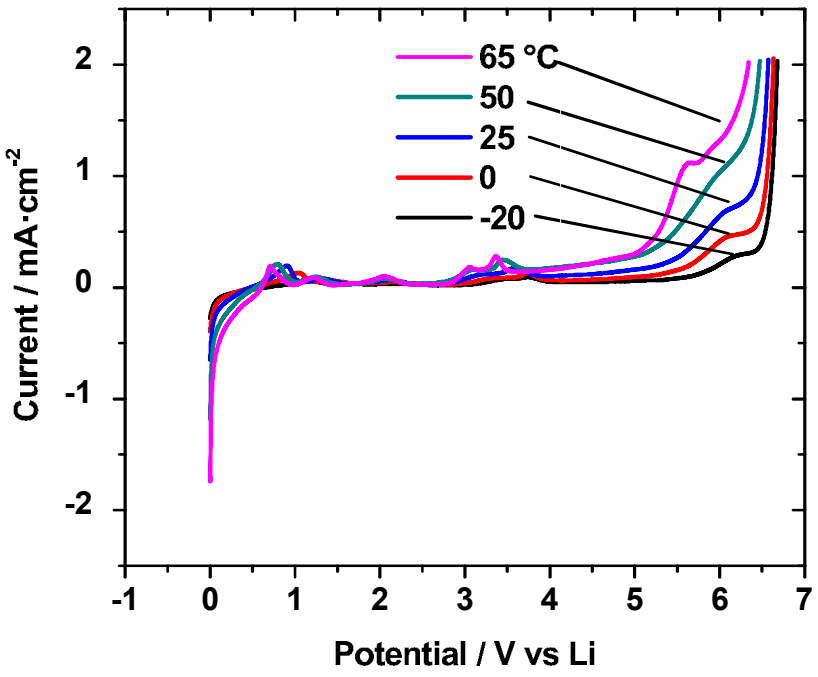

Figure 3.9: Cyclic voltammetry curves of 1 M $LiPF_6$ in EC:DMC (1:1 by wt.) over a range of temperatures with a 100 $mV \cdot sec^{-1}$ sweep rate, platinum working and counter electrodes and a lithium metal reference electrode. Only anodic currents shown for clarity.

various solvents; tetrahyrdrofuran, dichloromethane, propylene carbonate and acetonitrile. Cyclic voltammograms for the four electrolytes at room temperature are shown in Fig. 3.10a, along with their reduction potential, oxidation potential, and total potential windows listed in the inset. A cutoff current of 1 $mA \cdot cm^{-2}$ was used to determine the limiting potentials. It is important to note that this current, while commonly used in the literature, is an arbitrary value and is also dependent on the potential sweep rate used.

The conductivity of the same four electrolytes was also examined at a broad temperature range, shown in Fig. 3.10b. As expected, the acetonitrile based electrolyte has a

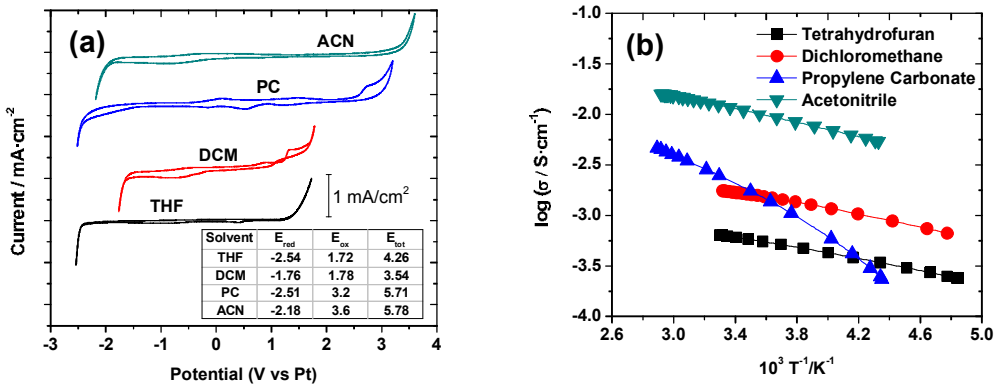

Figure 3.10: a) Cyclic voltammetry curves with a 100 $mV \cdot sec^{-1}$ sweep rate with platinum working, counter and reference electrodes and b) electrolytic conductivity measurements of 0.1 M $TBAPF_6$ in various solvents

significantly higher conductivity than the others due to the solvent's low viscosity, which increases ion mobility within the electrolyte. While having an overall lower conductivity than acetonitrile, dichloromethane and tetrahydrofuran have a much lower freezing points (-97 °C and -108 °C, respectively) vs. acetonitrile (-45 °C) and show good conductivity as low as -60 °C. Propylene carbonate, while having excellent electrochemical stability, often shows low electrolytic conductivities due to the high viscosity of the solvent.

3.4 Conclusion

A thin-film electrochemical sensor capable of temperature, ionic conductivity and cyclic voltammetry measurements has been fabricated and characterized and offers a low-cost, simple device capable of making critical high accuracy electrochemical measurements rapidly over a wide temperature range and wide electrolytic conductivity range. The design and fabrication techniques have been detailed and the device would be simple

to fabricate for any researcher with standard thin-film fabrication equipment. Contrary to the conventional method of waiting a number of minutes for thermal equilibrium to make measurements, an on device RTD has been fabricated and capable of determining the temperature right at the point of measurement, which enables rapid measurements rather than waiting for thermal equilibrium between the electrolyte and thermal measurement device outside the solution. Electrolytic conductivity measurement calibration has also been described with a new method of calculating the electrode cell constant with accuracy of $\pm$ 6% for electrolytic conductivity over a range of 0.1 to 100 $mS \cdot cm^{-1}$ which, to the authors knowledge, is the highest accuracy shown over such a wide range. The temperature and electrolytic conductivity calibrations have been verified by measuring two standard electrolytes and comparing with literature values. Cyclic voltammetry curves over various temperatures for an electrolyte have also been shown and can be a useful technique to observe in more detail certain electrochemical kinetics. Lastly, demonstration of the electrode measurements with four other electrolytes with cyclic voltammetry and electrolytic conductivity over a range of temperatures has been shown. With a number of new solvents and salts with applications in the rapidly growing field of electrochemical energy storage, accurate and rapid electrochemical characterization is often necessary and the described thin-film electrochemical sensor electrode could greatly simplify these processes with improved measurement accuracy.

Acknowledgements

I would like to acknowledge Jimmy Mac, Chulmin Choi, Tae Kyoung Kim, Duyoung Choi, Ying Shirley Meng and Sungho Jin, who helped co-author the material that has been acceted for publication in this chapter to the Journal of Applied Electrochemistry under the title "Thin-Film Electrochemical Sensor Electrode for Rapid Evaluation of Electrolytic Conductivity, Cyclic Voltammetry and Temperature Measurements". Further, I acknowledge financial support of this work by DOE ARPA-E Grant No. DE-AR0000379 and by Iwama Fund at UC San Diego and helpful discussions and fabrication assistance with the Nano3 Cleanroom staff Sean Parks and Ivan Harris at UC San Diego.

Chapter 4

Conductivity and Cyclic Voltammetry Studies of Compressed Gas Solvent Based Electrolytes

Six fluorinated compressed gas solvents are tested for conductivity over temperature and the potential windows via cyclic voltammetry with various salts. It is found these electrolytes show exceptionally high conductivities over a broad range of temperatures and have very wide potential windows.

4.1 Introduction

As discussed in Chapter 2, fluorinated compressed gas solvents have remarkable properties that warrants investigation as solvents for electrochemical energy storage

devices. Six fluorinated compressed gas solvents are explored; fluoromethane, difluoromethane, fluoroethane, 1,1-difluoroethane, 1,1,1,2-tetrafluoroethane and 2-fluoropropane. It is demonstrated, regardless of their comparably low dielectric constants, these solvents form fairly high conductivity electrolytes and have remarkably wide potential windows.

4.2 Experimental

4.2.1 Methods

Thin-film measurement electrodes were fabricated for conductivity and cyclic voltammetry measurements, as described in Chapter 3. The measurement electrodes were soldered to wires which were attached to an electrical high-pressure feed through (Conax Technologies). The electrodes and salt was then inserted into a stainless steel 316 pressure vessel and sealed shut under argon atmosphere. Vacuum was then briefly pulled on the cell through a valve and subsequently cooled to ca. -60 °C. Solvent was then introduced into the cell in gaseous form by evaporation from a pressurized liquid state at room temperature, which was then condensed back to a liquid state inside the cooled cell. After solvent filling, the valve was again shut. The cell mass was measured before and after solvent filling to verify the cell was completely filled with liquid solvent.

The cells were then temperature cycled for conductivity experiments in a temperature chamber (Espec). Cyclic voltammetery curves were conducted with a potentiostat (BioLogic SP-200) and were all done at room temperature, except where noted. Pressure measurements were done using a pressure transducer (Omega Engineering).

4.2.2 Chemicals

Difluoromethane (DFM, 99.9%), fluoroethane (FE, 97%), 1,1-difluoroethane (DFE, 99%), 1,1,1,2-tetrafluoroethane (TFE, 99%) and 2-fluoropropane (FP, 98%) were purchased from Synquest Laboratories. Fluoromethane (FM, 99.99%) was purchased from Airgas. Tetrabutylammonium hexfluorophosphate ($TBAPF_6$), tetrabutylammonium perchlorate ($TBAClO_4$), tetrabutylammonium bis(trifluoromethyl-sulfonyl)imide (TBATFSI), tetrabutylammonium tetrafluoroborate ($TBABF_4$), tetraethylammonium tetrafluoroborate ($TEABF_4$), tetraethylammonium hexafluorophosphate ($TEAPF_6$) and 1-ethyl-3-methylimidazolium tetrafluoroborate ($EMIBF_4$) were all purchased from Sigma-Aldrich in electrochemical grade, >99% purity). 1-ethyl-3-methylimidazolium bis(trifluoromethyl-sulfonyl)imide (EMITFSI, electrochemical grade, >99%) was purchased from Covalent Associates. Lithium bis(trifluoromethyl-sulfonyl)imide (LiTFSI) was purchased from 3M (HQ-115) and vacuum dried at 140 °C before use.

4.3 Results and Discussion

4.3.1 Non-Lithium Based Electrolytes

A variety of fluorinated compressed gas solvent based electrolytes were tested with various salts. The shape of the conductivity vs. temperature curves are distinctly different from electrolytes based on conventional solvents. Typically, electrolytic conductivity is roughly linear, increasing with temperature. This is due to increased ion

mobility with decreasing viscosity of the electrolyte at increased temperatures. Using a difluoromethane solvent based electrolyte, we see three distinct regions of conductivity, as shown in Fig. 4.1 for 0.1 M $TBAPF_6$ in difluoromethane. At lower temperatures in Region 1, up to roughly 0 °C, the electrolytic conductivity increases, presumably due to a lowering of the electrolyte viscosity. At higher temperatures in Region 2, roughly from 0 °C to +48 °C, a gradual decrease in conductivity is seen. This decrease is thought to be due to increased ion-ion interaction from decreased charge screening from the lowering of difluoromethane's dielectric constant at higher temperatures [5, 48]. At higher temperatures in Region 3, roughly >50 °C, there is an abrupt change in the decrease of the electrolytic conductivity. As seen in Fig. 4.1, this change is very well correlated to a sharp increase in pressure at 48 °C. The observed increase in pressure at 48 °C and 500 psi is far from the critical point of difluoromethane (T_c = 78.1 C and 838 psi) and so is not due to any super critical phenomena.

It has previously been shown that an isothermal increase in pressure in difluoromethane and 1,1,1,2-tetrafluoromethane can lead to a substantial change in conductivity due to an increase in the solvent dielectric constant with pressure, reducing ion-ion interaction and aggregation [49, 50]. It has been determined that there is an isochoric pressure increase due to volume expansion of the difluoromethane solvent which causes this sharp change in pressure and conductivity in these electrolytes. It is hypothesized that when the cell is filled at -60 °C and the valve shut, the entire volume of the cell is occupied with liquid solvent and unsolubilized salt, with no gaseous solvent. As the liquid solvent solubilizes the salt, the total occupited volume of the newly formed electrolyte decrease

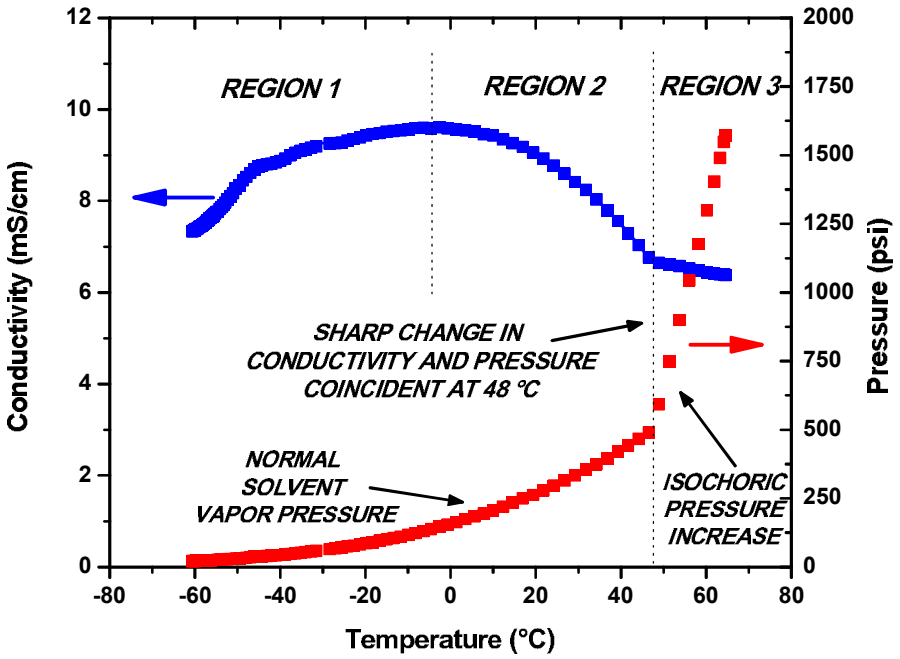

Figure 4.1: Conducutivity and pressure vs. temperature of 0.1 M $TBAPF_6$ in difluoromethane.

slightly, leaving a small volume of solvent in the gaseous state in the cell. When the temperature increases, the solvent (mixed with salt as an electrolyte) volume will expand. At a certain temperature, the volume of liquid solvent will expand to occupy the entire cell volume and any more thermal expansion will be constrained and result in a sharp isochoric pressure increase with the solvent volume expansion pressing against the cell walls. The exact temperature where this sharp increase in pressure will occur is dependent on the volume of gaseous solvent that resulted from the salt solubilization process. The higher the concentration of salt, the lower the liquid solvent fill volume will be and a proportionately higher gaseous solvent volume will be present. This lower liquid volume

will require a higher temperature for the solvent volume expansion to reach the full cell volume and show the sharp increase in pressure. This has been verified by testing electrolytes with four different concentrations of $TBAPF_6$ in difluoromethane, as shown in Fig. 4.2. The sudden change in conductivity, which is correlated with a sharp increase in pressure as seen in Fig. 4.1 increases with salt concentration with concentrations of 0.02, 0.1, 0.2 and 0.5 M showing sharp changes at temperatures of approximately 35, 48, 60, and 79 °C, respectively. It is also noteworthy to see the peak in conductivity shifts to higher temperatures with higher salt concentration. This suggest that the lowering viscosity of the solvent is the dominant mechanism in conductivity as compared to the lowering dielectric constant of the solvent.

Conductivities of electrolytes with 0.1 M $TBAPF_6$ based on difluoromethane solvent and conventional organic solvents are shown in Fig. 4.3 with their 20 °C and -40 °C conductivity data shown in Table 4.1. Acetonitrile based electrolytes are generally considered to have exceptionally high electrolyte conductivities due to the solvent's low viscosity, showing conductivites of 11.3 and 5.6 $mS \cdot cm^{-1}$ compared to <2 and <1 $mS \cdot cm^{-1}$ for other organic solvents at +20 and -40 °C, respectively. Therefore, it is very encouraging to see difluoromethane based electrolytes with an electrolytic conductivity of 9.0 $mS \cdot cm^{-1}$ at +20 °C, which is very comparable to 11.3 $mS \cdot cm^{-1}$ for acetonitrile. Even more, the difluoromethane based electrolyte has superior conductivity compared to the acetonitrile based electrolyte at temperatures $<+5$ °C. This is thought to be due to the exceptionally low viscosity of difluoromethane, 0.11 cP, compared to acetonitrile (0.34 cP). Further, the freezing point of difluoromethane (-136 °C) is much lower than

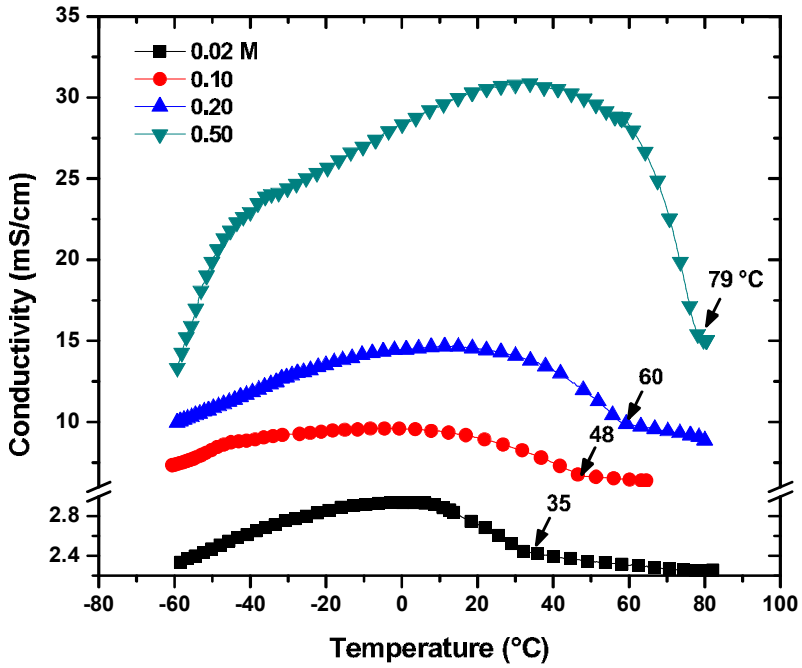

Figure 4.2: Conductivity of various concentrations of $TBAPF_6$ in difluoromethane.

that of acetonitrile (-46 °C), allowing for highly conductive electrolytes at very low temperatures.

The exceptional ability to form highly conductive electrolytes at low temperatures, difluoromethane based electrolytes could find use in electrochemical capacitors for applications requiring low temperatures. Recently, Brandon et. al. found a good candidate electrolyte for low temperature electrochemical capacitors composed of 0.5 M $TEABF_4$ in 1:1 acetonitrile:dioxolane [13]. Fig. 4.4 compares this electrolyte to an electrolyte composed of 0.5 M $TBAPF_6$ in difluoromethane, which shows significantly higher conductivities at temperatures from -60 to +30 °C. Table 4.2 compares the electrolytic

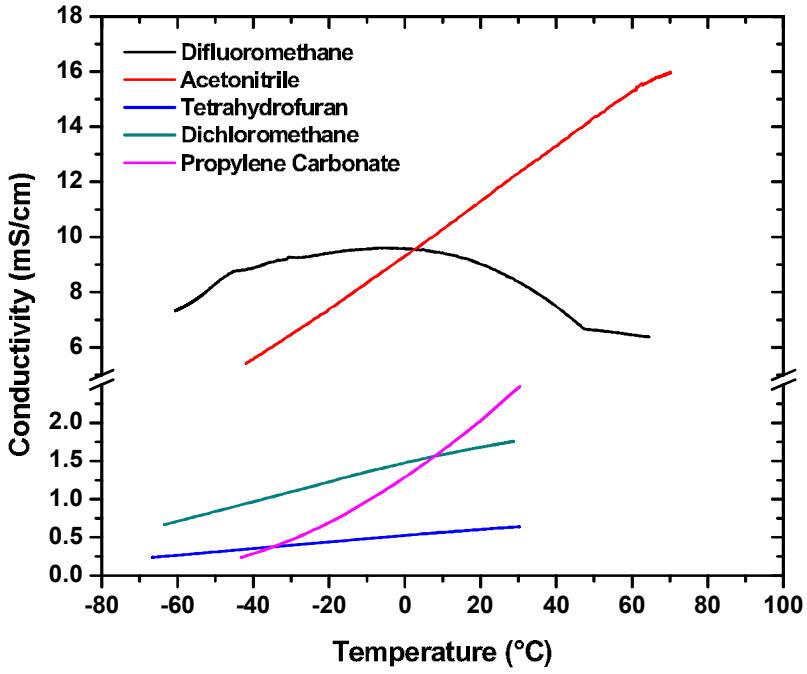

Figure 4.3: Conductivity vs. temperature of 0.1 M $TBAPF_6$ in various solvents.

conductivity of these electrolyte systems. The two have comparable conductivities at 20 °C (DFM = 30.0, ACN:DIOX = 24.2), but the difluoromethane based solvent is nearly twice as conductive at -40 °C (23.3 vs. 12.5 $mS \cdot cm^{-1}$) and -60 °C (13.4 vs. 7.5 $mS \cdot cm^{-1}$). These are the highest electrolytic conductivities ever reported for a non-aqueous electrolyte at these temperatures, to the author's knowledge.

In addition to $TBAPF_6$, many salts have been shown to form highly conductive solutions in difluoromethane. Fig 4.5 compares difluoromethane based electrolytes with various salts at 0.02 M concentration. Electrolytic conductivities ranging from 1 to 3 $mS \cdot cm^{-1}$ were seen over a similarly wide temperature range from -60 °C to +80 °C.

Table 4.1: Electrolytic Conductivities of Electrolytes Containing 0.1 M $TBAPF_6$.

Solvent	Conductivity / $mS \cdot cm^{-1}$	
	20 °C	-40 °C
Difluoromethane	9.0	8.9
Acetonitrile	11.3	5.6
Tetrahydrofuran	0.6	0.3
Dichloromethane	1.7	0.9
Propylene Carbonate	2.0	0.3

Table 4.2: Low temperature electrolytic conductivities of comparative electrolytes.

Solvent	Electrolytic Conductivity / $mS \cdot cm^{-1}$		
	20 °C	-40 °C	-60 °C
0.5 $TBAPF_6$ in DFM	30.0	23.3	13.4
0.5 $TEABF_4$ in ACN:DIOX	24.2	12.5	7.5

Multiple salts with similar anions or cations were used to qualitatively compare the ion affect on the electrolytic conductivity.

General trends show that the anion has a much greater effect on conductivity than the cation and increases in the order of $TFSI^- < ClO_4^- < BF_4^- < PF_6^-$. Because the diameter of the anions increase as $BF_4^- < ClO_4^- < PF_6^- < TFSI^-$, as seen in Table 4.3, it is thought there is strong difference in solvent ordering around the PF_6^- anion giving it higher mobility. It is unclear whether there is increased anion solvation around PF_6^- for

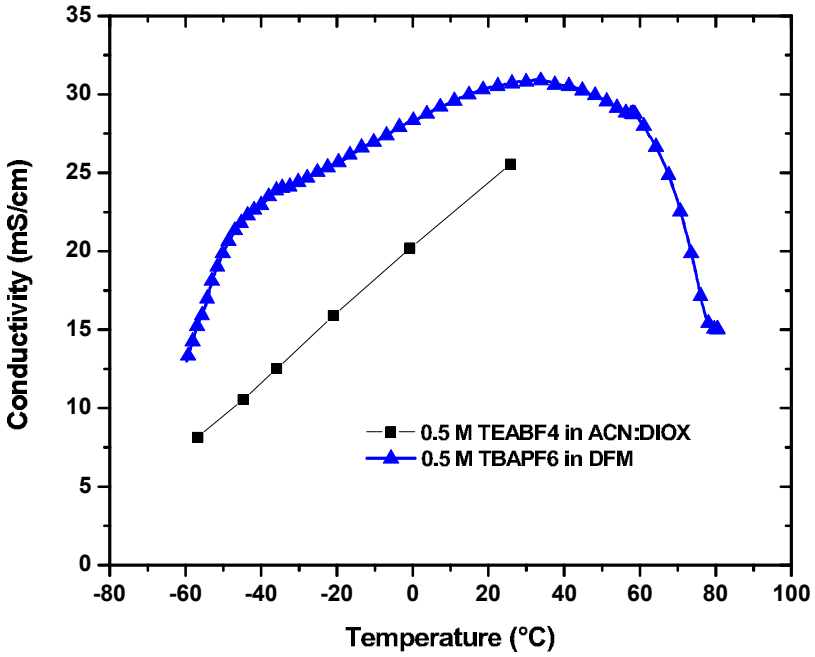

Figure 4.4: Comparison of conductivity of two low temperature electrolytes developed for electrochemical capacitor devices. The 0.5 M $TEABF_4$ in 1:1 ACN:DIOX data was used from Ref. [13]

better charge screening and less ion-ion interaction or lower solvation for a higher anion mobility with a smaller solvation shell.

In addition to difluoromethane, five other fluorinated compressed gas solvents were explored. The electrolytic conductivity of 0.1 M EMITFSI in these solvents is shown in Fig. 4.6. All electrolytes show the same general shape as described previously in Fig. 4.1, with an increase and a decrease in conductivity with increasing temperature. The electrolytic conductivity increased in the order of TFE <FP <FE <DFE <FM <DFM, clearly showing that the size of the alkane chain has a large effect. The fluorinated methane based solvents (FM,DFM) are the highest conducting electrolytes likely because

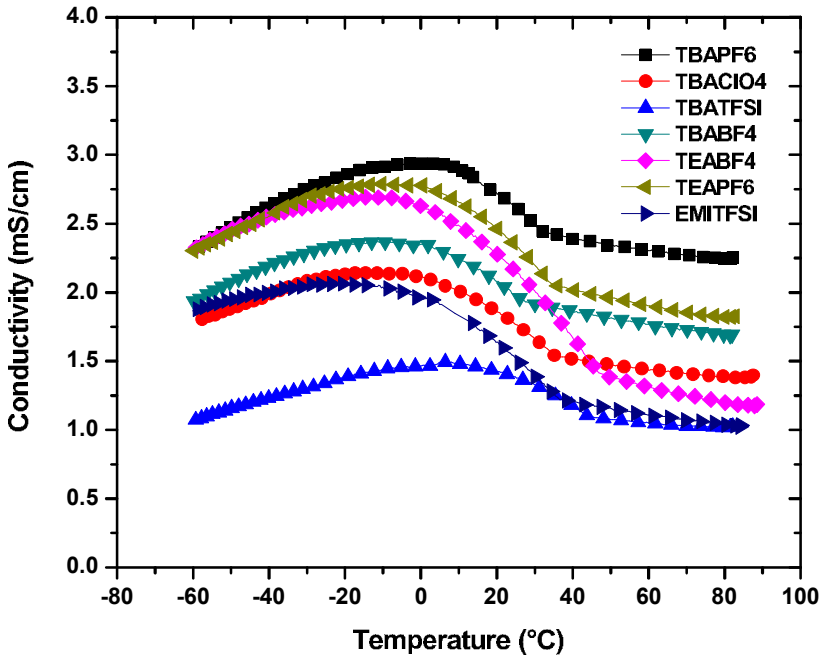

Figure 4.5: Conductivity electrolytes composed of various salts at 0.02 M concentration in difluoromethane.

of the very small radius and low viscosity. The fluorinated ethane based solvents FE and DFE showed the next highest conductivities followed by FP and TFE. TFE showed a slightly lower conductivity than FP, probably because it could not form an ideally ordered solvent shell around the ions due to the large asymmetry of the four fluorine atoms.

In order to determine the potential window of the solvents studied, cyclic voltammetry studies were conducted. Fig. 4.7 shows cyclic voltammetry spectra of 0.1 M EMITFSI in four fluorinated compressed gas solvents. Although the curves show considerable impurities, likely from the solvents themselves, they all show a roughly 4.2 V potential window. However, it has been determined the oxidation and reduction cur-

Table 4.3: Radius of selected ions explored [15, 16].

Ion	Formula	Radius (nm)
Li^+	Li^+	.076
EMI^+	$C_6H_{11}N_2^+$	.304
TEA^+	$(C_4H_9)_2N^+$	.336
TBA^+	$(C_4H_9)_4N^+$	.441
BF_4^-	$BF_4{}^-$	.227
ClO_4^-	ClO_4^-	.236
PF_6^-	PF_6^-	.254
$TFSI^-$	$(SO_2CF_3)N^-$	.326

rents occurs as a result of the salt decomposition, not the solvent itself, and is in strong agreement with previously determined potential limits of this salt [51].

4.3.2 Lithium Based Electrolytes

Lithium based salts are unique in that they are considerably harder to dissolve than most salts. This is because lithium is the smallest possible ion, after hydrogen, and requires high coordination to the solvent for adequate solubility. In addition, a high dielectric solvent is required to suitably screen the high charge density of the lithium cation from the anion in order to prevent ion aggregation. It was found that of the six fluorinated solvents explored, only the three monofluorinated solvents, FM, FE, and FP,

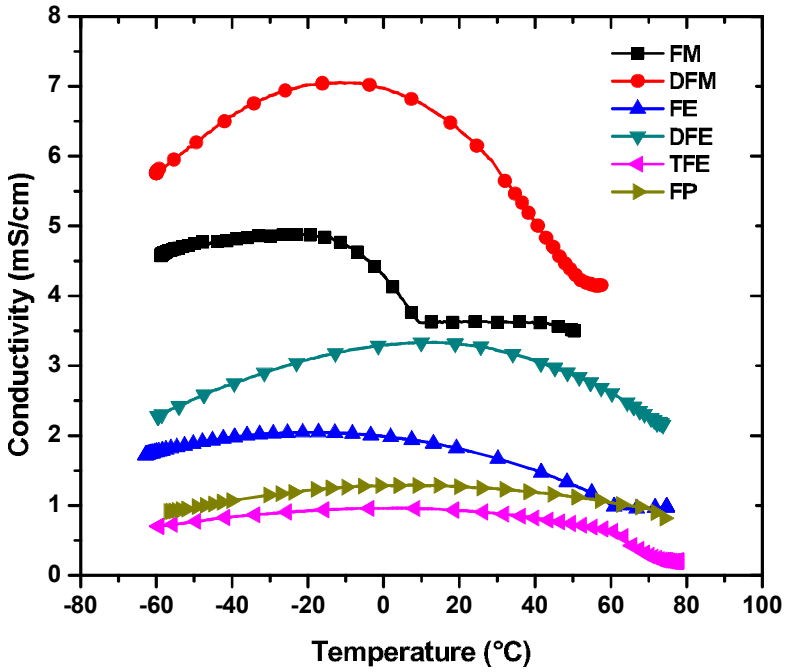

Figure 4.6: Conductivity of 0.1 M EMITFSI in various solvents.

were able to solubilize Li based salts. This is thought to be because the dipole moment of these solvents align directly along the axis of the highly electronegative fluorine atom, allowing good coordination and close proximity lithium cation to the solvent. In addition, it was found that the only lithium salt studied that forms highly conductive solutions was LiTFSI. The $TFSI^-$ anion, known for having high charge delocalization, aids the already difficult to solubize cation. The conductivity of 0.1 M LiTFSI in the three compatible fluorinated compressed gas solvents and a compataive example with propylene carbonate is shown in Fig. 4.8. The fluoromethane based electrolyte shows the highest conductivity of the three electrolytes, showing a conductivity of over 1 $mS \cdot cm^{-1}$ from -60 to +10

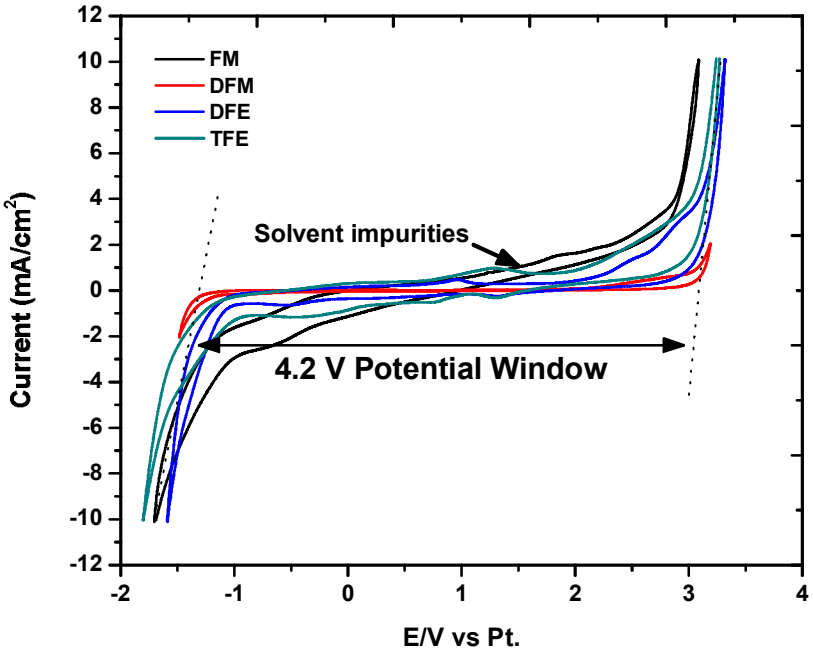

Figure 4.7: Cyclic voltammetry spectra of 0.1 M EMITFSI in various fluorinated compressed gas solvents. All spectra were taken at 20 °C at a 100 mV·sec^{-1} sweep rate using platinum working, counter and reference electrodes.

C. This remarkable conductivity down to -60 °C is the first, to the author's knowledge, for any lithium based electrolyte. Indeed, the comparative propylene carbonate based electrolyte shows a significantly decreased conductivity of about 0.3 mS·cm^{-1} at -20 °C. Further, a conductivity of 1 mS·cm^{-1} is suitable for automotive applications and is displayed at a low salt concentration of 0.1 M. This conductivity, however, is shown to decline sharply at higher temperatures and to below 0.1 mS·cm^{-1} at 40 °C. It is thought this is due to the rapid decline in the dielectric constant of this solvent and high ion aggregation and loss of solubility. However, external application of increased pressure may improve this conductivity, as shown before in Fig. 4.1. It is thought that higher

concentrations would also yield even higher conductivities. Neither of these options has yet been explored.

The electrolytic conductivity of the FE and FP based electrolytes show conductivities around 0.5 to 0.25 $mS \cdot cm^{-1}$, significantly lower than the FM based electrolyte. Further, the FE based electrolyte shows a steady decline of electrolytic conductivity through the temperature range explored (-60 to +100 °C) rather than an increase followed by a decrease in conductivity as observed for all other electrolytes examined. This is thought to be due to the poor solubility of the salt in this solvent resulting in high aggregation of the salt.

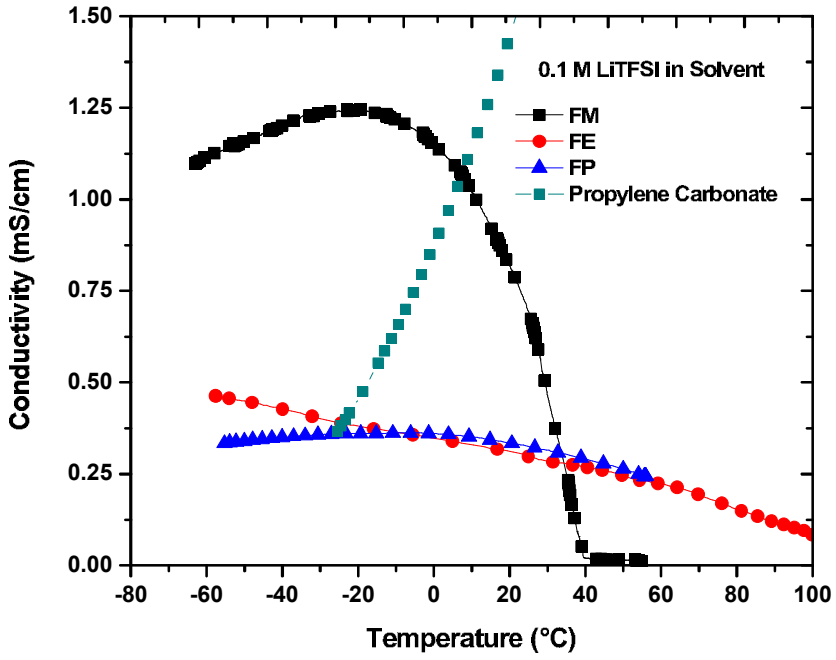

Figure 4.8: Conductivity of 0.1 M LiTFSI in various mono-fluorinated solvents and a comparative example with propylene carbonate.

The potential window of 0.1 M LiTFSI in fluoromethane was examined by cyclic voltammetry and shown in Fig. 4.9. At 20 °C, there are many impurities shown in the electrolyte system, however, a clear oxidation limit is seen at about 5.5 V vs. Li. As will be seen in Chapter 7, there is likely a reduction current contribution from the reduction of the solvent since it is known the solvent can be continuously reduced (no SEI formed) at these low reduction potentials, although this is expected to be a small contribution. To obtain a cleaner spectra and determine the real potential limits of the electrolyte, cyclic voltammetry was also conducted at -60 °C. At this low of a temperature, the impurity decomposition kinetics are significantly lowered and only the salt and solvent limits are observed. Firstly, the lithium platting and stripping peaks are very clearly defined and which are used to convert the potentials from the platinum reference to lithium reference potentials. There are no other observed peaks in the spectra till the oxidation at 5.5 V vs. Li. It has been determined this oxidation is due to the $TFSI^-$ anion and not the solvent for two reasons. Since it is known the conductivity, and hence ion diffusion, of the electrolyte is reduced at 20 °C (0.85 vs. 1.1 $mS \cdot cm^{-1}$ at +20 and -60 °C, respectively), it is expected the slope of the oxidation curve would change if the oxidation reaction were diffusion controlled, which it does indeed show. Further, the oxidation potential of 5.5 V vs. Li agrees well with previous measurements of the oxidation of the $TFSI^-$ anion [51, 52]. Therefore, it has been shown the oxidation potential of the fluoromethane solvent itself is stable at these high potentials.

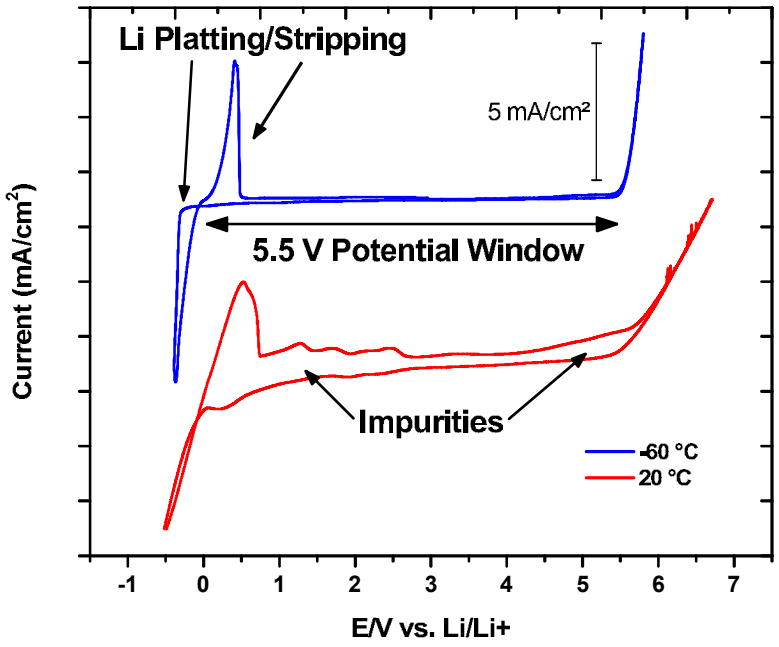

Figure 4.9: Cyclic voltammetry spectra of 0.1 M LiTFSI in fluoromethane at +20 and -60 °C with a 100 mV·sec^{-1} sweep rate using a Pt working, counter and reference electrodes. Potentials converted to lithium by taking the average of the platting/stripping peaks.

4.4 Conclusion

It has been shown that six fluorinated compressed gas solvents (fluoromethane, difluoromethane, fluoroethane, 1,1-difluoroethane, 1,1,1,2-tetrafluoroethane, 2fluoro-propane) may be used to form highly conductive electrolyte systems with wide potential windows. With non-lithium based salts, difluoromethane shows the highest conductivity amongst the solvents and conductivities as high as 30 mS·cm^{-1} at +20 °C and 13 mS·cm^{-1} at -60 degree C have been demonstrated. Fluoromethane shows the highest conductivity with lithium based salts, showing conductivities >1mS·cm^{-1} from -60 to +10 °C. Further, there is clearly a high pressure effect that is able to change the

conductivity of these electrolytes drastically. One may imagine engineering a system that applies an external pressure to these systems in order to increase conductivity and optimize electrolytes.

The potential window of these solvents has also been shown to be very wide. It has been demonstrated with EMITFSI, the potential limits of four electrolytes formed with the fluorinated compressed gas solvents are limited by the decomposition of the EMITFSI salt itself. With a lithium based salt in fluoromethane, the oxidation potential of the solvent is >5.5 V vs. Li. This high oxidation potential may allow for use of high voltage cathodes for increased energy density of lithium-ion batteries.

Chapter 5

Electrochemical Double Layer Capacitors Based on Compressed Gas Electrolytes

Electrochemical double-layer capacitors using a compressed gas solvent based electrolyte composed of difluoromethane are explored. The benefit to the use of these solvents are their considerably high electrochemical stability for potentially higher voltage operation, low viscosity for high electrolytic conductivity, and low melting point for low temperature operation. It is found that the electrolyte allows operation down to below -70 °C, compared to -40 °C with state-of-the-art acetonitrile based electrolytes. Further, the capacitance is also very comparable to the state-of-the-art.

5.1 Introduction

Electrochemical double-layer capacitors (EDLCs) are energy storage devices with a significantly higher power capability and longer life compared to battery devices. They have applications ranging from pulse power for remote sensors to start-stop in automotives. Typically, their exceptional low temperature performance is due to the use of acetonitrile as the electrolyte solvent, which is a highly toxic material. The less toxic propylene carbonate is also commonly used, but at a sacrifice of power and energy density, and operation temperature range. Further, as seen in Section 1.1.2, the energy density of EDLCs are given by Eqn. 1.2, which scales with V^2, and so it is important to increase the voltage of the device. Typically, this voltage is partially limited by the electrolyte, particularly the solvent. The need for a solvent with low toxicity and improving both the temperature and energy density requirements is crucial to enable new technologies.

As discussed in Chapter 2, fluorinated compressed gas solvents offer an alternative to conventional solvents. These solvents have exceptionally low melting points and so high conductivity electrolytes are expected at very low temperatures as well as very wide electrochemical potential windows, as shown in Section 4.3.1 and elsewhere [49, 50, 53–56]. Lastly, these solvents are non-hazardous and suitable for many applications. The use of the fluorinated compressed gas solvent difluoromethane for use in EDLC devices is explored here.

5.2 Experimental

For smaller sized cells (a few Farads), electrodes were fabricated by first mixing activated carbon (YP50), carbon black (Super C65, Timcal) and PTFE (60 wt.% aqueous solution, Sigma) in a ratio of 90:5:5 into a viscous aqueous slurry. The slurry was then dried in a convection oven at ca. 80 °C and the dried powder was rolled into a sheet which electrodes were then punched out of into a disc shape and vacuum dried at ca. 200 °C. Cells were assembled as shown schematically in Fig. 5.1. Two stainless steel 316 current collectors were used to make electrical contact to the carbon electrodes. The current collectors had a small portion which was sputter coated with platinum in order to solder electrical connections, which were then epoxied over to avoid electrical contact with electrolyte. A separator (Celgard) was placed between the electrodes to avoid shorting. The cell was held together under mild pressure with a few wraps of PTFE tape. For larger sized cells (100 Farads), cells were purchased (PowerStor, 1860 size), opened, and thoroughly washed with acetonitrile to remove the salt and vacuum dried at ca. 100 °C to remove the solvent. For both types of cell, the entire cell and salt ($TBABF_4$ or $TEABF_4$, Sigma-Aldrich, electrochemical grade, >99% purity) was then inserted into a pressure vessel and shut under argon atmosphere. Vacuum was then briefly pulled on the cell through a valve and subsequently cooled to ca. -60 °C. Difluoromethane (Synquest Laboratories, >99%) was then introduced into the cell in gaseous form by evaporation from a pressurized liquid state at room temperature, which was then condensed back to a liquid state inside the cooled cell. After solvent filling, the valve was again shut and

allowed to warm to room temperature. The cell mass was measured before and after solvent filling to verify the cell was completely filled with liquid solvent.

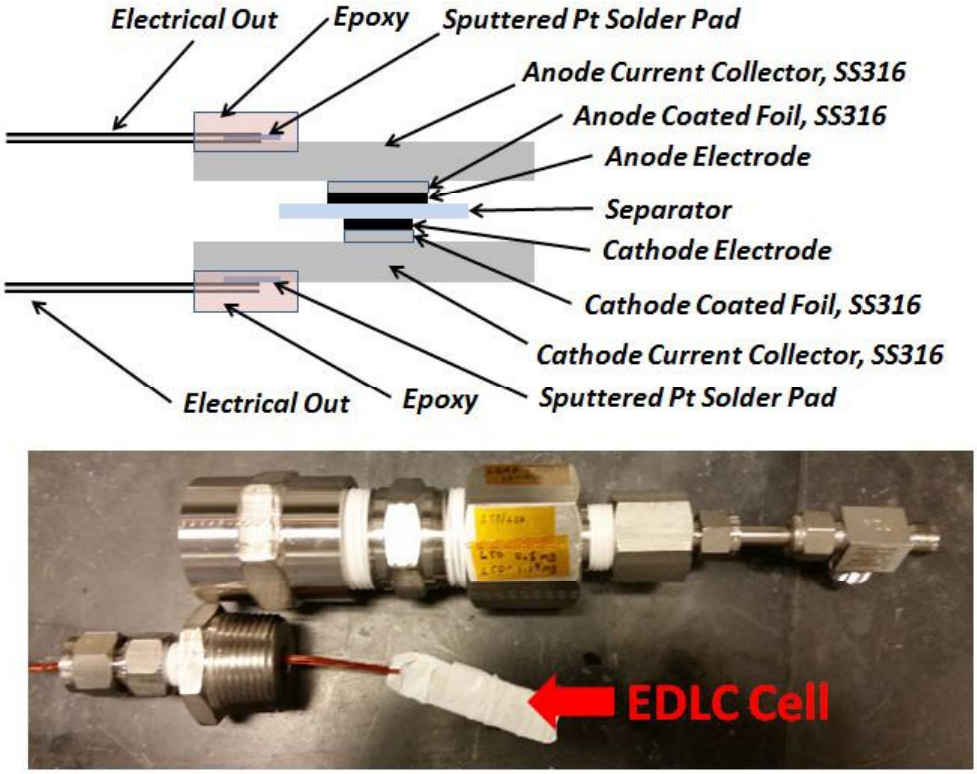

Figure 5.1: Schematic and image of EDLC cell assembly.

Cells were cycle tested with a battery cycle tester (Arbin Instruments) and placed in a convection oven (Espec) at various temperatures. The small coin cell sized EDLCs were cycle tested at room temperature with a 20 mA constant current charge up to 3.0 V, held at this voltage for 1 hour, followed by a 20 mA constant current discharge to 0.1 V. The larger 100 F cells were cycle tested at various temperatures with a 100 mA constant current charge up to 2.5 V (propylene carbonate) or 2.7 V (acetonitrile and difluoromethane), held at this voltage for 1 hour, followed by a 100 mA constant current

discharge to 0.1 V. The capacitance was calculated from the discharge curve between 80% and 40% of the full voltage (2.16-1.08 V for 2.7 V devices and 2.0-1.0 V for 2.5 V devices). Electrochemical impedance measurements (Bio-Logic) was typically done with a small 10 mV sine wave test signal.

5.3 Results and Discussion

5.3.1 1 F Coin Cells

One benefit to using the difluoromethane based electrolyte for EDLCs is for enabling exceptional low temperature performance. Figure 5.2 compares the resistance of two similar EDLC cells with electrolytes based on either conventional acetonitrile or difluoromethane compressed gas solvent. The resistance of the acetonitrile electrolyte increases considerably at around -40 °C. As is well known, the resistance of devices using acetonitrile based electrolytes increase substantially around this temperature, which limits the useful low temperature range of this electrolyte [2, 13, 22, 46, 57]. However, the resistance of the difluoromethane based cell remains fairly low and only begins to increase considerably around -75 °C. This allows for the low temperature operation to be extended by 35 °C with a non-toxic solvent, which would be a highly preferred alternative to the toxic acetonitrile.

Impedance spectroscopy measurements were performed on the difluoromethane based cell to confirm the low temperature behavior, with nyquist plots at various temperatures shown in Fig. 5.3. The point at which all the curves meet at the high frequency

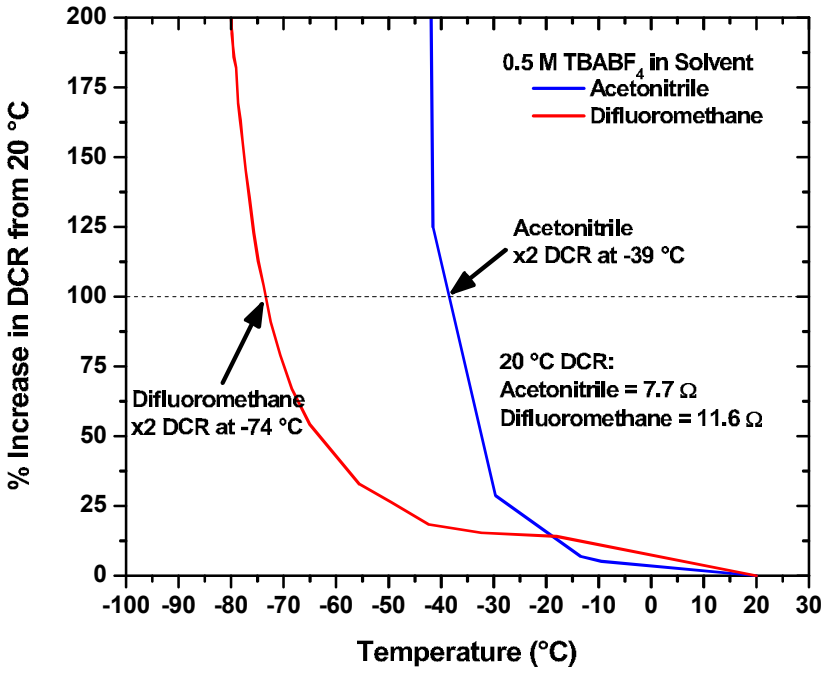

Figure 5.2: Cell resistance vs. temperature for two similar EDLC cells with 0.5 M $TBABF_4$ in acetonitrile and difluoromethane.

point around 5 Ω is representative of the cell contact resistance, R_c, while the semi-circle is representative of the electrode charge resistance and the 45°portion is due to the Warburg diffusion resistance [2, 22]. While the contact resistance is insensitive to a change in temperature, the electrode charge resistance is comprised of both the electrical and ionic resistance through the electrode material. This semi-circle increases only slightly from -40 to -70 °C. Since the electrode electrical resistance is essentially unchanged with temperature, the slight change in electrode charge resistance is primarily due to an increase in the ionic resistance. This matches well with the previous data shown in Fig. 5.2, showing the cell resistance increases about 70% up to -70 °C, after which the

resistance increases considerably.

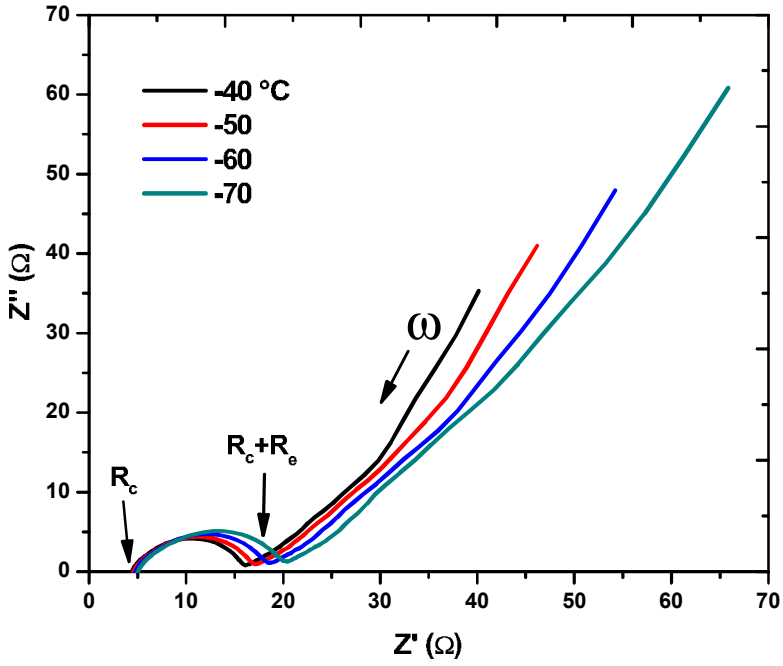

Figure 5.3: Nyquist plots vs. temperature for an EDLC cell composed of 0.5 M $TBABF_4$ in difluoromethane.

Capacitance and DCR were recorded each cycle, shown in Fig. 5.4. The resistance of the cell is seen to increase continuously with cycling from an original value of 6.35 Ω and the capacitance seen to decrease steadily from an original value of 1.46 F after nearly 400 cycles. It is thought that this cell failure could be due to the increased voltage applied to the cells and the mechanical construction of the cells not being ideal.

The capacitance and maximum voltage of the devices was also explored by cyclic voltammetry, seen in Fig. 5.5. The capacitance can be measured from the discharge portion of the curve by

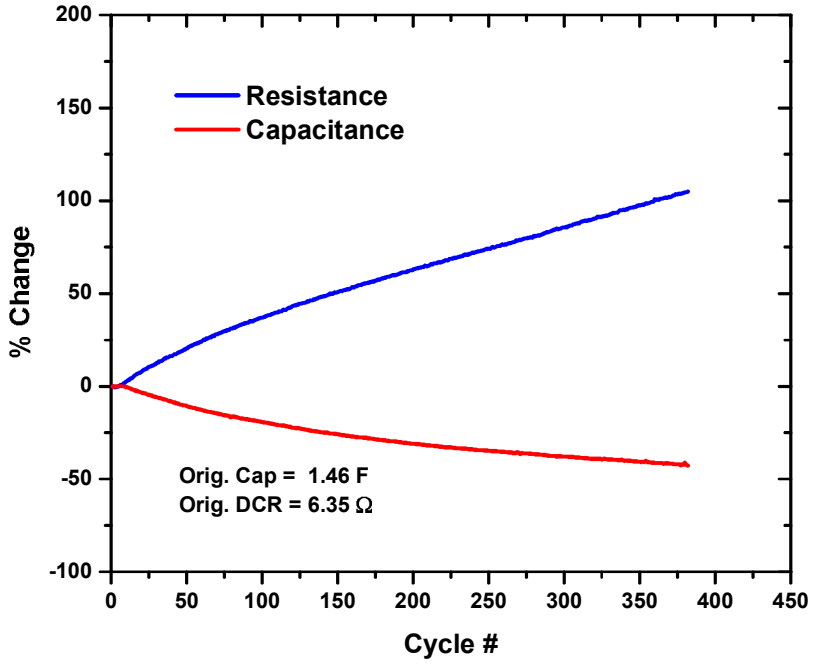

Figure 5.4: Capacitance and resistance of coin-cell sized EDLC cell with 0.5 M $TBABF_4$ with cycling at room temperature.

$$C = I/\nu \tag{5.1}$$

where C is the capacitance in Farads, I is the current in Amps, and ν is the sweep rate in $mV \cdot sec^{-1}$. The discharge curves for all three cells are approximately 3 mA with a sweep rate of 2 $mV \cdot sec^{-1}$, giving a cell capacitance of around 1.5 F, as expected from the constant current discharge calculations. The voltage limit can be qualitatively described by the increase in charge current at high voltages. It is clear the acetonitrile based cell has an earlier increase in oxidation current, as shown by the inset in the plot. This shows the device has a lower voltage stability than the difluoromethane device. This voltage

limit can be due to two factors; the stability of the electrolyte or unwanted impurities on the activated carbon electrode. If a cleaner electrode was used, it is possible an increased voltage device would be possible.

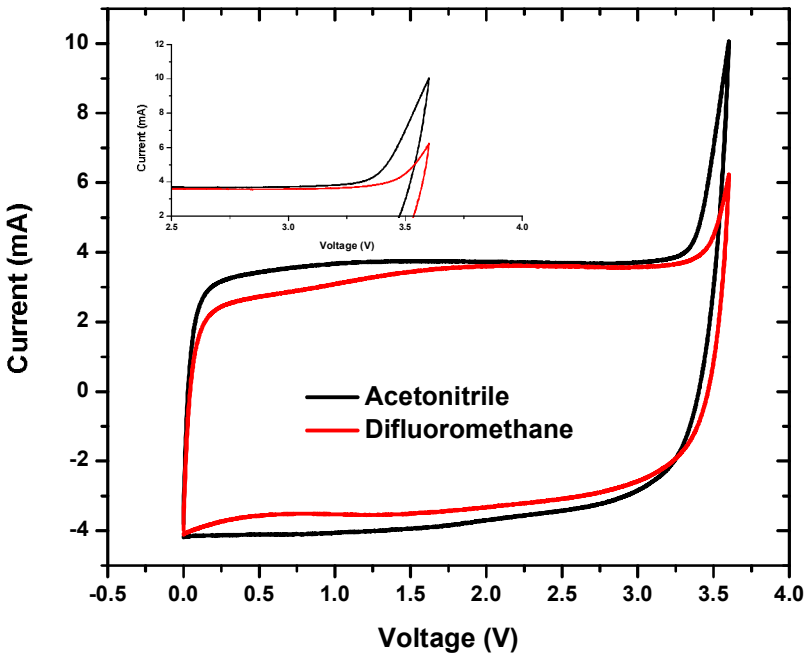

Figure 5.5: Room temperature cyclic voltammetry curves of EDLC cells with 1.0 M $TBABF_4$ with various solvents with a sweep rate of 2 $mV \cdot sec^{-1}$.

5.3.2 100 F Cells

Commercially manufactured 100 F cells were purchased in order to determine if the life cycle behavior of the cells would be improved with properly manufactured cells. Fig. 5.6 compares the capacitance of the difluoromethane based cell with similar commercially available cells based on acetonitrile and propylene carbonate with cycling

at +20 °C and +60 °C. At 20 °C, the capacitance retention out to 30 cycles is very comparable for all the cells studied, shown in Fig. 5.6a. It is noteworthy that the capacitance of the difluoromethane based cell is almost identical to that of the acetonitrile cell. This is interesting since the capacitance is thought to scale with the dielectric constant of the solvent, whereas here the difluoromethane solvent has about a three times lower dielectric constant than acetonitrile. At 60 °C, the difluoromethane clearly high higher capacity retention than that of the acetonitrile based device to 40 cycles, shown in Fig. 5.6b. This accelerated temperature ages the capacitor much faster at room temperature and is a good gauge of life stability.

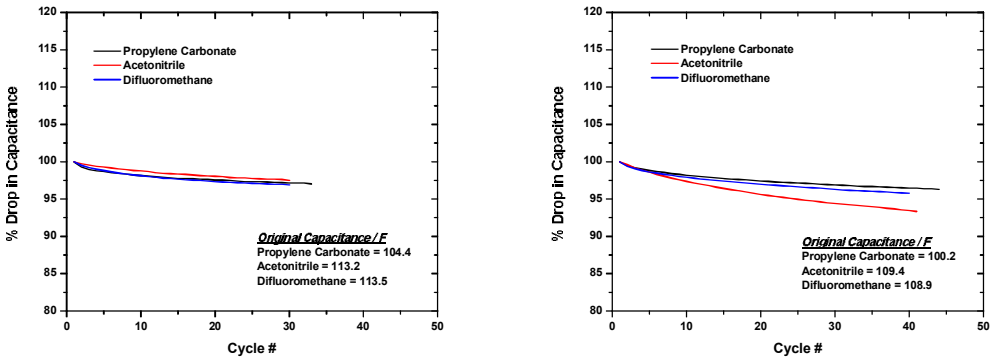

(a) (b)

Figure 5.6: Capacitance over a number of cycles of three similar EDLC devices using various solvents at (a) +20 °C and (b) +60 °C.

The temperature performance of the three cells was also examined, shown in Fig. 5.7. The resistance increase as a function of temperature for the cells are compared in Fig. 5.7a. The propylene carbonate based cell has the highest increase in resistance and increased significantly after -20 °C. The acetonitrile and difluoromethane based cells both

had comparable resistance at 20 °C. While the acetonitrile based device had the lowest resistance up to -40 °C of the three cells, the resistance significantly increased below -40 °C while the difluoromethane based cell resistance remained comparably low down to -70 °C. It is expected the capacitance does not drop significantly with temperature, and this is verified by Fig. 5.7b. It is seen that there is very little capacitance drop in any of the three cells within their temperature limits. This is important since at low temperatures, the device is still expected to show high capacitance retention for maximum energy content.

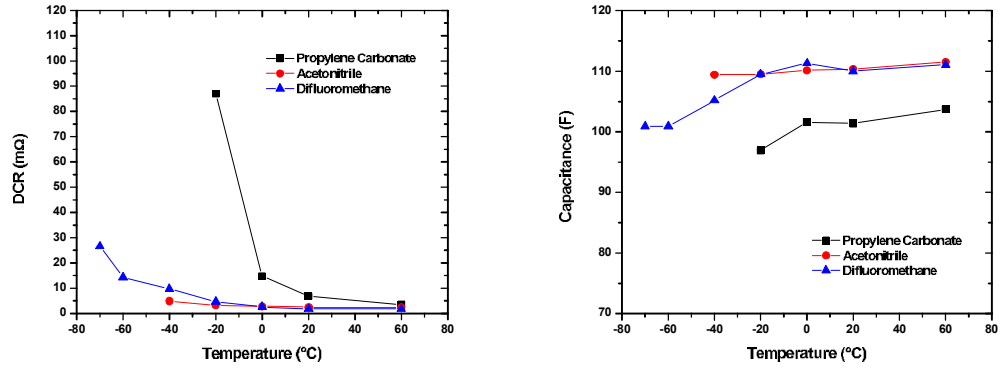

(a) (b)

Figure 5.7: The (a) DCR and (b) capacitance as a function of temperature of three similar EDLC devices using various solvents.

The capacitance and maximum voltage of the devices was also explored by cyclic voltammetry, seen in Fig. 5.8. The discharge curves for all three cells is approximately 500 mA with a sweep rate of 5 $mV \cdot sec^{-1}$, giving cell capacitance of around 100 F, as expected from the constant current discharge calculations. The voltage limit can be qualitatively described by the increase in charge current at high voltages. It is clear the propylene carbonate based device has an earlier increase in current as compared to the

other two devices, as shown by the inset in the plot. This shows the device has a lower voltage stability, as is known in the industry. The acetonitrile and difluoromethane devices both show an increase in current at about the same voltage, showing that neither has a substantial voltage benefit over the other. This voltage limit can be due to two factors; the stability of the electrolyte or unwanted impurities on the activated carbon electrode. If a cleaner electrode was used, it is possible a voltage benefit using difluoromethane would become apparent.

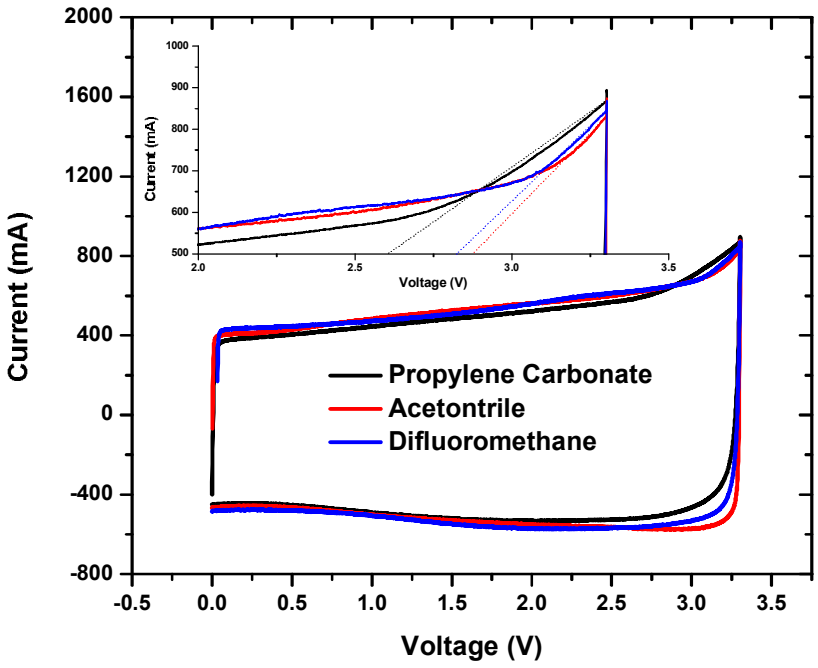

Figure 5.8: Room temperature cyclic voltammetry curves of EDLC cells with 1.0 M $TEABF_4$ with various solvents with a sweep rate of 5 $mV \cdot sec^{-1}$.

5.4 Conclusion

Electrochemical double-layer capacitor devices using an electrolyte based on the compressed gas solvent difluoromethane were built and tested. A clear advantage in low temperature performance is found with the difluoromethane based device, with operating temperatures as low as -75 °C demonstrated. The capacitance of the device is very comparable to state-of-the-art acetonitrile based devices. Although it is thought the solvent could offer increased device voltage as well, it is apparently limited more by the electrode purity itself. Future work will explore this solvent with higher purity carbons for demonstration of high voltage devices.

Chapter 6

Lithium-Ion Batteries Based on Compressed Gas Electrolytes

For the first time, lithium-ion battery cathodes are demonstrated to operate using a compressed gas solvent based electrolyte. Using fluoromethane as a solvent and lithium bis(trifluoromethyl-sulfonyl)imide as a salt, exceptionally low temperature performance down to -60 °C for $LiCoO_2$ and $LiMn_{1.5}Ni_{0.5}O_4$ cathodes are demonstrated with reasonably high charge-discharge efficiencies and good cycling behavior as low as -60 °C.

6.1 Introduction

Li-ion batteries are indispensable in modern technology due to their high energy density. There are many battery electrodes, both anode and cathode, currently being

explored to further increase this energy density [17, 58–60]. However, it is generally accepted the electrolyte limits the voltage, and in turn the overall energy density, of these battery devices and is a intense area of research [10, 29, 32, 47, 61, 62]. Because the oxidation of conventional electrolytes occurs around 4.5 V vs. Li, high voltage cathodes such as spinel $LiMn_{1.5}Ni_{0.5}O_4$ cannot be used without significant capacity fade over even a few cycles. Therefore, it is important to find electrolytes that have stability limits that allow the use of these materials.

The use of the highly electronegative fluorine is desirable in solvents since it tends to increase the solvents oxidation potential. There has been much interest in the fluorination of conventional solvents [32] which indeed increase the oxidation potential of electrolytes containing them. However, increased viscosity or an undesirable temperature range may result. However, nobody has previously tried using solvents that are typically gaseous at standard temperature and pressure for lithium batteries. In particular, fluorinated compressed gas solvents show moderate polartiy and dielectric constants [4–9, 48, 63–65], wide potential windows, and can form highly conductive solutions [49, 50, 53–56]. However, it has been found that solubility of the small Li^+ cation requires high coordination of the solvent to cation, and shown in Chapter 4 only the monofluorinated alkanes (fluoromethane, fluoroethane and fluoropropane) are able to solubilize lithium. Here, fluoromethane is used as electrolyte solvent since it shows high conductivity and a wide potential window. The use of this solvent as a base for lithium ion batteries has not been attempted previously and requires that the cell be contained inside a pressure vessel at all times during test and introduces some difficulty

in experimentation. However, because this is a typically gaseous solvent, viscosities are fairly low and melting points are under -100 °C, which is reflected in the exceptional low temperature performance of these devices.

6.2 Experimental

$LiCoO_2$ (LCO) and $LiMn_{1.5}Ni_{0.5}O_4$ (LMNO) active cathode materials were purchased from Sigma-Aldrich. These electrodes were fabricated by first wet mixing the active material with 10 wt% carbon black (Super C65, Timcal) and 10 wt% PVDF binder in N-methyl-2-pyrrolidone solvent overnight followed by wet coating onto appropriate substrate foil with a wire bar. The coated material was then vacuum dried in an oven at ca. 80 °C over night. Disc shaped electrodes were then punched out of the coated foil substrate and vacuum dried at 80 °C in a glovebox prior to cell assembly. Lithium metal electrodes (Sigma-Aldrich) were prepared under argon atmosphere by first scraping clean with a glass slide then rolled to a mirror finish with a glass rod. Disc shaped electrodes were then punched out of the cleaned electrode. Activated carbon electrodes were fabricated by first mixing activated carbon (YP50), carbon black (Super C65, Timcal) and PTFE (60 wt.% aqueous solution, Sigma) were mixed with a ratio of 90:5:5 into a viscous aqueous slurry. The slurry was then dried in a convection oven at ca. 80 °C and the dried powder was rolled into a sheet which electrodes were then punched out of into a disc shape and vacuum dried at ca. 200 °C.

Cells were assembled under argon atmosphere with copper current electrodes for

the anode and aluminum or stainless steel 316 current collectors for the cathode and a Celgard separator between electrodes to prevent electrical contact. The cell was held together under mild pressure with a few wraps of PTFE tape. The assembly is shown schematically in Fig. 6.1. The entire cell assembly and salt was then inserted into a pressure vessel and shut under argon atmosphere. Vacuum was then briefly pulled on the cell through a valve and subsequently cooled to ca. -60 °C. Fluoromethane solvent was then introduced into the cell in gaseous form by evaporation from a pressurized liquid state at room temperature, which was then condensed back to a liquid state inside the cooled cell. After solvent filling, the valve was again shut and allowed to warm to room temperature. The cell mass was measured before and after solvent filling to verify the cell was completely filled with liquid solvent. All experiments used 0.1 M lithium bis(trifluoromethyl-sulfonyl)imide (LiTFSI) salt, which was purchased from 3M (HQ-115) and vacuum dried at 140 °C before use. This particular electrolyte (0.1 M LiTFSI in fluoromethane) was chosen since it was previously shown that it forms electrolyte solutions with conductivity upwards of 1 $mS \cdot cm^{-1}$, as shown in Section 4.3.2.

Cells were cycle tested with a battery cycle tester (Arbin Instruments) and placed in a convection oven (Espec) at various temperatures. Electrochemical impedance measurements (Bio-Logic) were typically done with a small 10 mV sine wave test signal.

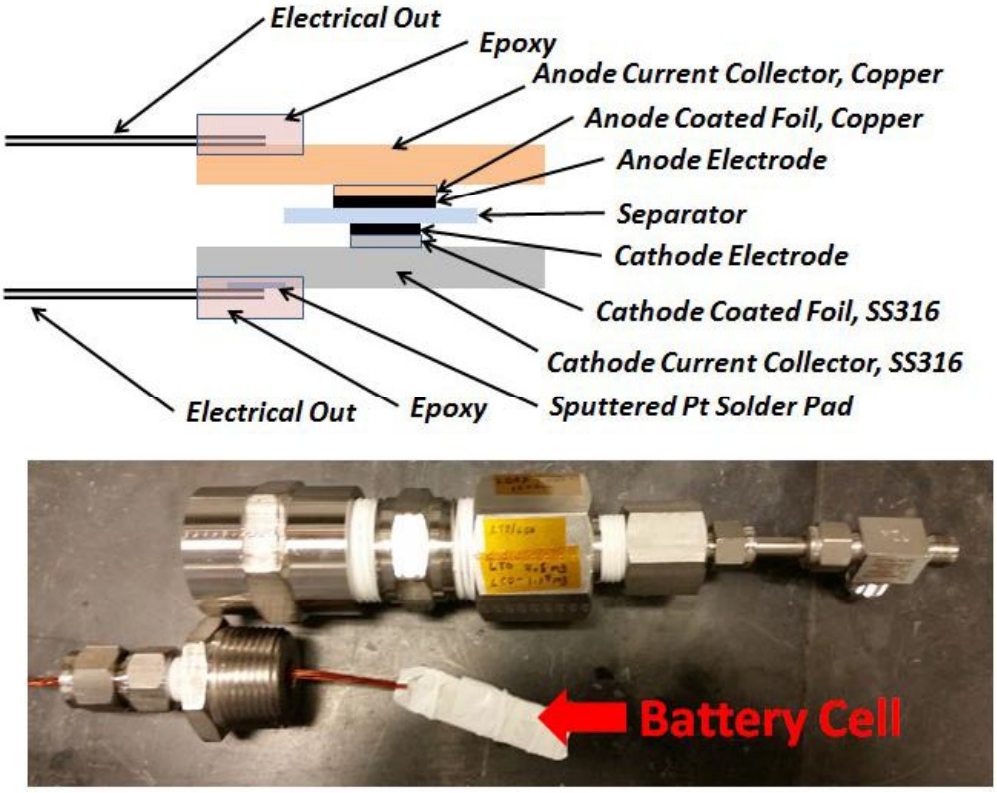

Figure 6.1: Schematic and optical image of lithium-ion cell assembly.

6.3 Results and Discussion

6.3.1 1st Cells

LMNO half-cells were first fabricated using an aluminum current collector and lithium metal counter electrode. Upon electrode cycling at the C/10 rate, it was noticed the voltage never reached the full charge voltage of 4.85 V vs. Li, but instead only reached about 4.8 V vs. Li, shown in Fig. 6.2. After about 49 hours of charging, discharge was manually initiated and the subsequent discharge took about 15 hours. This shows the spinel-LMNO was likely well over charged. It appears a high iR resistance, due to the

electrolyte, shifted all the potentials to lower values, reflecting why it would take much longer time than expected to fully charge the LMNO cathode. EIS analysis also reflects this high resistance, shown by a nyquist plot in Fig. 6.3. Both the discharged and charged electrodes show an impedance of well over 20 kΩ, showing a very high resistance and explaining the high iR-drop even at a low charge current.

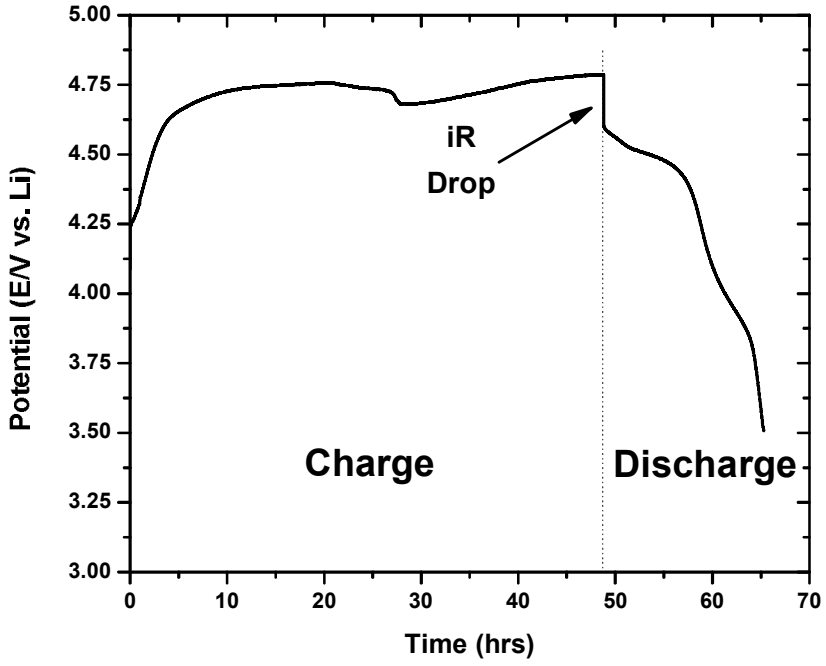

Figure 6.2: Constant current charge-discharge of a cell using an LMNO cathode and a Li-metal counter electrode at room temperature with a C/10 charge rate.

6.3.2 2nd Cells

It had been determined that the solubility of the LiTFSI salt takes some time to dissolve completely in fluoromethane solvent. In addition, temperature cycling between

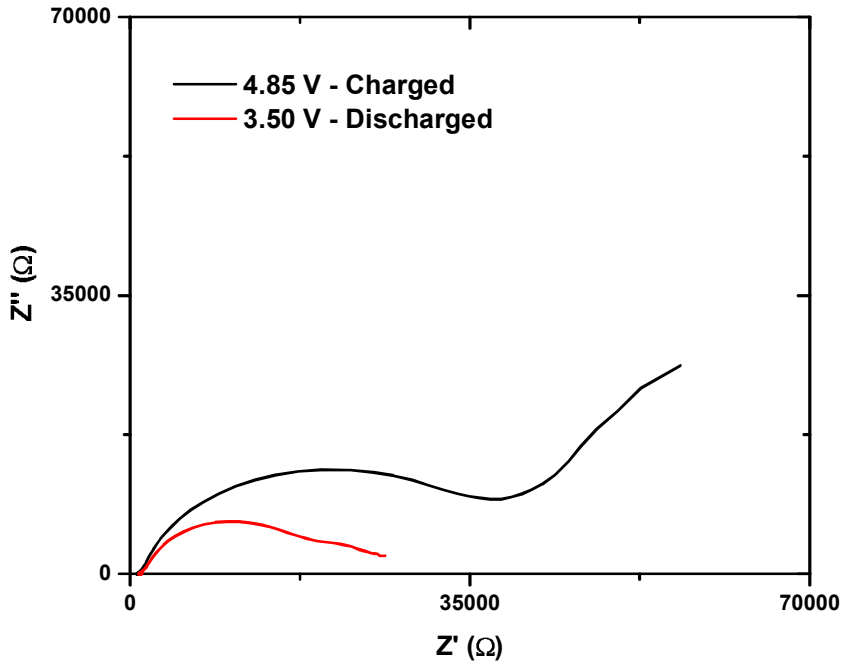

Figure 6.3: Nyquist plot of a cell using an LMNO cathode and li-metal counter electrode at room temperature.

-60 and +50 °C seems to be necessary to complete this solvation process. After proper electrolyte formation cycles were performed, LMNO half-cells with lithium metal counter electrodes were assembled. The impedance of these cells was significantly reduced, down to a few hundred ohms, seen in Fig. 6.4. This should permit good charge/discharge characteristics. Rather than do constant current charge-discharging, cyclic voltammetry was employed to ensure the controlled charge up to the full 4.85 V vs. Li charge potential. These CVs are shown over multiple cycles for the same LMNO half cell in Fig. 6.5. Over six cycles, a large oxidation current around 4.75 V vs. Li is seen, which could be due to a type of SEI formation. There is a definite redox behavior occurring with oxidation at

around 4.55 V vs. Li and reduction occurring around 4.65 V vs. Li, as shown in the inset for the 5th cycle. It is strange behavior to have the oxidation potential lower than the reduction potential, and this is thought to be due to again an increased impedance of the cell. However, it is seen here the litiation and delithiation of a working LMNO cathode.

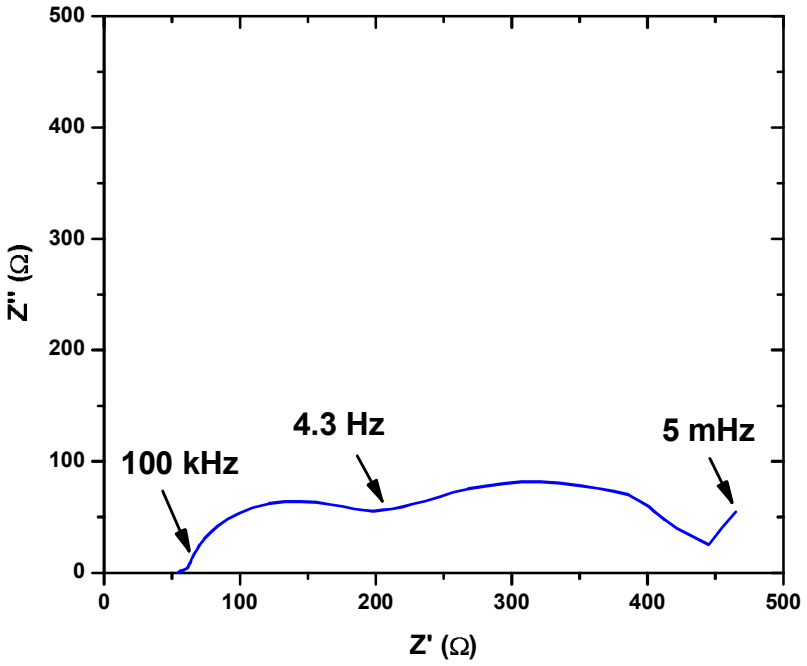

Figure 6.4: Nyquist plot of a cell using an LMNO cathode and Li-metal counter electrode at room temperature with properly prepared electrolyte.

6.3.3 3rd Cells - Activated Carbon Counter Electrode

As will be seen in Chapter 7, fluoromethane is slowly reduced by lithium metal, a chemical process which does not form a stable SEI layer. This reduction, thought to result in LiF, CH_3Li and ethane gas, continues till all the lithium metal is consumed.

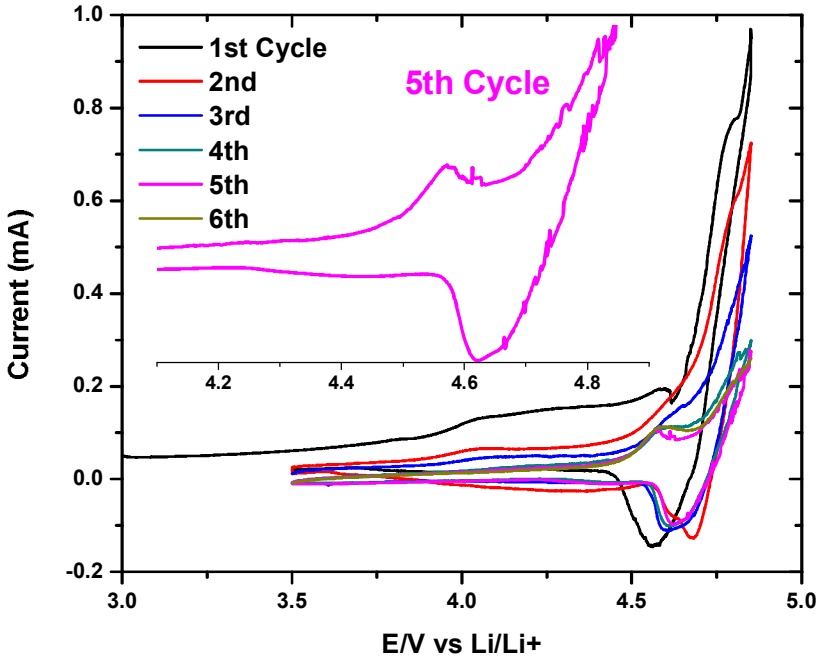

Figure 6.5: Cyclic voltammetry curves of a cell using an LMNO cathode and li-metal counter electrode at room temperature and a sweep rate of 0.1 $mV \cdot sec^{-1}$.

The half-cells described above all used Li-metal counter electrodes, which could explain the odd electrode behaviors and high impedance. Replacing the lithium metal counter electrode with an activated carbon electrode would enable the characterization of lithium-ion cathode materials. Further, the aluminum current collector was replaced with stainless steel 316 current collectors since it is known aluminum can be etched by the $TFSI^-$ anion [66].

Because the charge capacitance of the activated carbon electrode is much less than the charge capacity per gram of Li cathode materials, sizing of the electrodes was important. A symmetric activated carbon:activated carbon cell (essentially an EDLC

device) was constructed with the same electrolyte to be used for Li cathode testing, 0.1 M LiTFSI in fluoromethane. The cell was charged at 90 μA· g^{-1}, equating to a similar current rate that would be used on a lithium cathode material. The charge-discharge curves are shown in Fig. 6.6 and show a capacitance of about 70 F·g^{-1}. This is equivalent to about a 10 mV voltage swing on a 100 mg activated carbon electrode for a 1 mAh capacity cathode material. Therefore, we may use the activated carbon electrode to serve as a pseudo-reference electrode and assume the voltage changes very little during charge and discharge operation.

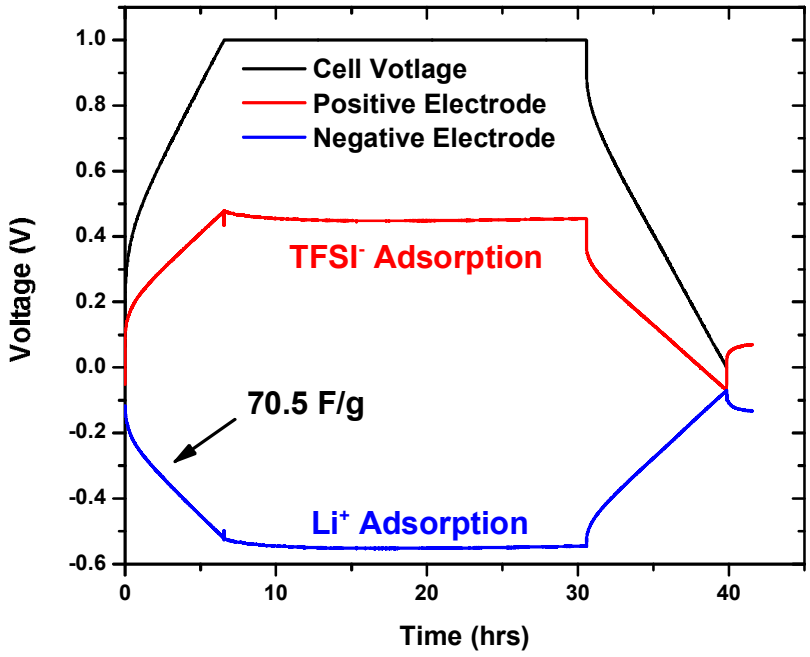

Figure 6.6: Charge-discharge curve of two activated carbon electrodes of 110 mg mass using 0.1 M LiTFSI in difluoromethane as electrolyte.

Replacing the lithium metal counter electrode with the activated carbon electrode

showed a significant decrease in cell impedance for both LCO and LMNO cathode half-cells, reducing the overall impedance of the electrodes to around 300 Ω, seen in Fig. 6.7 and only showing one semi-circle, indicating most of the impedance contribution only comes from one electrode, presumably from the lithium intercalation cathodes, in this case.

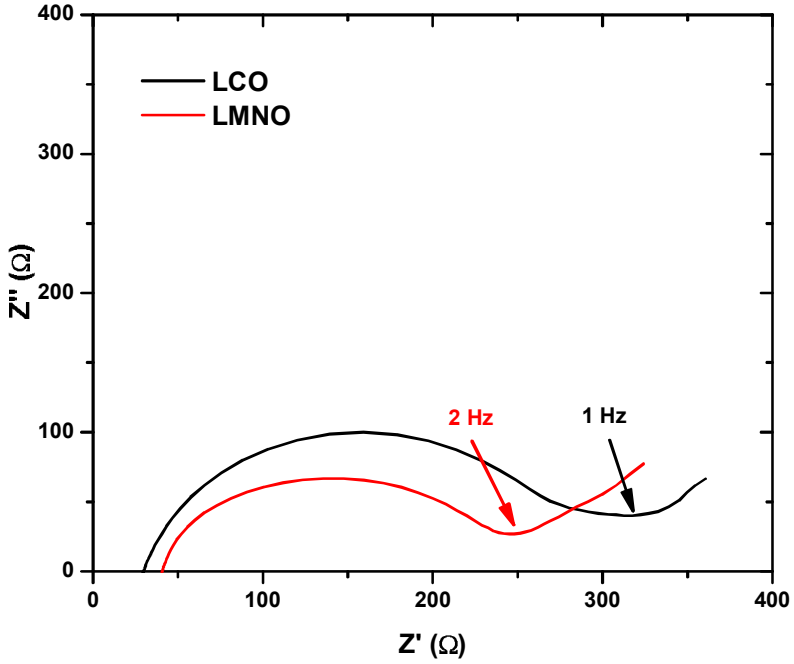

Figure 6.7: Nyquist plots of LMNO and LCO cells using activated carbon counter electrodes.

Cyclic voltammetry on LCO and LMNO cathodes were conducted, shown in Fig. 6.8, using activated carbon as the counter and reference electrode. For both electrodes, clear redox peaks are observed. The oxidation and reduction of Co^{3+}/Co^{4+} in LCO takes place around 1.4 V and 1.1 V vs AC, respectively. As these peaks generally occur

around 3.9 V and 3.6 V vs. Li, it is determined the activated carbon has a potential of around 2.5 V vs. Li. The LMNO electrode has oxidation peaks at 1.1 V and 1.8 V vs. AC, corresponding to the oxidation of Mn^{3+} and Ni^{2+}, respectively. The corresponding reduction peaks are found at 1.0 V and 1.7 V vs. AC. As these peaks generally occur around 4 V and 4.75 V vs. Li in conventional electrolytes, it is determined the potential of the activated carbon here to be about 3.0 V vs. Li. The discrepency may be due to an unknown iR drop or different preperation of the activated carbon electrodes.

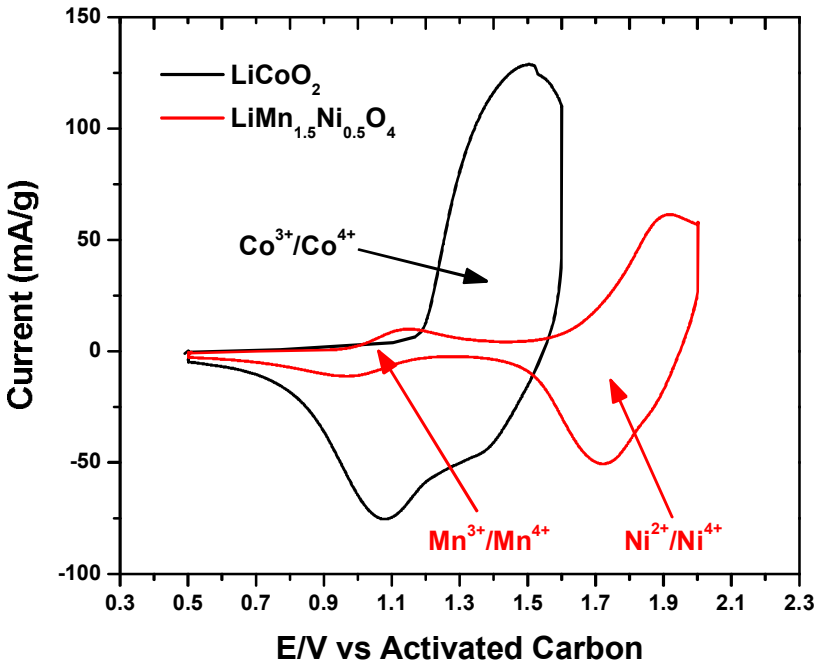

Figure 6.8: Cyclic voltammetry curves of LCO and LMNO cathode materials with a 0.1 $mV \cdot sec^{-1}$ sweep rate at room temperature with an electrolyte composed of 0.1 M LiTFSI in fluoromethane.

The magnitude of the LCO oxidation and reduction currents match well with the theoretical capacity of the electrode of 137 mAh/g. However, the total capacity of the

LMNO electrode seems to be far less than the theoretical capacity of 147 mAh/g. This is confirmed by constant charge-discharge curves shown in Fig. 6.9, conducted at C/2 rate. The charge-discharge of the LCO electrode, shown in Fig. 6.9a, took the expected 2 hours to charge and about 1.5 hours to discharge, giving an overall charge-discharge efficiency of about 75%. The charge-discharge of the LMNO electrode, shown in Fig. 6.9b, took 1 hour to charge and discharge at the C/2 rate. This shows an electrode capacity utilization of only about 50%, but an overall charge-discharge efficiency close to unity. While the 50% capacity utilization matches that from the cyclic voltammetry data in Fig. 6.8, it is thought these issues are due to poor mechanical assembly of the cells. Improved cell assembly with better electrode alignment and electrode pressure should improve these metrics.

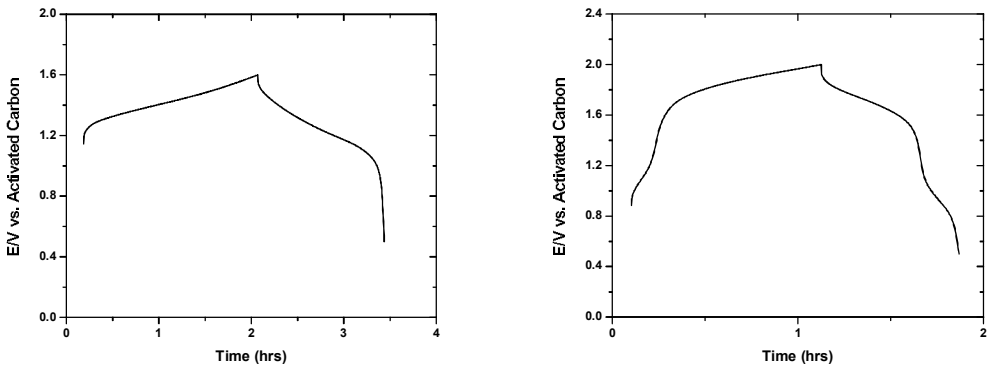

(a) (b)

Figure 6.9: Charge-discharge curves for an (a) LCO and (b) LMNO cathode at C/2 rate and room temperature.

With well behaving electrodes, the low temperature behavior was explored. The charge-discharge efficiency of LCO and LMNO cathodes in conventional electrolyte (1

M $LiPF_6$ in 1:1 EC:DMC) is shown in Fig. 6.10a. At a C/10 rate, the LCO and LMNO cathode show a charge-discharge efficiency of 57.9% and 26.2%, respectively. This is expected as this electrolyte tends to precipitate out and have a very low conductivity at these temperatures. The fluoromethane based electrolyte instead shows charge-discharge efficiencies significantly improved even at a higher C/2 rate. At -40 and -60 °C, the LCO electrode shows efficiencies of 93.8% and 69.8%, respectively. At -40 and -60 °C, the LMNO electrode shows efficiencies of 77.9% and 28.7%, respectively. The efficiencies for both cathodes are the best reported for these temperatures and meet the automotive requirement of 80% charge-discharge efficiency at -40 °C. Further, any discharge of these materials at -60 °C has never been reported, to the author's knowledge.

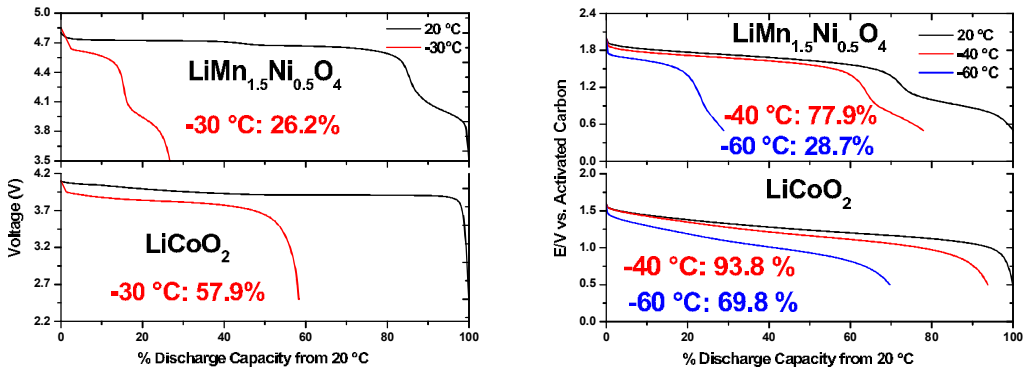

(a) (b)

Figure 6.10: Charge-discharge curves of LCO and LMNO electrodes at various temperatures using (a) conventional 1 M $LiPF_6$ in 1:1 EC:DMC electrolyte at C/10 rate and (b) 0.1 M LiTFSI in fluoromethane at C/2 rate.

The LCO and LMNO cells were cycle tested at C/2 rate at -60 °C, shown in Fig. 6.11. The LCO and LMNO cells showed a fairly constant charge-discharge efficiency

of 80% and 75%, respectively. The capacity retention for both electrodes both initially jump up about 10-30 % followed by a steady decline. The initial jump is likely due to mechanical construction of the cell and low compression pressure of the two electrodes against each other. The otherwise good cyclability of these electrodes demonstrate the possibility of using compressed gas solvent based electrolytes for lithion-ion batteries.

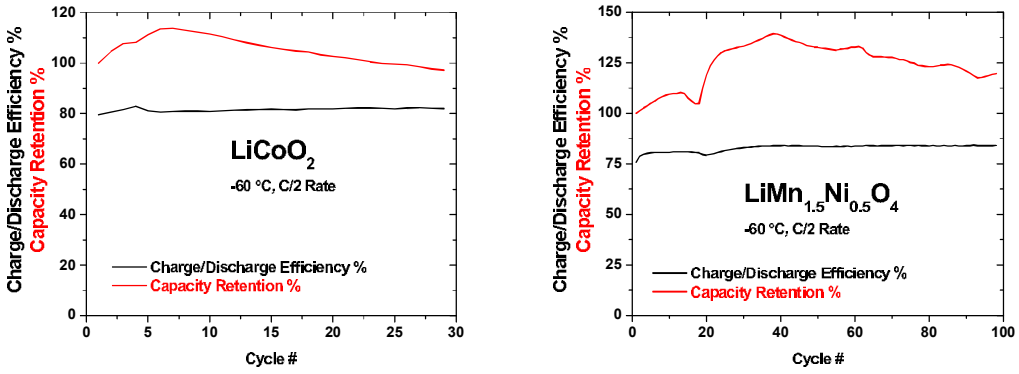

(a) (b)

Figure 6.11: Charge-discharge efficiency and capacity retention % of (a) LCO and (b) LMNO electrodes over cycling at C/2 rate at -60 °C.

6.4 Conclusion

The use of compressed gas solvent based electrolytes for lithium ion batteries offered a number of challenges including proper preparation of the electrolyte and selection of counter electrode material. However, with the correct preperation of cells, exceptional low temperature performance has been demonstrated, showing charge-discharge efficiencies at the C/2 rate of 93.8% and 69.8% at -40 and -60 °C, respectively, for an LCO

cathode and 77.9% and 28.7% at -40 and -60 °C, respectively, for an LMNO cathode. Efficiencies this high, at even moderate charge-discharge rates, has not previously been reported. Cycling of these electrodes also looks promising. However, capacity utilization and capacity fade are still a concern, which will probably be improved with better mechanical assembly of the cells. These results prove the ability for compressed gas solvent based electrolytes to operate with lithium-ion battery technology, offering possibilities such as low temperature performance and possibly high voltage cathode operation.

Chapter 7

Chemical Reduction of Fluorinated Compressed Gas Solvents with Lithium Metal

The chemical reduction of six fluorinated compressed gas solvents with lithium metal are explored and it is found each solvent is reduced quite differently. However, the reductions may be grouped into two categories; mono-fluorinated solvents that fully consume the lithium metal and poly-fluorinated solvents that form stable SEIs that prevent further solvent reduction.

7.1 Introduction

As discussed in Chapter 2, fluorinated compressed gas solvents show remarkable properties that may be useful for lithium-ion batteries and electrochemical double-layer capacitor devices. For lithium-ion batteries, it is interesting to explore the reduction of these solvents at lithium potential, particularly at a lithium metal surface. The chemical reduction route these solvents take may indicate what types of SEI layers are formed on real anode surfaces, if any.

7.2 Experimental

7.2.1 Methods

Lithium metal was scrapped clean with a glass slide, weighed and inserted into a glass vile, which was then plugged with a porous polypropylene mesh. Typically, about 20 mg of lithium metal was used. The glass vial and lithium contents was then inserted into a larger stainless steel 316 cell and sealed shut under argon atmosphere. Vacuum was then briefly pulled on the cell through a valve and subsequently cooled to ca. -60 °C. Solvent was then introduced into the cell in gaseous form by evaporation from a pressurized liquid state at room temperature, which was then condensed back to a liquid state inside the cooled cell. After solvent filling, the valve was again shut and allowed to warm to room temperature. The cell mass was measured before and after solvent filling to verify the cell was completely filled with liquid solvent. After allowing the lithium

metal and solvent reaction to proceed for a certain amount of time (typically 24 hours), the cell was opened and the reacted lithium contents were weighed. On occasion, thick glass bottle with a tight seal was used as the reaction vessel with the lower vapor pressure solvents in order to visually observe the reaction. In such cases, solvent was added into the lithium loaded glass bottle and solvent added under argon atmosphere.

Methyllithium, ethyllithium and isopropyllithium solutions were purchased and solid samples were collected by gentle evaporation of the solvent with use of a cold trap. No heating or further purification was performed.

7.2.2 Characterization

FT-IR measurements were performed with a Nicolet 6700 (Thermo Scientific) using transmission IR for powder samples and a single-bounce diamond ATR-IR (attenuated total reflectance) for solid lithium samples. Nujol mulls were prepared from powder samples by first grinding into a fine powder with a polished mortar and pestle, after which mineral oil was added drop wise and was further mixed till a nearly translucent paste was formed. A small amount of paste was then added between two polished potassium bromide crystals which were used for transmission IR measurements. Since solid lithium metal is highly sensitive to atmosphere, samples were submerged into mineral oil in an argon atmosphere and sealed in a glass vial. Immediately before measurements, the still oil coated sample was removed from the vial, placed on top of the ATR-IR diamond surface and clamped down with an additional thick piece of plastic. This method allowed for very minimal atmospheric exposure to the lithium metal samples and multiple scans

over several minutes showed no sign of atmospheric contamination. The light pressure applied from the clamped plastic on top of the lithium metal ensured a very thin layer of mineral oil between the sample and the ATR crystal. This thin layer allowed for good FT-IR signal from the metal surface since the penetration depth of ATR-IR is typically on the order of 1 μm.

For XRD measurements, powder and solid lithium samples were individually vacuum sealed in plastic bags under argon atmosphere. The sealed samples were then transferred to the XRD chamber (Bruker) for measurment. SEM and EDX measurements were made with a Phillips XL30 ESEM with an Oxford EDX attachment and were made by storing lithium samples under argon and quickly transferring to the SEM vacuum chamber with atmospheric exposure limited to about 10 seconds.

7.2.3 Chemicals

Lithium metal (0.38 mm thick), mineral oil (infrared spectroscopy grade), methyllithium (1.6 M in diethylether), ethyllithium (0.5 M in benzene:cyclohexanes 90:10) and isopropyllithium (0.7 M in pentane) were purchased from Sigma-Aldrich. Potassium bromide crystals (5 mm thick, 25 mm diameter) were purchased from International Crystal Laboratories. Difluoromethane (DFM, 99.9%), fluoroethane (FE, 97%), 1,1-difluoroethane (DFE, 99%), 1,1,1,2-tetrafluoroethane (TFE, 99%) and 2-fluoropropane (FP, 98%) were purchased from Synquest Laboratories. Fluoromethane (FM, 99.99%) was purchased from Airgas.

7.3 Results and Discussion

Each of the six fluorinated compressed gas solvents evaluated were uniquely chemically reduced by lithium metal. All mono-fluorinated (FM, FE, FP) solvents chemically reacted and consumed lithium metal and turned the entire metal sample into powder. All poly-fluorinated solvents (DFM, DFE, TFE) left the Li metal intact, and in some cases, formed a thin solid layer on its surface. Table 7.1 summarizes the resulting reaction products resulting from chemical reduction of these fluorinated solvents with lithium metal and Fig. 7.1 shows optical images of the products after the reaction has completed.

Figure 7.1: Optical images of reaction products resulting from chemical reduction of fluorinated solvents with lithium metal.

7.3.1 Fluoromethane

Chemical reduction of fluoromethane with lithium metal was a very slow reaction process, but the final reaction product resulted in a brownish-purple powder form. The reaction was studied in detail with a number of cells reacting in parallel, each which was stopped after a different amount of time. Optical photos of reaction products after 1, 15 and 25 days is shown in Fig. 7.2. The images show initially a gray/brown surface layer

Table 7.1: Summary of products resulting from chemical reduction of solvents with lithium metal.

Solvent	Reaction Product	Approximate Reaction Speed	Product Color	% Change in Mass
FM	Powder	20 days	Brown Purple	265
DFM	Solid	None	No Change Silver	0
FE	Powder	2 hrs	White Purple Black	440
1,1-DFE	Solid	5 min	Gray Black	20
1,1,1,2-TFE	Solid	1 hr	Gray	5
2-FP	Powder	3 hrs	Purple Black White	285

of approximately 5 μm on the Li metal after 1 day. This thin surface layer, even after 1 day of reaction, is noticeably hard and brittle. The fluoromethane solvent continues to react despite this surface layer and after 15 days has grown a very thick light brown surface layer many hundreds of microns thick. Further reaction to 25 days leaves the entire lithium metal in a brown-purple powder form.

SEM images shown in Fig. 7.3 show lithium metal after reaction with fluo-

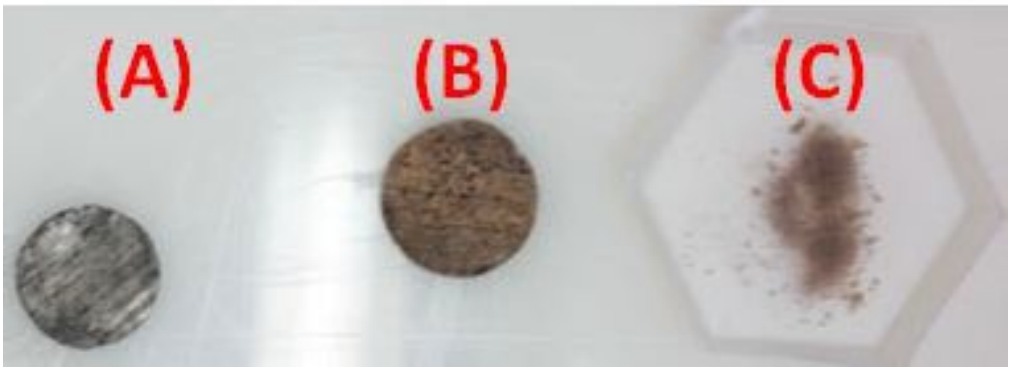

Figure 7.2: Product of chemical reduction of fluoromethane solvent with lithium metal at (a) 1 day, (b) 15 days and (c) 25 days.

romethane after 5 days. Fig. 7.3a shows a very fractured surface over the entire lithium metal surface. Fig. 7.3b and Fig. 7.3c show higher magnified images of a cross section of the surface features, showing large pieces of material of approximately 40 μm that have formed from the lithium surface. EDX was performed to determine the elemental composition of the formed surface, Fig. 7.4, which shows that the primary detectable element of the surface was fluorine, however, is not sensitive to lighter elements such as carbon, lithium and hydrogen, but are presumed to be present.

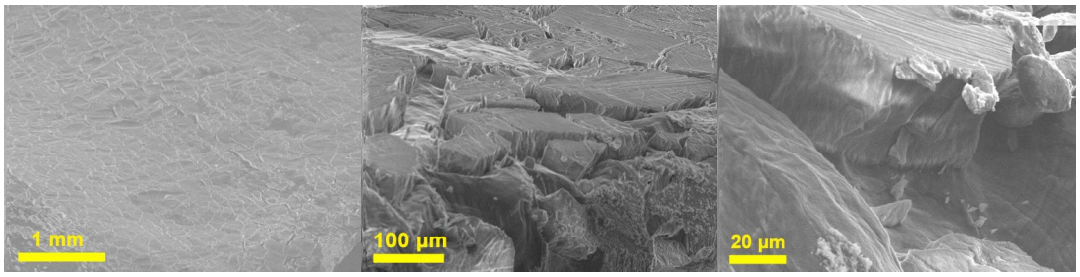

(a) (b) (c)

Figure 7.3: SEM images of the resulting lithium metal surface after reaction with fluoromethane after 5 days.

Possible scenarios for the chemical reduction of fluoromethane is shown in Fig.

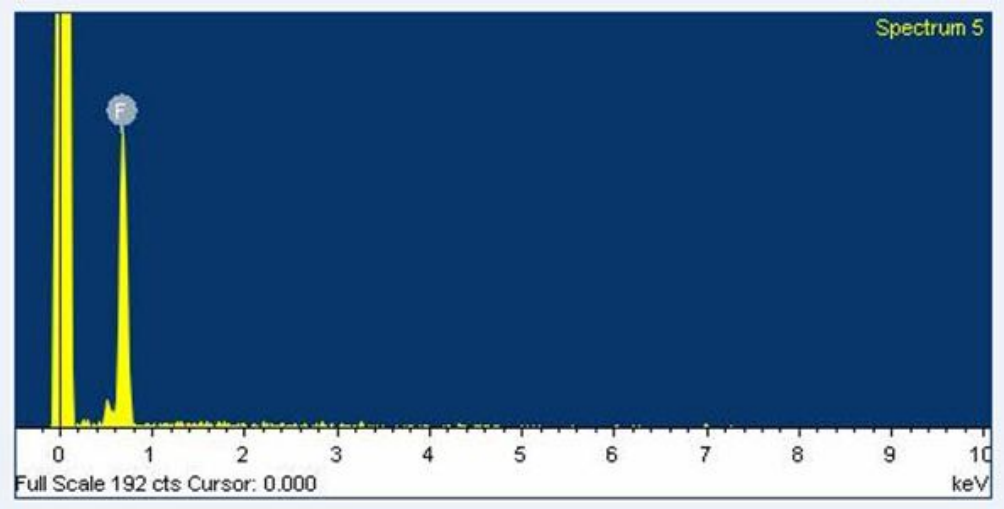

Figure 7.4: EDX analysis of the surface of lithium metal after reaction with fluoromethane for 5 days.

7.5. The initial reaction likely starts with reduction of the highly electronegative fluorine atom, forming LiF and a methyl radical. As LiF is insoluble in fluoromethane, it remains on the surface as a solid. The methyl radical may proceed to react with lithium metal to form methyl lithium or combine with another methyl radical to form ethane gas.

To verify that LiF was formed as a product of the reaction, XRD was performed on samples after 1, 15, and 25 days of reaction, results shown in Fig. 7.7. There is a very clear increase in LiF product with longer reaction time, as shown by increasing LiF peaks at 38.4°, 44.5°and 65.0°. There seems to be a large amount of LiF produced between 1 and 15 days, with less being produced between 15 and 25 days. The reasoning for this is likely that by 15 days, most of the reaction has already taken place, and by 25 days the reaction is complete. No other obvious peaks were detected other than those expected from the vacuum bag which shows any other solid products of the reaction were not well crystalized. To verify methyl lithium was formed as a product of the reaction, FTIR was

performed after 25 days of reaction with the powder sample reaction product, results shown in Fig. 7.8. There was a very clear peak at 2770 cm^{-1} which corresponds well to the methyl lithium FTIR peak. Other strong methyllithium peaks at 2698 and 2610 cm^{-1}, however, were not visible in the reacted product. Other peaks are thought to be due to impurities in the methyllithium solid that was not purified. Peaks at 1113, 1057 and 887 cm^{-1} are not very clear since they coincide with lithium metal peaks. Though it is thought there is no metallic lithium left in the reacted product, strong Li-Li bonding may still occur between both methyllithium and LiF products making analysis of these peaks difficult.

If the reaction scheme proposed in Fig. 7.5 is correct, one may calculate the approximate ratio of methyllithium to ethane gas product generation from the reaction from the % mass change, shown in Table 7.1 to be 265% for reduction of fluoromethane with lithium metal, assuming this mass only includes contributions from LiF and methyllithium. From this, we may estimate that the ratio of the secondary reactions (A):(B) in Fig. 7.5, resulting in ethane gas and methyllithium production, respectively, is approximately 4:1. This makes sense since the access of the methyl radicals may be partially blocked to the lithium surface by LiF and other methyllithium molecules, making ethane gas production the more likely reaction route. This also explains the slow reaction rate of the reduction of fluoromethane with lithium metal since if diffusion of a methyl radical to the lithium surface is slow, it is expected diffusion of a slightly larger fluoromethane molecule to the lithium surface is slow as well. It is very interesting to note the vapor pressures of ethane and fluoromethane are very similar, with ethane about 50 psi higher

than fluoromethane at room temperature, as shown in Fig. 7.9. This coincidence of vapor pressures could further explain the reaction rate of fluoromethane with lithium metal. As LiF and methyl lithium form a surface layer, ethane is continuously produced, cracking this surface layer and exposing fresh lithium metal and allowing further reduction of fluoromethane solvent. If ethane had a higher vapor pressure, ethane bubbling may have been more vigorous and cracking of the lithium surface more severe, accelerating the reaction rate. Had ethane gas have had a slightly lower vapor pressure or fluoromethane slightly higher, a stable surface layer may be formed and further solvent reduction may cease.

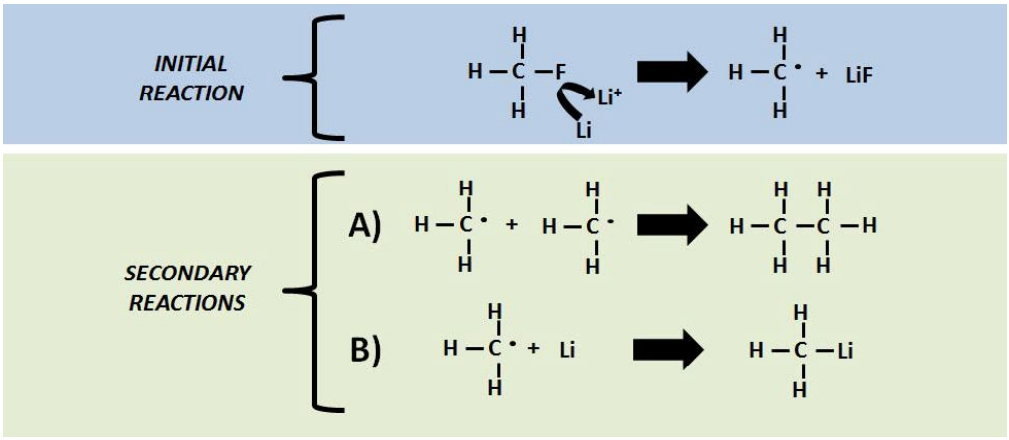

Figure 7.5: Possible scenarios for fluoromethane solvent reduction with lithium.

A stable surface layer that prevents further reduction of fluoromethane with lithium metal would be very useful. To determine if ethane production is truly the cause for an accelerated reduction of fluoromethane, one cell was identically prepared with lithium metal and liquid fluoromethane. Soon after the fluoromethane solvent was filled into the cell, an additional 1200 psi of pressure was applied from an argon gas cylinder,

then the cell was sealed. The reaction was allowed to proceed under the additional pressure for 21 days. A change in mass of 260% was found, and was nearly identical to the previous 25 day experiment showing 265%. However, the lithium metal under pressure was found to be mostly intact rather than powderized, Fig. 7.7, as was found with the other reaction without the additional pressure. It is hypothesized that under the additional pressure, ethane is still generated in liquid phase and, since the volume of liquid ethane is substantially less than the gaseous phase, allows the methyllithium to grow a tighter structure allowing the lithium structure to stay intact. However, no such stable surface layer is grown preventing the further reduction of difluoromethane at lithium metal.

7.3.2 Fluoroethane

Chemical reduction of fluoroethane with lithium metal was relatively quick reaction, turning the lithium metal into a white, purple and black powder within about 2 hours. Similar to the reaction scheme described for fluoromethane, it appears the reaction begins with chemical reduction of the fluorine to create LiF and an ethyl radical, as seen in Fig. 7.10. Similar to fluoromethane, the ethyl radical can either combine with another ethyl radical to form butane, reaction path (A), or react with lithium metal to form ethyllithium, reaction path (B). Unlike the methyl radical formed from the reduction of fluoromethane, the ethyl radical may also decompose into ethylene and hydrogen, reaction path (C). The hydrogen produced from reaction path (C) may combine with hydrogen or lithium to form H_2 or LiH.

Figure 7.6: Optical photo of lithium metal after 21 days of reaction with fluoromethane under an applied 1200 psi of pressure.

It was observed that during the chemical reduction of fluoroethane with lithium metal, vigorous bubbling had occurred. High vapor pressure components produced during the reaction are shown in Fig. 7.11. It is seen that butane and ethylene have significantly lower and higher vapor pressures, respectively, than fluoroethane across all temperatures. Hydrogen gas is not shown, but has a significantly higher vapor pressure as well. Because there was vigorous bubbling observed during the reaction, it is expected ethylene and hydrogen is produced, and likely H_2 and LiH as well. Because the diffusion kinetics of the ethyl radical is likely much slower than the decomposition of the highly

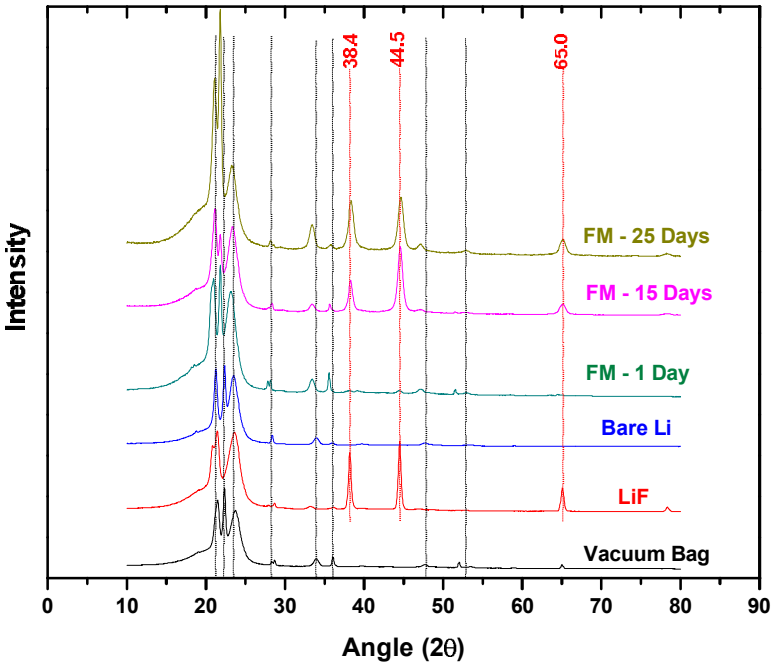

Figure 7.7: XRD analysis of reaction products from fluoromethane reduction with lithium metal.

unstable ethyl radical to ethylene and hydrogen, it is expected butane and ethyllithium generation is minimal.

To verify that LiF was formed as a product of the reaction, XRD was performed on powder samples, shown in Fig. 7.12. Similar to the previously descirbed specra of fluoromethane reduction, the XRD spectra show LiF peaks at 38.4°, 44.5°and 65.0°. FTIR was also performed to determine what other products were formed, shown in Fig. 7.13. The FTIR spectra does not show a strong correlation of peaks of ethyllithium with the resulting powder product. There are, however, peaks at 2746 and 944 cm^{-1} which are likely due to ethyllithium, but are shifted to due to other components generated from

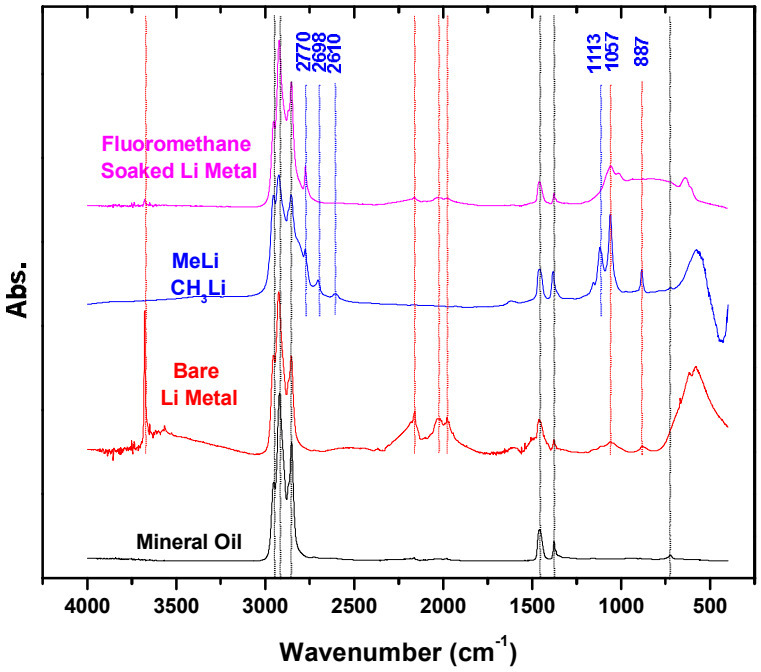

Figure 7.8: FTIR analysis of reaction products from fluoromethane reduction with lithium metal.

the reaction. Further, various peaks in the ethyllithium spectra could be due to impurities in the unpurified material.

7.3.3 2-Fluoropropane

Chemical reduction of 2-fluoropropane with lithium metal, like fluoroethane, is a relatively quick reaction, turning the lithium metal into a purple, black and white powder within about 3 hours. Similar to the reaction schemes described in Fig. 7.5 and Fig. 7.10, it appears the reaction begins with chemical reduction of the fluorine to create LiF and an isopropyl radical, as seen in Fig. 7.14. Similar to fluoroethane, the isopropyl

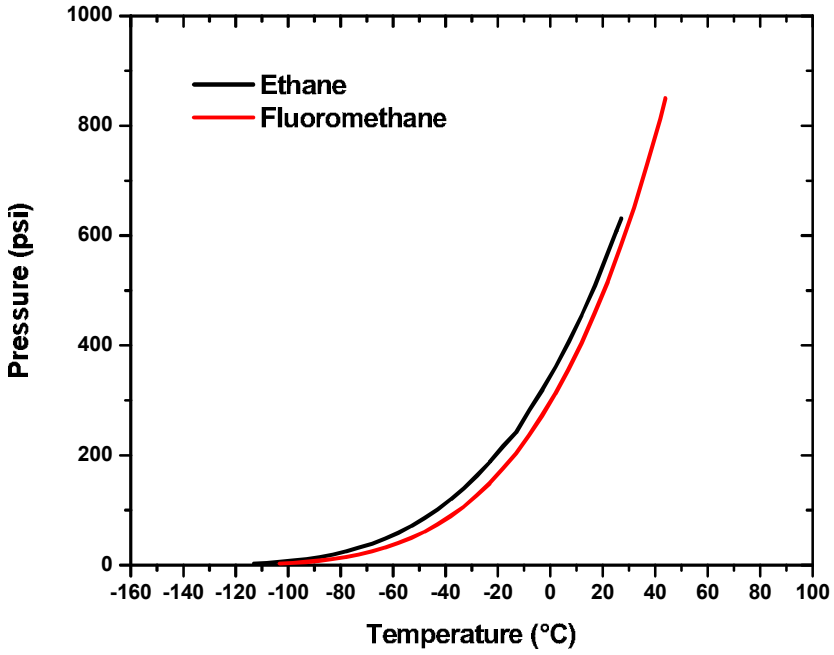

Figure 7.9: Vapor pressures for ethane and fluoromethane gas as a function of temperature.

radical may take one of three routes; combine with another isopropyl radical to form 2,3-dimethylbutane, reaction path (A), decompose into propadiene and three hydrogens, reaction path (B), or combine with lithium to form isopropyllithium. The hydrogen produced from reaction path (C) may combine with hydrogen or lithium to form H_2 or LiH.

It was observed that during the chemical reduction of 2-fluoropropane with lithium metal, vigorous bubbling had occurred. Since 2,3-dimethylbutane is a liquid at room temperature, it shows that reaction path (C), formation of propadiene and hydrogen must occur since their vapor pressures are greater than 2-fluoropropane (107 psi vs 37

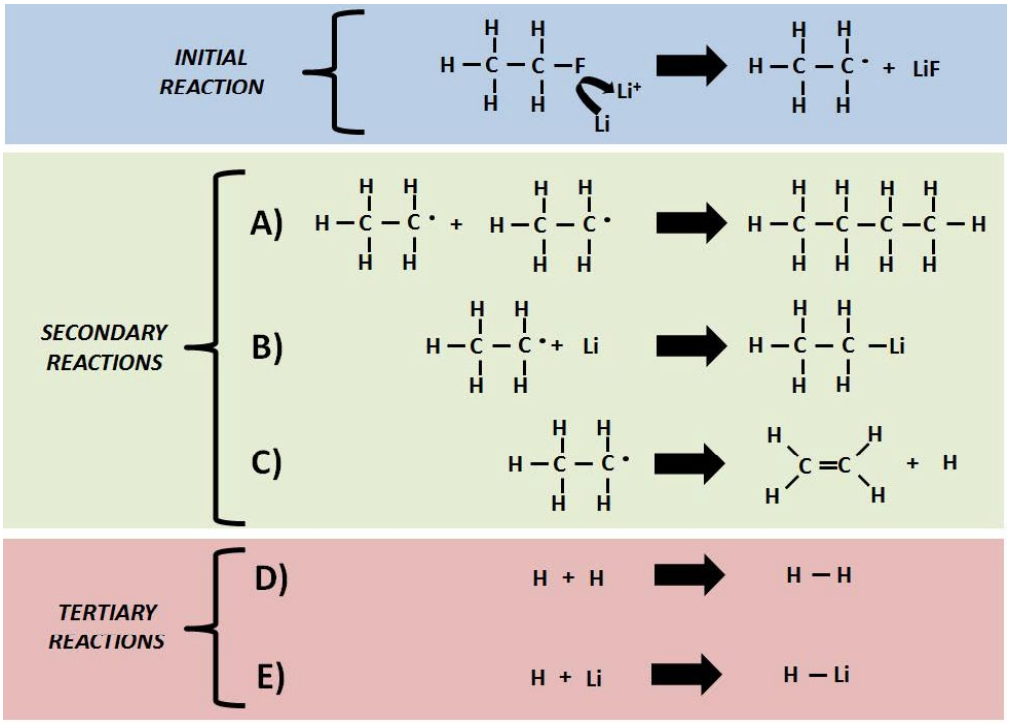

Figure 7.10: Possible scenarios for fluoroethane solvent reduction with lithium metal.

psi). Because the diffusion kinetics of the isopropyl radical is expected to be much slower than the decomposition of the radical to propadiene and hydrogen, it is expected that a majority of reactant product will be white LiF and black LiH. However, there is a strong purple color to the product, perhaps from another reaction not considered here.

To verify that LiF was formed as a product of the reaction, XRD was performed on powder samples, shown in 7.15. Similar to the previously descirbed specra of fluoromethane and fluoroethane reduction, the XRD spectra show LiF peaks at 38.4°, 44.5°and 65.0°. No other peaks are seen, probably because of the lack of crystallinity in the reactant products. FTIR was also performed to determine what other products were formed, shown in Fig. 7.16. The FTIR spectra does not show a strong correlation of

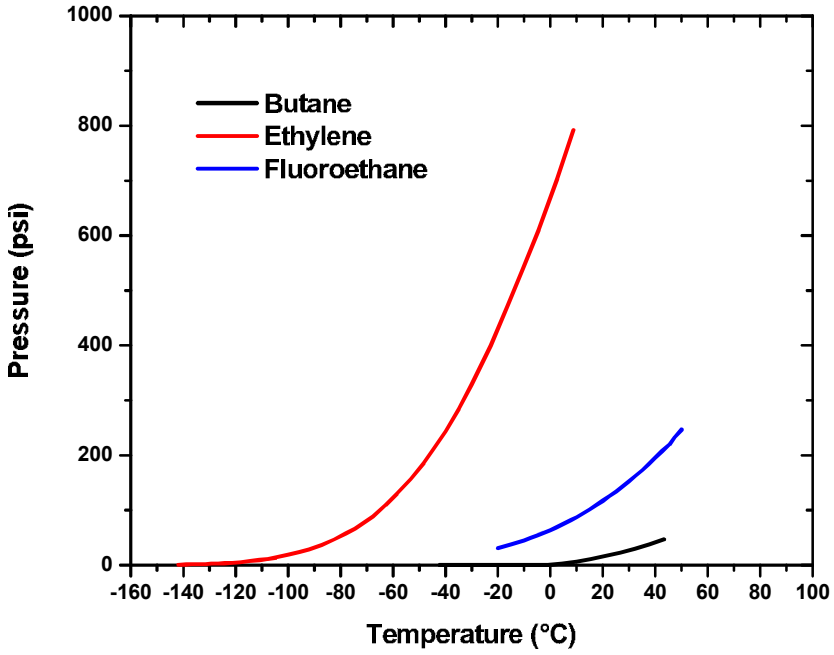

Figure 7.11: Vapor pressures for butane, ethylene and fluoroethane gas as a function of temperature.

peaks of 2-propyllithium with the resulting powder product. This shows 2-propyllithium is not a primary component of the reaction products.

7.3.4 Difluoromethane, 1,1-Difluoroethane, 1,1,1,2-Tetrafluoroethane

Soaking lithium metal in difluoromethane, 1,1-difluoroethane, 1,1,1,2tetrafluoroethane all resulted solid lithium metal products with various surfaces. XRD and FTIR specra for the resulting products are shown in Fig. 7.17 and Fig. 7.18, respectively.

No new peaks appear in either XRD and FTIR spectra for lithium metal soaked in

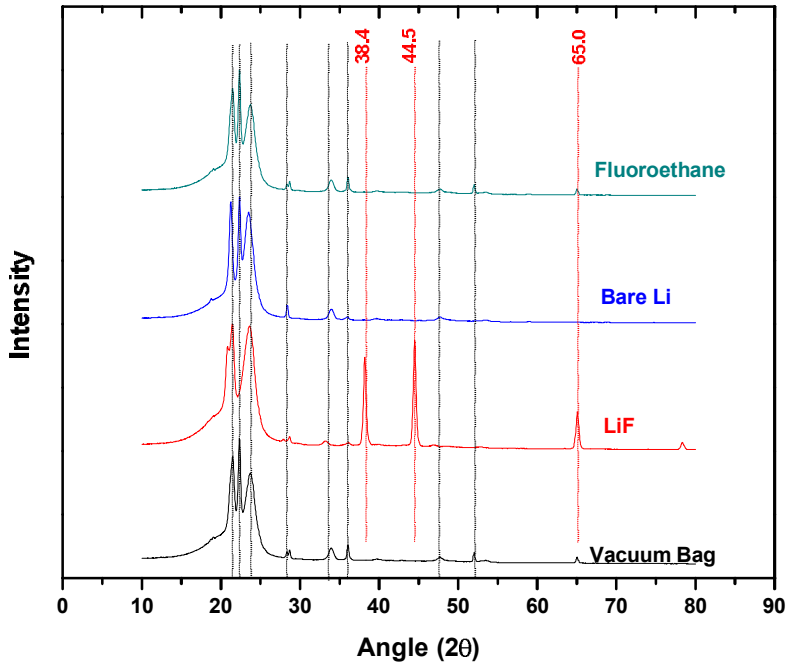

Figure 7.12: XRD analysis of reaction products from fluoroethane reduction with lithium metal.

difluoromethane solvent. Further, visual inspection, shown in Fig. 7.1, shows no change to the lithium metal surface and there is no change in mass detected. However, SEM inspection of the lithium metal surface, shown in Fig. 7.19, does show some very slight surface features, perhaps a thin polymerization layer. It is not clear, however, if this is simply due to the rough lithium metal surface or actually indeed due to reduction with lithium metal. It is known multiple fluorine atoms on the same methyl group strengthen each of the C-F bonds [28], resulting in a highly stable molecule. Thus, it would not be surprising to find that difluoromethane is indeed not reduced at lithium metal potentials.

Reduction of 1,1-difluoromethane with lithium metal resulted in a rapidly formed

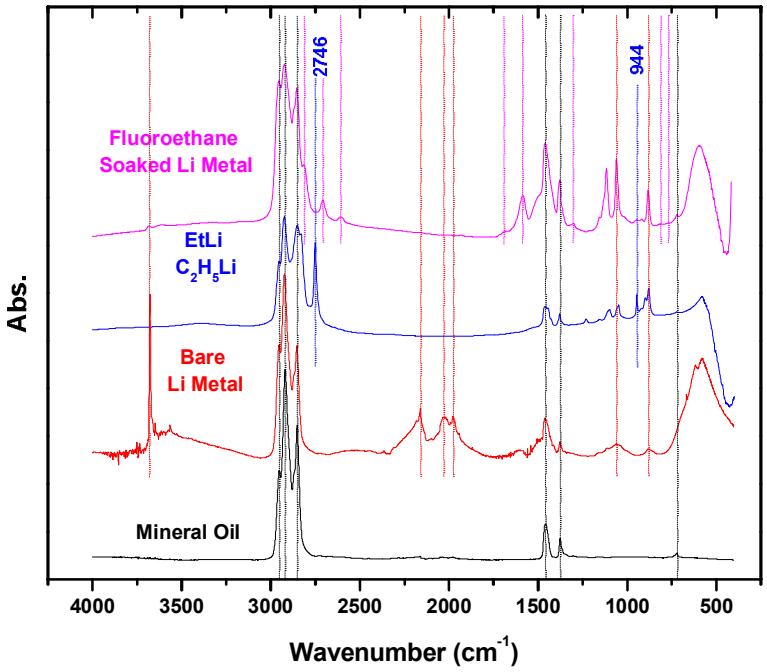

Figure 7.13: FTIR analysis of reaction products from fluoroethane reduction with lithium metal.

black layer on the lithium metal surface within about 5 minutes, after which it seems the reaction ceases to continue. The black surface seems to be a thick and dense enough layer preventing further reduction of 1,1-difluoroethane. The total change in mass was about 20% but would vary with various surface areas of lithium metal reactant. It is observed from the XRD spectra in Fig. 7.17 that there is indeed LiF formation involved in the reduction of the 1,1-difluoroethane, as expected. No other peaks are observed in the XRD spectra. FTIR spectra shown in Fig. 7.18 show no strong change in peaks other than a very broad peak and increase in absorption at wavenumbers great than 3000 cm^{-1}. This absorption of high wave numbers corresponds well with the black color of the lithium

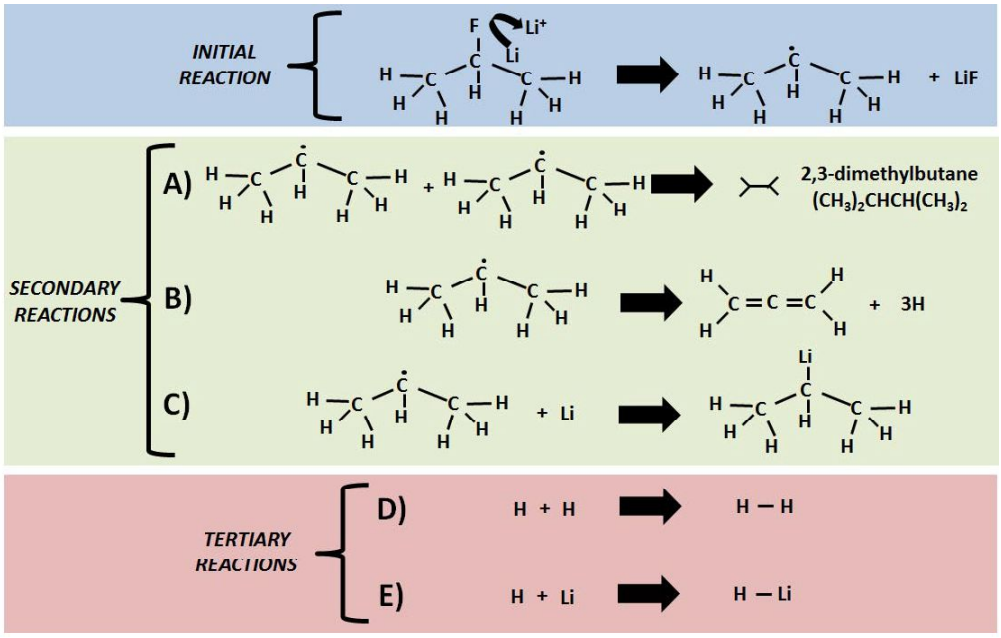

Figure 7.14: Possible scenarios for fluoroethane solvent reduction with lithium metal.

metal surface. SEM images, shown in Fig. 7.20 show a very roughened surface at high magnification, which appears to be a dense polymer layer formed by reduction of the solvent. The exact nature of the polymer was not determined, but is certainly a type of fluorohydrocarbon polymer.

Reduction of 1,1,1,2-tetrafluoromethane with lithium metal resulted in a strong dark gray color on the surface of the lithium metal within about 3 hours. As with 1,1-difluoroethane, once the surface was formed, the reaction seemed to stop, evidently because the surface layer was dense enough to prevent further solvent from reacting with the base lithium metal. The total change in mass of the lithium material was about 5%, pointing to a very thin surface layer. XRD spectra in Fig. 7.17 show formation of LiF, as expected. No other obvious peaks in the XRD are seen. FTIR spectra in Fig. 7.18 shows

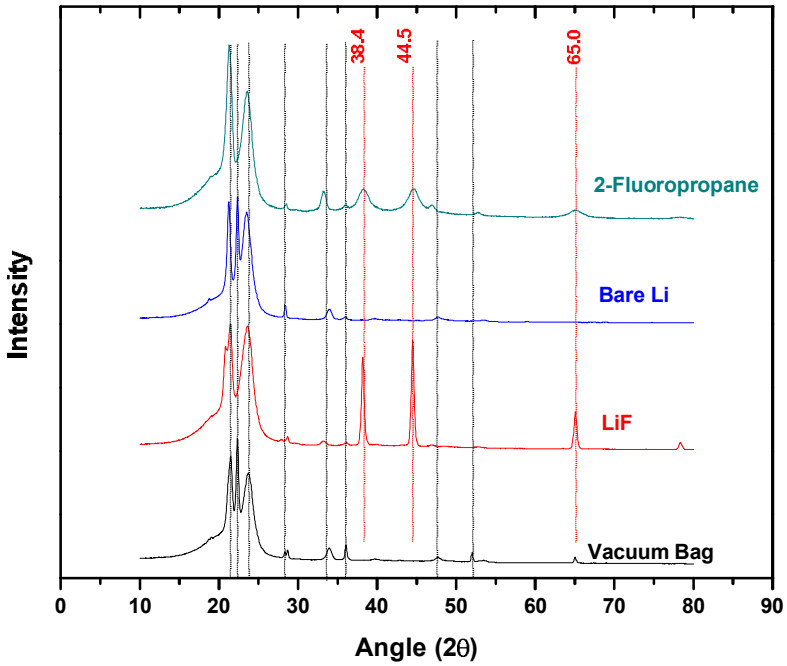

Figure 7.15: XRD analysis of reaction products from 2-fluoropropane reduction with lithium metal.

only one unknown new peak at 1219 cm^{-1}. SEM images, shown in Fig. 7.21 show a highly roughened surface, likely from very strong polymerization on the surface of the lithium metal. The origin of the change in the FTIR spectra and the polymerization layer has not been determined, but is expected to be a type of fluorohydrocarbon polymer.

7.4 Conclusion

The chemical reduction with lithium metal of six fluorinated compressed gas solvents (fluoromethane, fluoroethane, 2-fluoropropane, 1,1-difluoroethane and 1,1,1,2-tetrafluoroethane) has been studied. It has been shown that the monofluorinated solvents

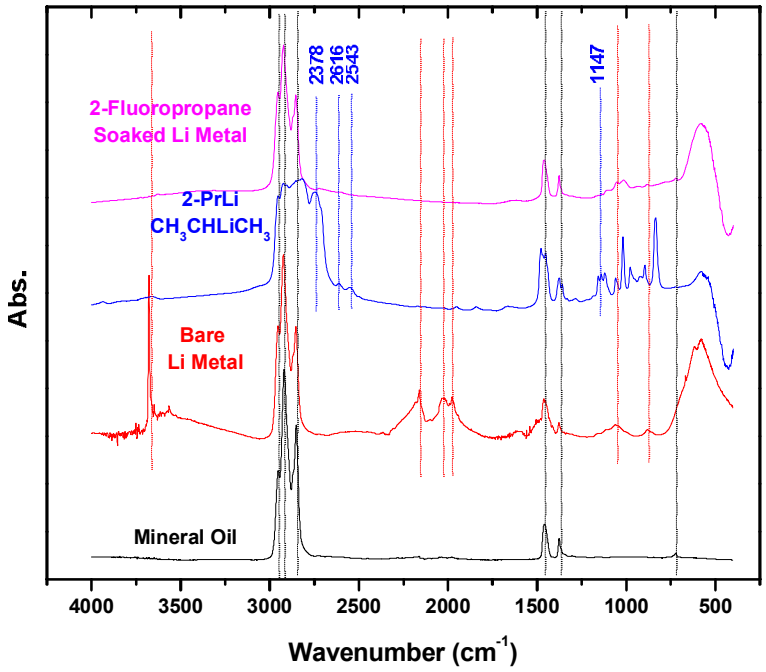

Figure 7.16: FTIR analysis of reaction products from 2-fluoropropane reduction with lithium metal.

(fluoromethane, fluoroethane and 2-fluoropropane) all react strongly with lithium metal, consuming all metallic lithium and turning it into powder form. The high vapor pressure hydrocarbon products of these reactions accelerate the reaction further by gassing and cracking the solid LiF and alkyllithium surface layer formed, exposing fresh lithium metal which the solvent may further be reduced by. Polyfluorinated solvents 1,1-difluoroethane and 1,1,1,2-tetrafluoroethane seem to be reduced with lithium metal and quickly form a stable LiF and fluorohydrocarbon polymerized surface layer which stops further solvent chemical reduction. The chemical reduction of difluoromethane with lithium metal is not clear, and it is believed that the solvent is not reduced at lithium metal potentials.

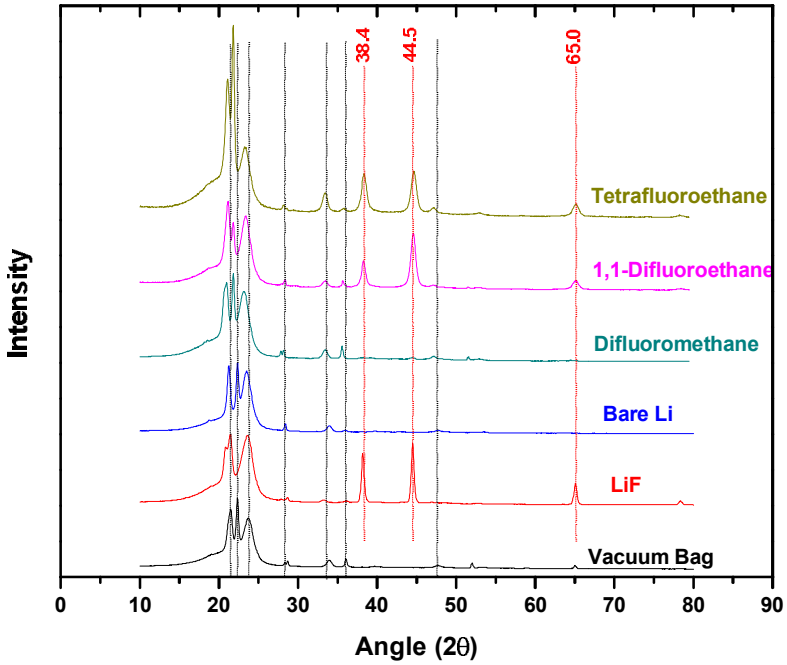

Figure 7.17: XRD analysis of reaction products from difluoromethane, 1,1-difluoroethane and 1,1,1,2-tetrafluoroethane reduction with lithium metal.

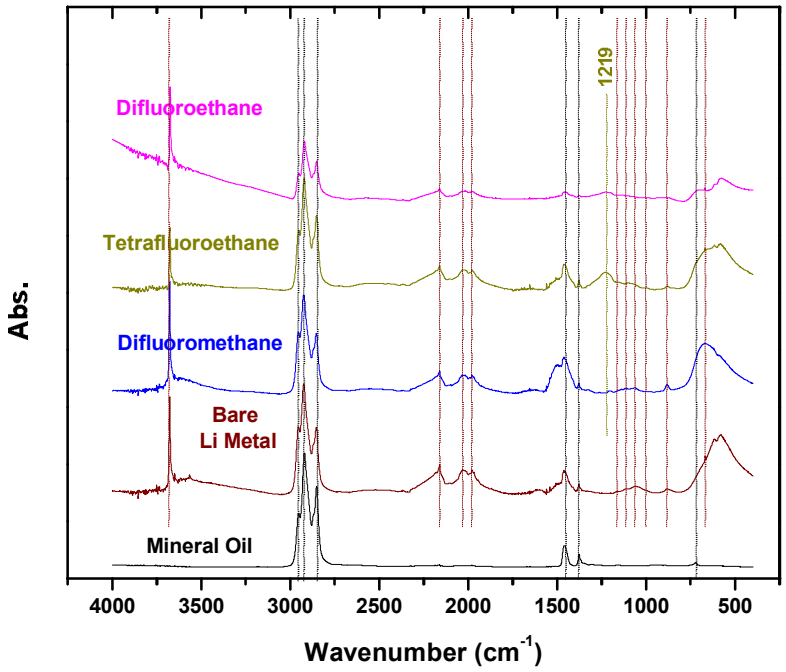

Figure 7.18: FTIR analysis of reaction products from difluoromethane, 1,1-difluoroethane and 1,1,1,2-detrafluoroethane reduction with lithium metal.

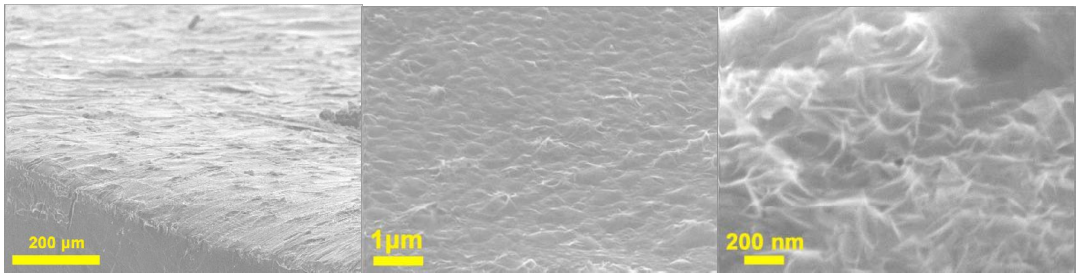

(a) (b) (c)

Figure 7.19: SEM images of the resulting lithium metal surface after reaction with difluoromethane after 1 day.

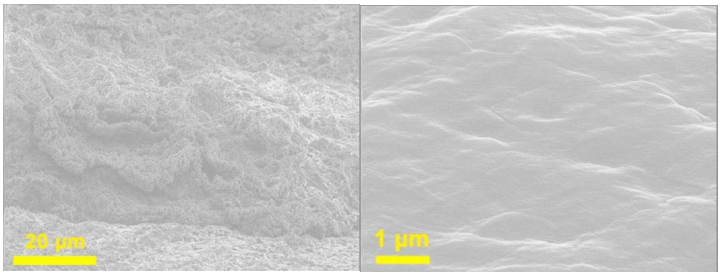

(a) (b)

Figure 7.20: SEM images of the resulting lithium metal surface after reaction with 1,1-difluoroethane after 1 day.

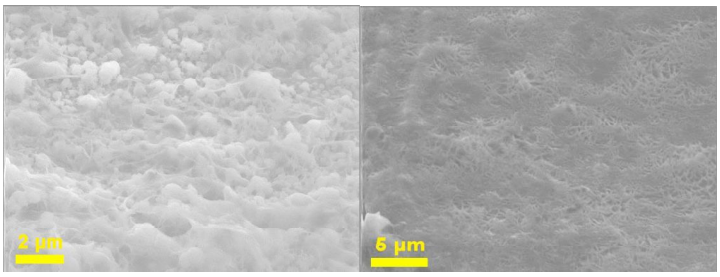

(a) (b)

Figure 7.21: SEM images of the resulting lithium metal surface after reaction with 1,1,1,2-tetrafluoroethane after 1 day.

Chapter 8

Thin-Film Electrode Array for Rapid Analysis of Li-Ion Battery Electrodes and Electrolytes

A thin-film array of electrodes composed of Li-ion battery cathode and current collector materials is fabricated for rapid analysis of battery electrolytes. Thin-films of battery cathode materials $LiCoO_2$, $LiMn_{1.5}Ni_{0.5}O_4$, and $LiNiPO_4$ are deposited via sputter deposition and characterized by raman spectroscopy. Different O_2% during sputter and anneal temperatures were used to optimize the electrode crystallinity and structure. Finally, electrolyte testing using this test electrode is demonstrated.

8.1 Introduction

Thin-film batteries are being explored for many applications [67–70] such as credit cards and microelectronics. However, they also have very ideal electrochemical behavior and allow fast analysis by cyclic voltammetry due to their low impedance. This makes them ideal for testing electrolyte behavior for intercalation, SEI formation, oxidation stability and full potential window analysis. Here, a thin-film rapid-test electrode is fabricated using thin-films of $LiCoO_2$, $LiMn_{1.5}Ni_{0.5}O_4$, and $LiNiPO_4$ for cathode evaluation and aluminum, copper and platinum for current collector and potential window evaluation. On-chip lithium metal reference and counter electrodes are also utilized. The raman spectra of the thin-film cathodes are thouroughly investigated with various annealing temperatures and O_2 sputter contents.

8.2 Experimental

8.2.1 Wafer Fabrication

Electrodes were fabircated on 99.6% alumina 3" square x .020" wafers, purchased from Valley Design Corp., which were polished on both sides to a 1-2μm" R_a surface roughness. Multiple patterning, sputter deposition and annealing steps were performed to fabricate the final wafer. A typical single deposition step was done by initially cleaning the alumina substrate by successive sonication in acetone, isopropanol, and ethanol, dried under a stream of nitrogen gas and heated to 150 °C on a hot plate to dehydrate the surface,

followed by an O_2 plasma clean for 2 minutes at 200 W power and 200 mT pressure (Technics PEIIB Planar Etcher). Photoresist (Futurrex NR9 6000) was then applied to the wafer via spin coating and the electrode pattern was then transferred via photolithography (Karl Suss MA6 Mask Aligner) followed by thin-film sputter deposition. A titanium adhesion layer was first deposited, followed by a titanium nitride blocking layer, to block titanium diffusion into subsequently deposited films during anneal. A platinum layer was then deposited on top of the titanium nitride layer to act as the base film for all further film deposition steps. After the primary top film was deposited, an Al_2O_3 passivation layer was deposited, as shown in Fig. 8.1. Titanium, copper, aluminum, platinum and alumina thin films were deposited under argon atmosphere with a base pressure of 5 μT (Denton Discovery 18). Titanium nitride thin-films were similiarly deposited by reactive sputtering in a 1:1 Ar:N_2 atmosphere. Lithium sputter targets $LiCoO_2$, $LiMn_{1.5}Ni_{0.5}O_4$, and $LiNiPO_4$ were all purchased from Plasmaterials and contained an extra 10 wt% Li_2O to compensate for any lithium loss during sputtering and annealing. Lithium targets were sputtered in a custom built sputter deposition vacuum chamber with a typical base pressure of 40 μT using various mixtures of oxygen and argon gas. After lithium-cathode film deposition, samples were annealed in a tube furnace with oxygen gas with 5 °C ramp rate, held at various temperatures for 2 hours, and allowed to cool back down to room temperature. Deposition of copper, aluminum and platinum electrodes and an alumina passivation layer then followed with post deposition annealing at 200 °C under vacuum for 2 hours. Film thicknesses measurements (Veeco Dektak 150) were an average of three data points over a wide area.

8.2.2 Electrode Materials and Geometry

The thin-film electrode was fabricated in order to do a rapid analysis of multiple Li-ion battery components in electrolyte systems that might be limited in electrolyte volume due to difficulty of synthesis or high cost. A schematic of the electrode is shown in Fig. 8.2. Three lithium intercalation materials, $LiCoO_2$, $LiMn_{1.5}Ni_{0.5}O_4$, and $LiNiPO_4$, were selected as primary test working electrode materials due to the range of charge potentials (4.1, 4.85, 5.2 V vs. Li, respectively) and different crystal structures (layered, spinel and phosphate, respectively). Copper and aluminum working electrodes were also selected to study any corrosion that might occur to common current collector materials as a result of the electrolytes studied. A sixth platinum working electrode was also selected to examine the potential windows and cyclic voltammetry curves of the electrolytes studied. All six working electrodes had an area of 1 mm^2, defined by a Al_2O_3 passivation layer. Larger counter and reference platinum electrodes were also fabricated which lithium was electrodeposited onto from a 0.5 M $LiClO_4$ in PC:THF 1:1 solution. Another benefit to the fabricated electrodes is the lithium plated counter and reference electrodes make for very convenient electrodes with which to measure the lithium cation transference number in the electrolyte, an important quantity rarely considered in electrolytic conductivity measurements.

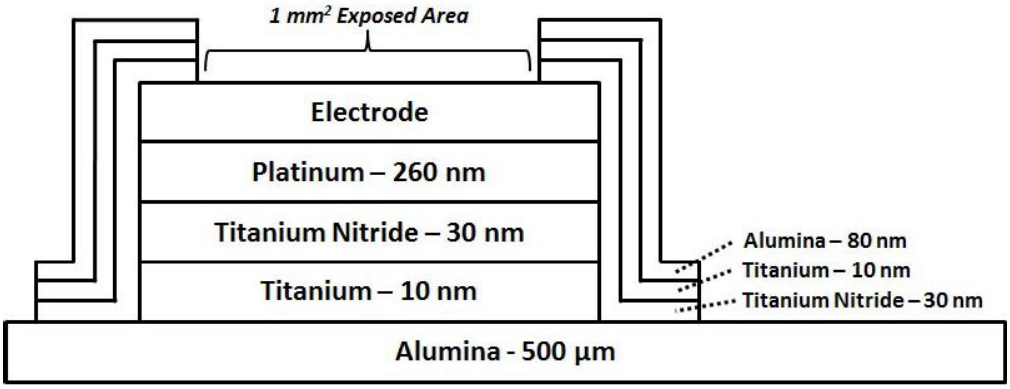

Figure 8.1: Geometrical schematic of thin-film layer stack up of fabricated electrodes.

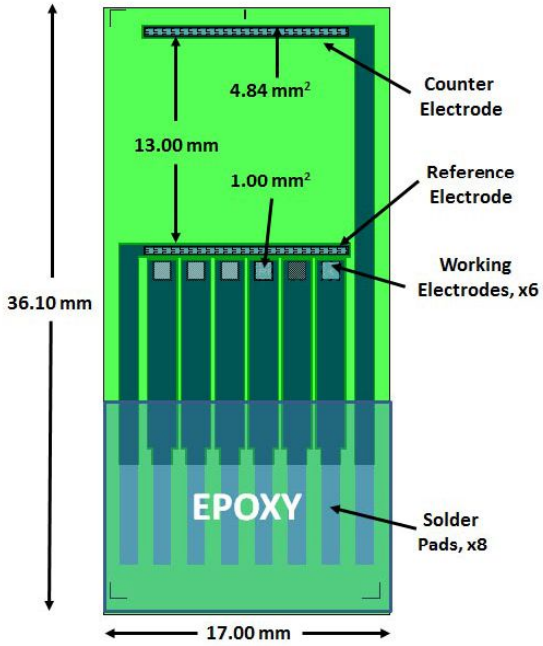

Figure 8.2: Geometrical schematic of fabricated electrodes.

8.2.3 Electrochemical Testing

The electrodes were electrochemically tested with a potentiostat via cyclic voltammetry (BioLogic) using various working electrodes (Pt, Al, LCO, LMNO, LNP) and

Table 8.1: Sputtered thin-film battery cathode material thicknesses.

Film	Thickness (nm)
$LiCoO_2$	668
$LiMn_{1.5}Ni_{0.5}O_4$	826
$LiNiPO_4$	273

the on-chip lithium counter and reference electrodes. CVs were conducted at 100 mV/s at room temperature in a electrolyte composted of 1 M $LiPF_6$ in ethylene carbonate:dimethylcarbonate 1:1 by volume.

8.3 $LiCoO_2$

8.3.1 $LiCoO_2$ EDX Characterization

EDX analysis of the elemental composition of the $LiCoO_2$ target and sputtered films is shown in Table 8.2. The composition of the target was fairly close to expected, with the biggest impurity being carbon at 15 at%, likely from the carbon tape below the sample used during EDX measurement. The sputtered film had the cobalt and oxgen contents in the correct ratio, 2:1, however, other unexpected elements were present such as chrome and nickel at 15.6 and 2.0 at%, respectively. The 15.3 at.% of platinum is likely due to the base layer itself, which is only shown through a non-uniform coverage of the $LiCoO_2$ film. The origin of the 8.0 at% carbon is unknown. From this analysis, we

can conclude that the film was not sputtered uniformly onto the platinum base layer and with other metal contamination.

Table 8.2: Elemental Atomic % of the $LiCoO_2$ target and sputtered films as measured by EDX.

Element	Actual Target	Ideal Target	Actual Film	Ideal Film
Co	23.3	30.0	19.3	33.0
O	61.5	70.0	39.7	66.0
C	15.3	0	8.0	0
Cr	0	0	15.6	0
Ni	0	0	2.0	0
Pt	0	0	15.3	0

8.3.2 $LiCoO_2$ Raman Characterization

Raman spectra of sputtered $LiCoO_2$ films as a function of oxygen percent and anneal temperature are shown in Fig 8.3 and Fig. 8.4, respectively. There are four strong raman peaks around 482, 523, 593, and 689 cm^{-}1, with some variation in wavenumber and intensity with annealing temperature and sputter O_2% content. From previous work [71], it is seen that the modes at 482 and 593 cm^{-1} are from the $LiCoO_2$ vibration modes while the mode at 691 cm^{-1} is due to an unwanted Co_3O_4 phase. This phase may exist because of low Li content in the film. A fourth mode at 523 cm^{-1} is likely due to the substrate or Pt thin film itself. The highest quality $LiCoO_2$ film sputtered with 0% O_2

and annealed at 500 °C, is shown in Fig. 8.5.

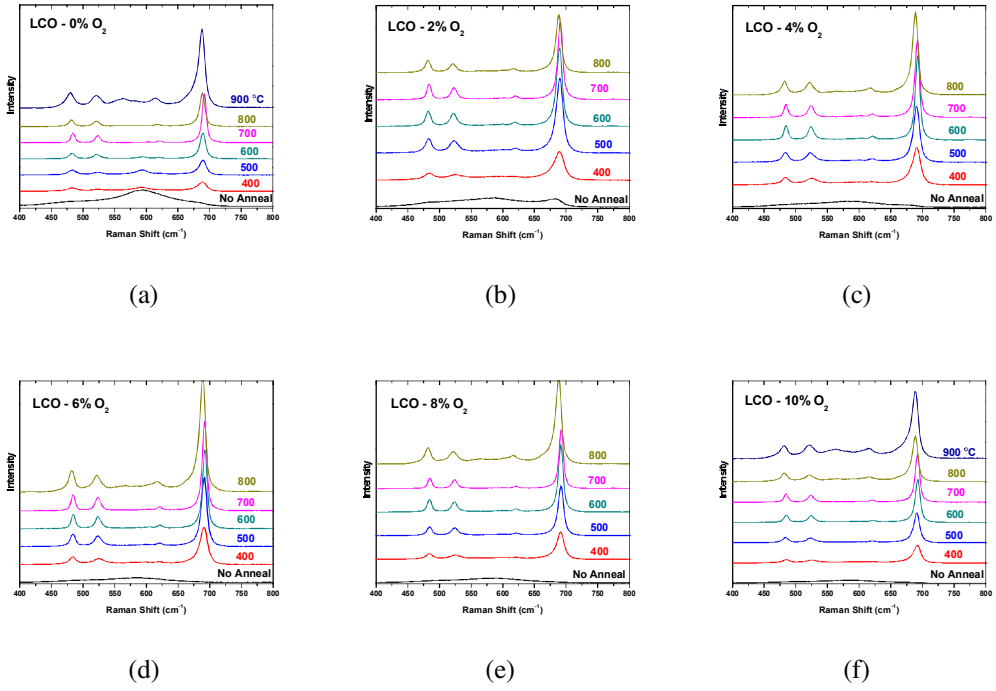

Figure 8.3: Raman spectra of $LiCoO_2$ thin-films annealed at various temperatures and sputtered with (a) 0%, (b) 2%, (c) 4%, (d) 6%, (e) 8%, (f) 10% O_2 and argon gas mixtures.

8.4 $LiMn_{1.5}Ni_{0.5}O_4$

8.4.1 $LiMn_{1.5}Ni_{0.5}O_4$ EDX Characterization

EDX analysis of the elemental composition of the $LMn_{1.5}Ni_{0.5}O_4$ target and sputtered films is shown in Table 8.3. The composition of the target was fairly close with atomic percent of nickel and oxygen, however, the maganese was deficient by nearly a factor of two (12.4 at.% vs 23.0 at.%). The large amount of carbon was likely due to

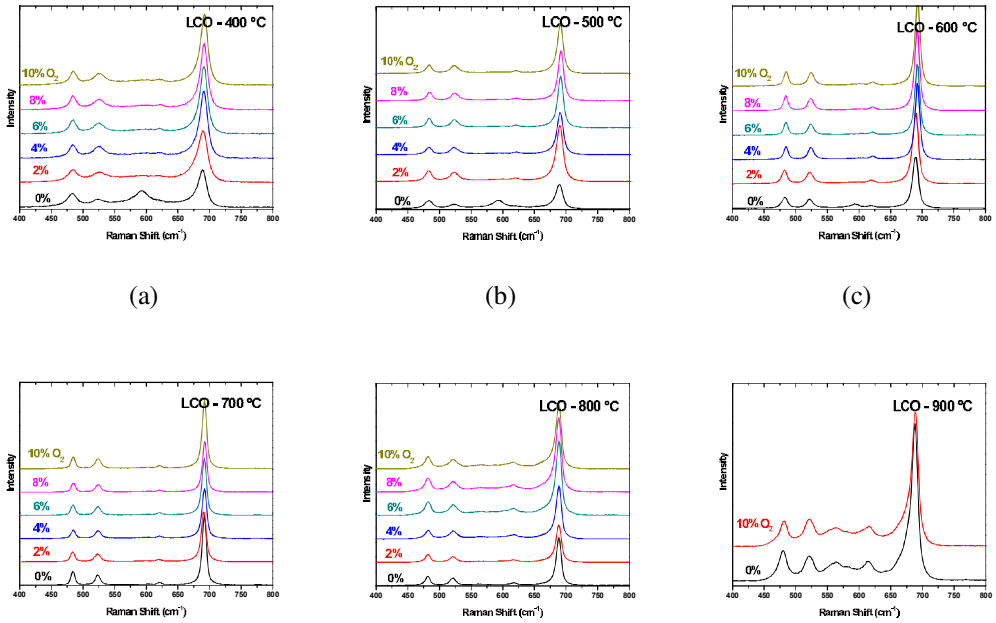

Figure 8.4: Raman spectra of $LiCoO_2$ thin-films sputtered with various contents of O_2 and argon gas mixtures and annealed at (a) 400 °C, (b) 500 °C, (c) 600 °C, (d) 700 °C, (e) 800 °C, (f) 900 °C.

the carbon tape on the sample substrate holder. The sputtered film showed >10 at.% chromium, cobalt and platinum. The platinum would be expected from the base layer, but chrome and cobalt were unexpected and the sources are unknown. The elemental at.% for maganese, nickel and oxygen were 9.9, 3.8 and 49.8 at.%, respectively. This is closer to a $Li_xMn_{1.5}Ni_{0.5}O_5$ type film, the excess oxygen likely coming from the chromium and cobalt impurities.

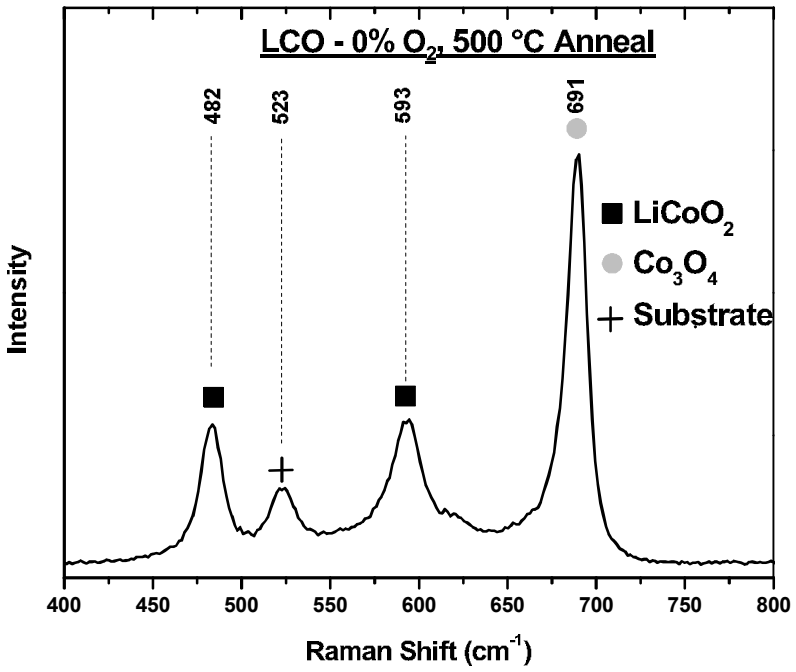

Figure 8.5: Raman spectra for highest quality $LiCoO_2$ film sputtered with 0% O_2 and annealed at 500 °C.

8.4.2 $LiMn_{1.5}Ni_{0.5}O_4$ Raman Characterization

Raman spectra of sputtered $LiMn_{1.5}Ni_{0.5}O_4$ films as a function of oxygen percent and anneal temperature are shown in Fig 8.6 and 8.7, respectively. There are very broad peaks from ca. 450 - 700 cm^{-1}, signifying that these films are not well crystallized. Again, this may be due to the cobalt or chrome impurities discussed above which may disrupt the spinel structure. However, the broad peaks agree well with previous work [72]. The vibration assignments are shown in Fig. 8.8 for the highest quality $LiMn_{1.5}Ni_{0.5}O_4$ film sputtered with 4% O_2 and annealed at 900 °C.

Table 8.3: Elemental Atomic % of the $LiMn_{1.5}Ni_{0.5}O_4$ target and sputtered films as measured by EDX.

Element	Actual Target	Ideal Target	Actual Film	Ideal Film
Mn	12.4	23.0	9.9	25.0
Ni	4.9	7	3.8	8.3
O	63.0	70.0	49.8	66
C	19.8	0	0	0
Cr	0	0	12.4	0
Co	0	0	11.6	0
Pt	0	0	10.8	0

8.5 $LiNiPO_4$

8.5.1 $LiNiPO_4$ EDX Characterization

EDX analysis of the elemental composition of the $LiNiPO_4$ target and sputtered films is shown in Table 8.4. The composition of the target was fairly close to expected, with the biggest impurity being carbon at 13.2 at.%, likely from the carbon tape below the sample used during EDX measurement. The sputtered film apparently did not have good adhesion to the Pt base film, evident fromt the lack of nickel or phosphorus showing in the EDX. This is not too suprising since nickel is the only metallic element in this target and will not form an alloy or bond with platinum easily. An alternative method to obtain adequate adhesion will need to be found.

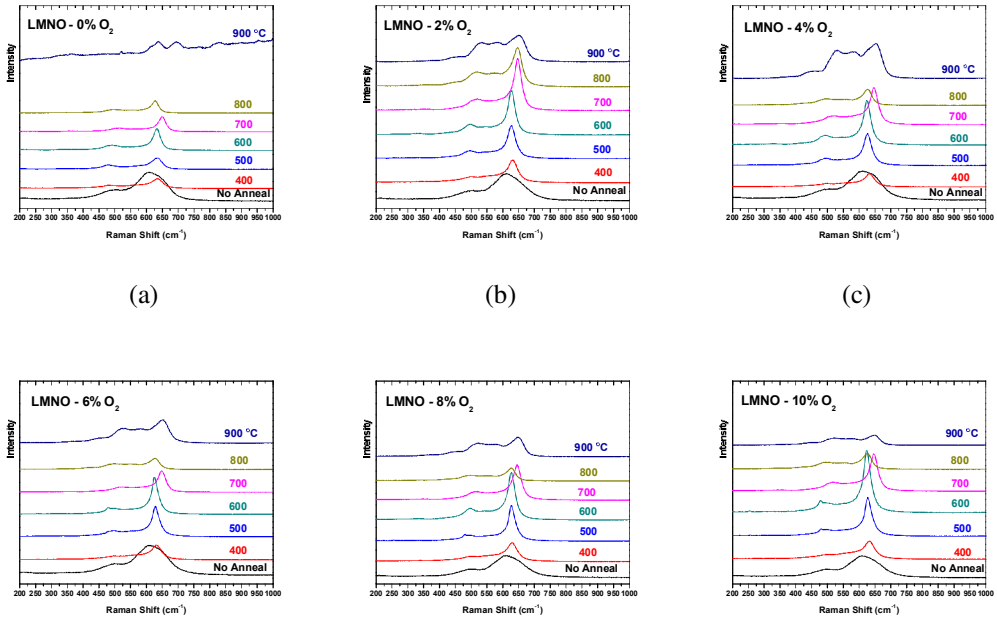

Figure 8.6: Raman spectra of $LiMn_{1.5}Ni_{0.5}O_4$ thin-films annealed at various temperatures and sputtered with (a) 0%, (b) 2%, (c) 4%, (d) 6%, (e) 8%, (f) 10% O_2 and argon gas mixtures.

Table 8.4: Elemental Atomic % of the $LiNiPO_4$ target and sputtered films as measured by EDX.

Element	Actual Target	Ideal Target	Actual Film	Ideal Film
Ni	15.5	15.0	0	16.6
O	54.3	70	18.2	66.7
P	15.6	15.0	0	16.6
C	13.2	0	25.5	0
Pt	0	0	56.3	0

8.5.2 $LiNiPO_4$ Raman Characterization

Raman spectra of sputtered $LiNiPO_4$ films as a function of oxygen percent and

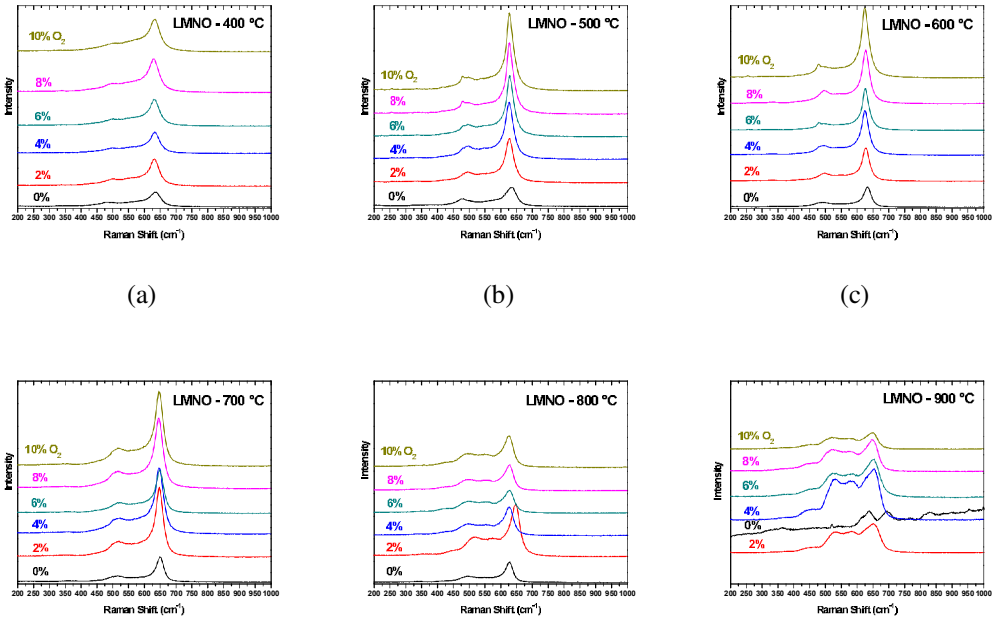

Figure 8.7: Raman spectra of $LiMn_{1.5}Ni_{0.5}O_4$ thin-films sputtered with various contents of O_2 and argon gas mixtures and annealed at (a) 400 °C, (b) 500 °C, (c) 600 °C, (d) 700 °C, (e) 800 °C, (f) 900 °C.

anneal temperature are shown in Fig 8.9 and 8.11, respectively. The evident peaks are probably from impurities because the $LiNiPO_4$ film likely was not present in many of these spectra.

8.6 Electrode Electrochemical Testing

The thin-film cathode materials were tested by cyclic voltammetry, shown in Fig. 8.11a. As expected from the raman data, LMNO was the most electrochemically active thin-film, showing a clear charge and discharge redox, however, the peaks were either not clear or at shifted potentials. The high sweep rate used, 100 $mV \cdot sec^{-1}$, could explain

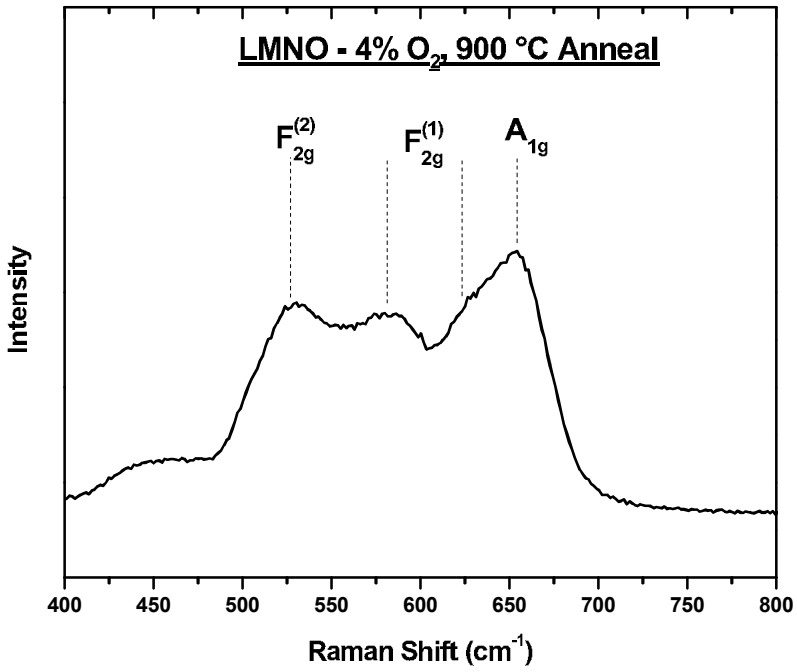

Figure 8.8: Raman spectra for highest quality $LiMn_{1.5}Ni_{0.5}O_4$ film sputtered with 4% O_2 and annealed at 900 °C.

this shift in potential. The LCO and LNP films did not show much redox behavoir, likely since LCO had the wrong phase as indicated by Raman, and LNP did not appear to adhere to the substrate properly. The CVs for aluminum and platinum are also shown in Fig. 8.11b and Fig. 8.11c, respectively. It is useful to have aluminum as a test working electrode since this is a commonly used current collector material. Platinum is also useful for evaluating the potential window of the electrolyte under study since this metal is highly oxidation resistant.

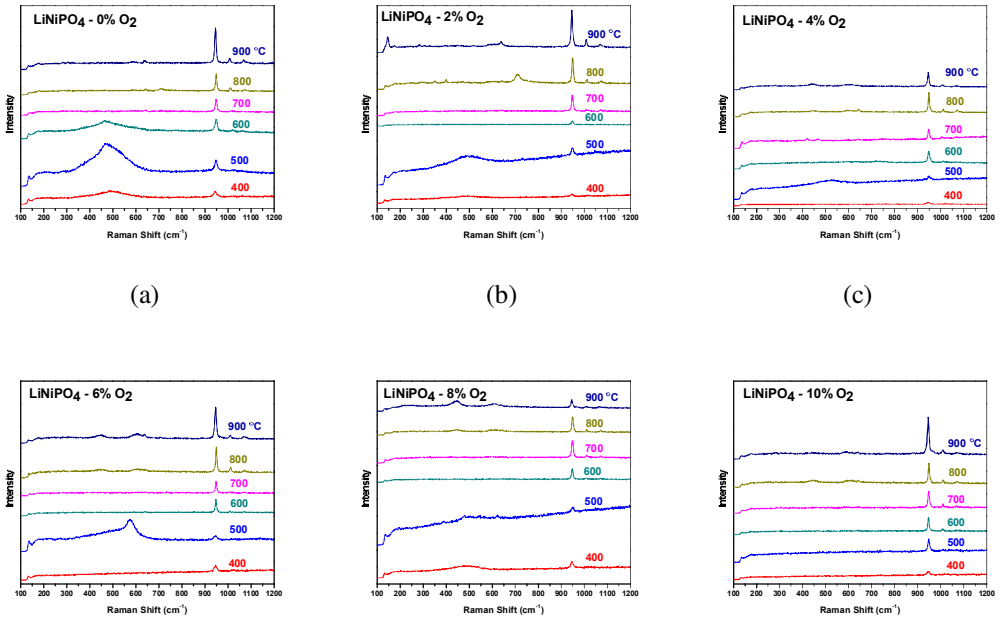

Figure 8.9: Raman spectra of $LiNiPO_4$ thin-films annealed at various temperatures and sputtered with (a) 0%, (b) 2%, (c) 4%, (d) 6%, (e) 8%, (f) 10% O_2 and argon gas mixtures.

8.7 Conclusion

A thin-film electrode for rapid analysis of Li-Ion battery materials and electrolytes has been fabricated and analyzed. $LiCoO_2$, $LiMn_{1.5}Ni_{0.5}O_4$, and $LiNiPO_4$ thin-film cathodes were sputtered and analyzed by EDX and raman spectroscopy. It was found that all three films have forms of contamination and were not properly crystallized into their proper phases. LCO showed a high degree of Co_3O_4 phase and LMNO, which having the correct phase, was not highly crystallized as seen from the broad peaks of the raman spectra. LNP films seemed to have an adhesion issue to the platinum base film. Improvements in this electrode fabrication will surely help and the electrode should

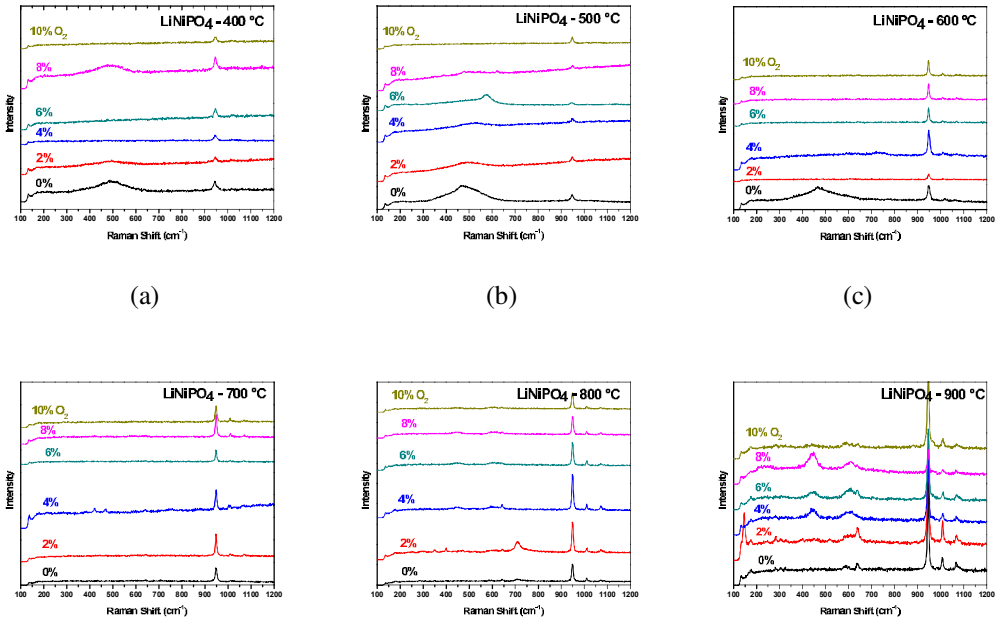

Figure 8.10: Raman spectra of $LiNiPO_4$ thin-films sputtered with various contents of O_2 and argon gas mixtures and annealed at (a) 400 °C, (b) 500 °C, (c) 600 °C, (d) 700 °C, (e) 800 °C, (f) 900 °C.

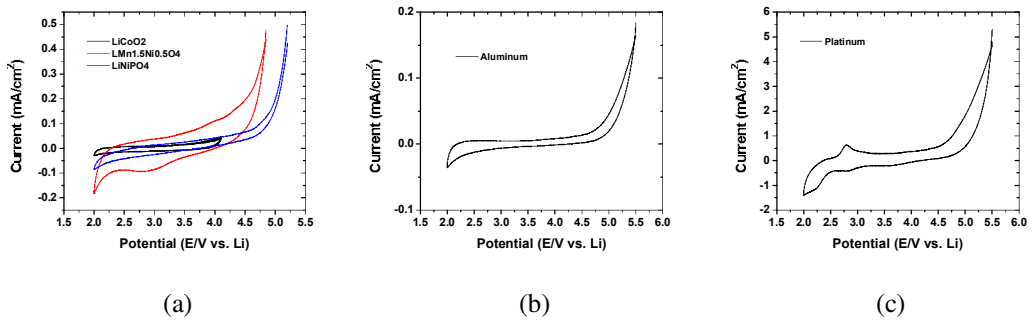

Figure 8.11: Cyclic voltammetry of (a) Li-ion thin film cathodes, (b) aluminum and (c) platinum electrodes with a 100 $mV \cdot sec^{-1}$ sweep rate in 1 M $LiPF_6$ in EC:DMC 1:1 electrolyte at room temperture.

prove to be a very useful tool in evaluating battery electrolyte and electrode materials.

Chapter 9

Electrodeposition of Titanium from Compressed Gas Solvent Based Electrolytes

The electrochemical deposition of titanium is attempted from a compressed gas solvent based electrolyte using difluoromethane. Although no titanium was found to be depositied, thought to be due to simultaneous reduction of the electrolyte salt and simultaneous chemical etching, it is thought using difluoromethane as a solvent may soon lead to promising results.

9.1 Introduction

Electrodeposition of metals has a wide range of applications from decorative purposes to electronic and semiconductor technologies. A primary focus of electrodeposition research focuses on replacing expensive metals such as chromium and nickel as plating metals for anti-corrosion coatings. Ideal metal replacements include titanium, aluminum and tungsten since these are low-cost, abundant and have excellent corrosion resistance. However, the narrow potential window (ca. 1.23 V) and passivation effects of water makes these metals impossible to plate using traditional aqueous plating solutions [16].

There has been much interest in plating metals in non-aqueous solutions and some success has been found in electroplating of aluminum [73, 74]. However, there has been little success with electrodeposition of titanium since the reduction potential of common titanium salts is well below the reduction potential of conventional solvents. Titanium has been successfully electrodeposited using molten salt electrolytes [75, 76], which is not a commercially viable option. More recently, the electrodeposition of titanium in solvent-free ionic liquids has been attempted [16, 77] from the titanium tetrachloride precursor (Ti(IV)Cl_4), however, it appears this method encounters problems involving the poor solubility of the Ti(III)Cl_3 intermediate.

The use of ionic liquids for titanium electrodeposition is necessitated by the fact that solvents will be reduced prior to titanium deposition at such low potentials. As has been seen in Chapter 2, fluorinated compressed gas solvents offer exceptionally low reduction potentials. Using these novel solvents could potentially improve titanium

electrodeposition three-fold:

1. Increase solubility of Ti(III)Cl_3 intermediate
2. Increased mass transfer through lower viscosity electrolyte
3. Lower cost by significantly lower usage of ionic liquids
4. Lower amount of ionic liquids means less competing and more efficient reduction reaction
5. No source of oxygen to passivate a deposited titanium layer

Here, we attempt electrodeposition of titanium using the same titanium precursor $TiCl_4$ and an ionic liquid, both solubilized in the fluorinated compressed gas solvent difluoromethane.

9.2 Experimental

Difluoromethane (DFM, 99.9%) was purchased from Synquest Laboratories, 1-Ethyl-3-methylimidazolium bis(trifluoromethylsulfonyl)imide (EMITFSI, 97%) was purchased from Covallent Associates and titanium precursor titanium tetrachloride ($TiCl_4$, 99%) was purchased from Sigma-Aldrich and stored under argon atmosphere. Glass slides sputter deposited with platinum, with a chromium adhesion layer, were used as working and counter electrodes while lithium metal was used as reference electrode. As described in Chapter 7, lithium metal is compatible with difluoromethane solvent and there is no evidense of reduction of this solvent at its surface. The platinum electrodes were lightly roughened with 2400 grit sand paper to improve deposition at crystal defect

locations to help seed electrodeposition [78], and washed clean with solvents. The electrodes were soldered to wires which were attached to an electrical high-pressure feed through (Conax Technologies). The electrodes, 0.1 M $TiCl_4$ and 0.1 M EMITFSI were then inserted into a larger stainless steel 316 cell and sealed shut under argon atmosphere. Vacuum was then briefly pulled on the cell through a valve and subsequently cooled to ca. -60 °C. Difluoromethane solvent was then introduced into the cell in gaseous form by evaporation from a pressurized liquid state at room temperature, which was then condensed back to a liquid state inside the cooled cell. After solvent filling, the valve was again shut and the cell was allowed to warm to room temperature. The cell mass was measured before and after solvent filling to verify the cell was completely filled with liquid solvent. After electrodepostion experiments, the cell was opened and the electrodes washed thoroughly with ethanol and dried. SEM and EDX measurements were made with a Phillips XL30 ESEM with an Oxford EDX attachment

9.3 Results and Discussion

To first evaluate the reduction potentials of the solvent, ionic liquid, and $TiCl_4$ precursor, cyclic voltammetry was performed. Two cyclic voltammetry curves are shown in Fig. 9.1 for 0.1M EMITFSI in difluoromethane with and without the addition of 0.1 M $TiCl_4$. The reduction of the electrolyte without addition of $TiCl_4$ shows two peaks. The first reduction at 1.1 V vs. Li matches well with the previously determined reduction of the the EMI^+ cation [51, 52]. The second reduction at around -0.3 V vs. Li is attributed

to the bulk reduction of the difluoromethane solvent. With the addition of 0.1 M $TiCl_4$ to this electrolyte, there are many new peaks associated with the reduction of the Ti(IV). Fig. 9.1 is in good agreement to previous work in chloride melts and ionic liquids [75, 77, 79], however, the use of difluoromethane solvent enables much higher mass transfer and currents about ten times higher are shown at the same concentration of $TiCl_4$ and the same sweep rate from an earlier study [77]. As a result, peaks are well dissolved and finer features may be determined. It is hypothesized the peaks may correspond as follows:

1. Ti(IV) + $2e^-$ $\rightarrow$ Ti(II), 1.78 V
2. Ti(IV) + e^- $\rightarrow$ Ti(III), 1.55 V
3. Ti(III) + e^- $\rightarrow$ Ti(II), 1.47 V
4. Ti(II) + $2e^-$ $\rightarrow$ Ti, 0.81 V (Underpotential Deposition)
5. Ti(II) + $2e^-$ $\rightarrow$ Ti, 0.71 V (Overpotential Depostion)
6. Reduction of EMI^+ cation, -0.47 V
7. Reduction of difluoromethane solvent, -0.55 V
8. Ti $\rightarrow$ Ti(II) + $2e^-$, 1.01 V
9. Ti(II) $\rightarrow$ Ti(IV) + $2e^-$, 1.74 V
10. Ti(III) $\rightarrow$ Ti(IV) + e^-, 1.92 V

It is fairly well understood that Ti(IV) may be reduced directly to Ti(II) through a two electron transfer step [77], which may be attributed to peak 1. Peak 2 may be attributed to the reduction of Ti(IV) to Ti(III), which has been reported to be a low solubility product that may deposit onto the electrode, corresponding to the sharp decline

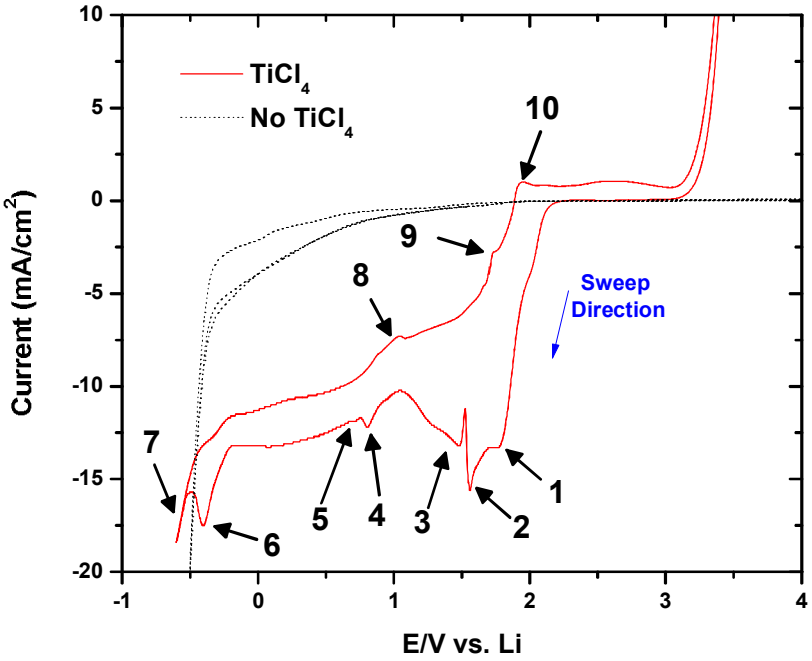

Figure 9.1: Cyclic voltammetry curves of 0.1 M EMITFSI in difluoromethane with and without 0.1 M $TiCl_4$ at 20 °C. Scan rate was 10 $mV \cdot sec^{-1}$ with platinum working and counter electrodes and a lithium metal reference.

in current immediately after this peak has been passed on the sweep. The resolubility of Ti(III) as it is reduced to Ti(II) could account for the sharp rise back up to peak 3. The underpotential deposition at peak 4 located at 0.81 V is followed immediately by the overpotential deposition at peak 5 at 0.71 V. At the overpotential point, there are multiple competing reductions taking place associated with Ti(IV), Ti(III), Ti(II) as well as the EMI^+ cation and so it is unclear whether significant titanium deposition is taking place. It is clear the EMI^+ cation reduction is the only undesired process at these potentials as the other titanium species would all eventually reduce to Ti metal. Therefore, it would be desirable to use a metal cation such as Li^+ or Na^+ to extend the reduction window by

about 1 V and allow for titanium deposition.

It was evident through additional trials that there was a difference when the salt (EMITFSI) and titanium precursor ($TiCl_4$) were mixed together prior to the solvent (difluoromethane) introduction and when they were not. An additional cyclic voltammogram is shown in Fig. 9.2 where the two were each held in seperate glass vials and only mixed when difluoromethane was introduced into the cell and solubilized both compounds. In this instance, the high cathodic current is reduced after the first cycle. It is thought that it is possible iron has been leached out of the stainless steel by the intimate contact of $TiCl_4$ with the cell in the earlier case, leading to the high cathodic currents by possible reduction of the resulting Fe complex. In the later case when $TiCl_4$ is contained in a glass vial, no leaching can occur and the peaks are much cleaner. In addition, there are clear plating and stripping peaks around 1.25 and 1.75 V. At around -0.3 V vs. Li, there appears to be the UPD and OPD of titanium. Similar to before, no titanium was seen after holding at this potential for an hour.

9.4 Conclusions

Electroplating of titanium metal onto a platinum thin-film was attempted in difluoromethane using EMITFSI as salt. While no plated titanium was observed, it was determined that the solvent itself has a low enough reduction potential to allow for the plating, as opposed to traditional solvents. It appears the EMI^+ is being reduced prior to titanium plating, which could introduce complications in Ti adhesion to the film. Lastly,

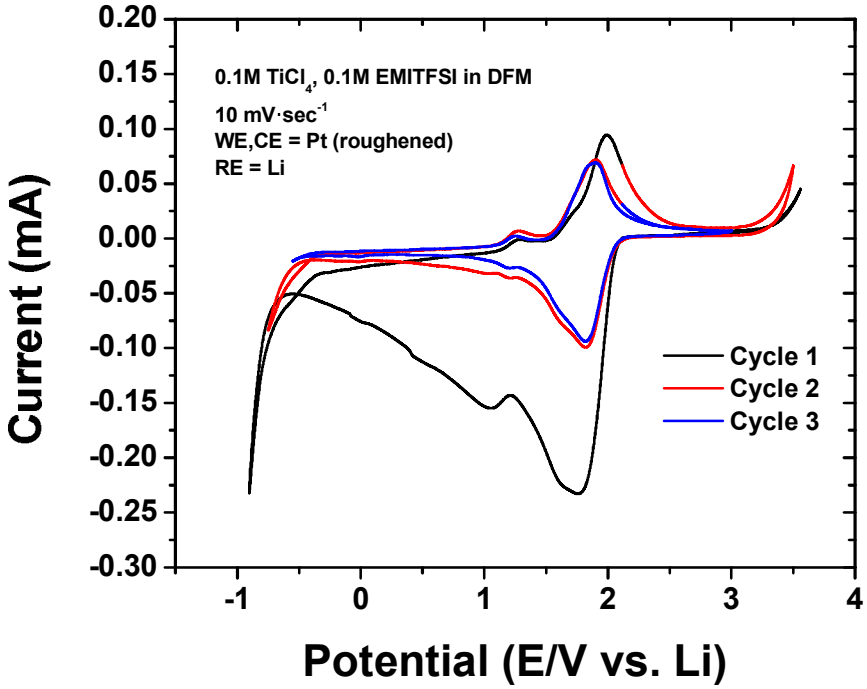

Figure 9.2: Cyclic voltammetry curves of 0.1 M EMITFSI in difluoromethane and 0.1 M $TiCl_4$ at 20 °C. The salt and titanium precursor in this instance were not mixed until after introduction of difluoromethane solvent.

issues of iron leaching out from the stainless steel cell might also bring complications to this plating method. Additional work will be needed to demonstrate electrodeposition of titanium is possible in this medium.

Appendix A

Final notes

While the fluorinated compressed gas based electrolytes explored here show promising data, a number of other possibilities have yet to be explored. Particularly, the use of difluoromethane as a solvent for lithium ion batteries looks promising as it is seen to have a reduction potential lower than that of lithium metal and an oxidation potential of >5.5 V vs. Li. However, the solubility of the Li^+ cation in this solvent is seen to be very poor. Future work might include the use of anion and/or cation receptors to increase the solubility lithium based salts in difluoromethane, such as boron based anion receptors or crown ether cation receptors.

Further, the use of ammonia (NH_3) as a compressed gas electrolyte, or liquid electrode, offers intriguing possibilities. Ammonia has a unique ability to solvate electrons, which gives it the ability to solubilize a number of metals, notably metallic lithium. These types of solutions are both electrically and ionically conductive and hold a large quantity of charge (electron and ionic charge), which are highly desirable properties in battery

electrode technology. However, the problem most obvious with using ammonia as a liquid electrode is its high electrical conductivity, which would short to the opposite electrode upon contact. Similarly, the use of ammonia as an electrolyte between an anode and cathode would short the two electrodes. A thin barrier, similar to a solid electrolyte interphase, such as a solid electrolyte like LiPON, would be required on any solid electrodes with use of ammonia as an electrode or electrolyte.

Bibliography

[1] M Saiful Islam and Craig AJ Fisher. Lithium and sodium battery cathode materials: computational insights into voltage, diffusion and nanostructural properties. *Chemical Society Reviews*, 43(1):185–204, 2014.

[2] Max Lu, Francois Beguin, and Elzbieta Frackowiak. *Supercapacitors: materials, systems and applications*. John Wiley & Sons, 2013.

[3] Kang Xu. Whether ec and pc differ in interphasial chemistry on graphitic anode and how. *Journal of the Electrochemical Society*, 156(9):A751–A755, 2009.

[4] Cynthia D Holcomb, JW Magee, JL Scott, WM Haynes, and SL Outcalt. Selected thermodynamic properties for mixtures of r-32 (difluoromethane), r-125 (pentafluoroethane), r-134a (1, 1, 1, 2-tetrafluoroethane), r-143a (1, 1, 1-trifluoroethane), r-41 (fluoromethane), r-290 (propane), and r-744 (carbon dioxide). technical note. Technical report, National Inst. of Standards and Technology, Boulder, CO (United States). Physical and Chemical Properties Div., 1997.

[5] Reiner Tillner-Roth and Akimichi Yokozeki. An international standard equation of state for difluoromethane (r-32) for temperatures from the triple point at 136.34 k to 435 k and pressures up to 70 mpa. *Journal of Physical and Chemical Reference Data*, 26(6):1273–1328, 1997.

[6] Xiao-long Cui, Guang-ming Chen, Xiao-hong Han, and Qin Wang. Experimental vapor pressure data and a vapor pressure equation for fluoroethane (hfc-161). *Fluid phase equilibria*, 245(2):155–157, 2006.

[7] Dana R Defibaugh and Graham Morrison. Compressed liquid densities, saturated liquid densities, and vapor pressures of 1, 1-difluoroethane. *Journal of Chemical & Engineering Data*, 41(3):376–381, 1996.

[8] Graham Morrison and David K Ward. Thermodynamic properties of two alternative refrigerants: 1, 1-dichloro-2, 2, 2-trifluoroethane (r123) and 1, 1, 1, 2-tetrafluoroethane (r134a). *Fluid Phase Equilibria*, 62(1):65–86, 1991.

[9] Csid:9483, http://www.chemspider.com/chemical-structure.9483.html (accessed 02:15, apr 13, 2015).

[10] Seung-Yul Lee, Kazuhide Ueno, and C Austen Angell. Lithium salt solutions in mixed sulfone and sulfone-carbonate solvents: A walden plot analysis of the maximally conductive compositions. *The Journal of Physical Chemistry C*, 116(45):23915–23920, 2012.

[11] Alar Jänes and Enn Lust. Use of organic esters as co-solvents for electrical double layer capacitors with low temperature performance. *Journal of Electroanalytical Chemistry*, 588(2):285–295, 2006.

[12] Doron Aurbach. *Nonaqueous electrochemistry*. CRC Press, 1999.

[13] Erik J Brandon, William C West, Marshall C Smart, Gleb Yushin, Yair Korenblit, Adam Kajdos, Alexander Kvit, and Jacek Jagiello. Low temperature double-layer capacitors with improved energy density: An overview of recent development efforts. 2012.

[14] Thomas Reddy. *Handbook of batteries*. McGraw-Hill Pub., 2002.

[15] Makoto Ue. Mobility and ionic association of lithium and quaternary ammonium salts in propylene carbonate and γ-butyrolactone. *Journal of the electrochemical society*, 141(12):3336–3342, 1994.

[16] Frank Endres, Douglas MacFarlane, and Andrew Abbott. *Electrodeposition from ionic liquids*. John Wiley & Sons, 2008.

[17] CM Julien and A Mauger. Review of 5-v electrodes for li-ion batteries: status and trends. *Ionics*, 19(7):951–988, 2013.

[18] Dae Hoe Lee, Jing Xu, and Ying Shirley Meng. An advanced cathode for na-ion batteries with high rate and excellent structural stability. *Physical Chemistry Chemical Physics*, 15(9):3304–3312, 2013.

[19] Nikhilendra Singh, Timothy S Arthur, Chen Ling, Masaki Matsui, and Fuminori Mizuno. A high energy-density tin anode for rechargeable magnesium-ion batteries. *Chem. Commun.*, 49(2):149–151, 2012.

[20] N Jayaprakash, Shyamal K Das, and Lynden A Archer. The rechargeable aluminum-ion battery. *Chemical Communications*, 47(47):12610–12612, 2011.

[21] O Barbieri, M Hahn, A Herzog, and R Kötz. Capacitance limits of high surface area activated carbons for double layer capacitors. *Carbon*, 43(6):1303–1310, 2005.

[22] Brian E Conway. Electrochemical supercapacitors. 1999.

[23] T Richard Jow, Kang Xu, Oleg Borodin, and Makoto Ue. *Electrolytes for lithium and lithium-ion batteries*, volume 58. Springer, 2014.

[24] Emanuel Peled. The electrochemical behavior of alkali and alkaline earth metals in nonaqueous battery systems—the solid electrolyte interphase model. *Journal of The Electrochemical Society*, 126(12):2047–2051, 1979.

[25] Rosamaria Fong, Ulrich von Sacken, and JR Dahn. Studies of lithium intercalation into carbons using nonaqueous electrochemical cells. *Journal of The Electrochemical Society*, 137(7):2009–2013, 1990.

[26] Fritz London. The general theory of molecular forces. *Trans. Faraday Soc.*, 33:8b–26, 1937.

[27] Gianfranco Pistoia, Mario De Rossi, and Bruno Scrosati. Study of the behavior of ethylene carbonate as a nonaqueous battery solvent. *Journal of The Electrochemical Society*, 117(4):500–502, 1970.

[28] P Kirsh. Modern fluoroorganic chemistry. *Synthesis, Reactivity, Applications*, 2004.

[29] Li Yang, Boris Ravdel, and Brett L Lucht. Electrolyte reactions with the surface of high voltage lini0. 5mn1. 5o4 cathodes for lithium-ion batteries. *Electrochemical and Solid-State Letters*, 13(8):A95–A97, 2010.

[30] Energy Efficiency and Renewable Energy. Multi-year program plan. 2010.

[31] Kichiro Kato, Kohei Igarashi, Michihiko Masuda, Katsuji Otsubo, Akio Yasuda, Keiso Takeda, and Toru Sato. Development of engine for natural gas vehicle. Technical report, SAE Technical Paper, 1999.

[32] Zhengcheng Zhang, Libo Hu, Huiming Wu, Wei Weng, Meiten Koh, Paul C Redfern, Larry A Curtiss, and Khalil Amine. Fluorinated electrolytes for 5 v lithium-ion battery chemistry. *Energy Environ. Sci.*, 6(6):1806–1810, 2013.

[33] R Kötz and M Carlen. Principles and applications of electrochemical capacitors. *Electrochimica Acta*, 45(15):2483–2498, 2000.

[34] Makoto Ue, Kazuhiko Ida, and Shoichiro Mori. Electrochemical properties of organic liquid electrolytes based on quaternary onium salts for electrical double-layer capacitors. *Journal of the Electrochemical Society*, 141(11):2989–2996, 1994.

[35] Makoto Ue, Masayuki Takeda, Masahiro Takehara, and Shoichiro Mori. Electrochemical properties of quaternary ammonium salts for electrochemical capacitors. *Journal of The Electrochemical Society*, 144(8):2684–2688, 1997.

[36] John R Scully, David C Silverman, and Martin W Kendig. *Electrochemical impedance: analysis and interpretation*. Number 1188. ASTM International, 1993.

[37] J Braunstein and GD Robbing. Electrolytic conductance measurements and capacitive balance. *Journal of Chemical Education*, 48(1):52, 1971.

[38] Gregoire Herzog, Waleed Moujahid, Karen Twomey, Conor Lyons, and Vladimir I Ogurtsov. On-chip electrochemical microsystems for measurements of copper and conductivity in artificial seawater. *Talanta*, 116:26–32, 2013.

[39] Michael Freemantle. *An introduction to ionic liquids*. Royal Society of chemistry, 2010.

[40] MJ Atkinson. Fast-response oxygen sensor for a free-fall ctd. *Limnology and Oceanography*, 33(1):141–145, 1988.

[41] MJ Atkinson, FIM Thomas, N Larson, E Terrill, K Morita, and CC Liu. A microhole potentiostatic oxygen sensor for oceanic ctds. *Deep Sea Research Part I: Oceanographic Research Papers*, 42(5):761–771, 1995.

[42] Maciej Sosna, Guy Denuault, Robin W Pascal, Ralf D Prien, and Matt Mowlem. Development of a reliable microelectrode dissolved oxygen sensor. *Sensors and Actuators B: Chemical*, 123(1):344–351, 2007.

[43] Walt Boyes. *Instrumentation reference book*. Butterworth-Heinemann, 2009.

[44] Dongming He, Mark A Shannon, and Norman R Miller. Micromachined silicon electrolytic conductivity probes with integrated temperature sensor. *Sensors Journal, IEEE*, 5(6):1185–1196, 2005.

[45] Bela G Liptak. *Analytical instrumentation*. CRC Press, 1994.

[46] Erik J Brandon, William C West, Marshall C Smart, Larry D Whitcanack, and Gary A Plett. Extending the low temperature operational limit of double-layer capacitors. *Journal of power sources*, 170(1):225–232, 2007.

[47] Doron Aurbach, Yosef Talyosef, Boris Markovsky, Elena Markevich, Ella Zinigrad, Liraz Asraf, Joseph S Gnanaraj, and Hyeong-Jin Kim. Design of electrolyte solutions for li and li-ion batteries: a review. *Electrochimica Acta*, 50(2):247–254, 2004.

[48] Peter Tremaine and Maurice G Robinson. The static dielectric constants of the liquified fluoromethanes. *Canadian Journal of Chemistry*, 51(10):1497–1503, 1973.

[49] Andrew P Abbott and Christopher A Eardley. Conductivity of (c4h9) 4n bf4 in liquid and supercritical hydrofluorocarbons. *The Journal of Physical Chemistry B*, 104(39):9351–9355, 2000.

[50] Andrew P Abbott, Christopher A Eardley, and Richard Tooth. Relative permittivity measurements of 1, 1, 1, 2-tetrafluoroethane (hfc 134a), pentafluoroethane (hfc 125), and difluoromethane (hfc 32). *Journal of Chemical & Engineering Data*, 44(1):112–115, 1999.

[51] Aoife M O'Mahony, Debbie S Silvester, Leigh Aldous, Christopher Hardacre, and Richard G Compton. Effect of water on the electrochemical window and potential limits of room-temperature ionic liquids. *Journal of Chemical & Engineering Data*, 53(12):2884–2891, 2008.

[52] Cormac O Laoire, Edward Plichta, Mary Hendrickson, Sanjeev Mukerjee, and KM Abraham. Electrochemical studies of ferrocene in a lithium ion conducting organic carbonate electrolyte. *Electrochimica Acta*, 54(26):6560–6564, 2009.

[53] Andrew P Abbott, Christopher A Eardley, John C Harper, and Eric G Hope. Electrochemical investigations in liquid and supercritical 1, 1, 1, 2-tetrafluoroethane (hfc 134a) and difluoromethane (hfc 32). *Journal of Electroanalytical Chemistry*, 457(1):1–4, 1998.

[54] Andrew P Abbott and Christopher A Eardley. Solvent properties of liquid and supercritical 1, 1, 1, 2-tetrafluoroethane. *The Journal of Physical Chemistry B*, 102(43):8574–8578, 1998.

[55] Andrew P Abbott and Christopher A Eardley. Solvent properties of liquid and supercritical hydrofluorocarbons. *The Journal of Physical Chemistry B*, 103(13):2504–2509, 1999.

[56] Darío L Goldfarb and Horacio R Corti. Electrical conductivity of decamethylferrocenium hexafluorophosphate and tetrabutylammonium hexafluorophosphate in supercritical trifluoromethane. *The Journal of Physical Chemistry B*, 108(10):3358–3367, 2004.

[57] Ping Liu, Mark Verbrugge, and Souren Soukiazian. Influence of temperature and electrolyte on the performance of activated-carbon supercapacitors. *Journal of Power Sources*, 156(2):712–718, 2006.

[58] Bo Xu, Danna Qian, Ziying Wang, and Ying Shirley Meng. Recent progress in cathode materials research for advanced lithium ion batteries. *Materials Science and Engineering: R: Reports*, 73(5):51–65, 2012.

[59] Min Sik Park, Sang Bok Ma, Dong Joon Lee, Dongmin Im, Seok-Gwang Doo, and Osamu Yamamoto. A highly reversible lithium metal anode. *Scientific reports*, 4, 2014.

[60] Jung-Ki Park. *Principles and applications of lithium secondary batteries*. John Wiley & Sons, 2012.

[61] Wu Xu and C Austen Angell. Weakly coordinating anions, and the exceptional conductivity of their nonaqueous solutions. *Electrochemical and Solid-State Letters*, 4(1):E1–E4, 2001.

[62] Nan Shao, Xiao-Guang Sun, Sheng Dai, and De-en Jiang. Electrochemical windows of sulfone-based electrolytes for high-voltage li-ion batteries. *The Journal of Physical Chemistry B*, 115(42):12120–12125, 2011.

[63] K Reuter, S Rosenzweig, and EU Franck. The static dielectric constant of ch 3 f and chf 3 to 468 k and 2000 bar. *Physica A: Statistical Mechanics and its Applications*, 156(1):294–302, 1989.

[64] Christopher W Meyer and Graham Morrison. Dipole moments of seven refrigerants. *Journal of Chemical and Engineering Data*, 36(4):409–413, 1991.

[65] MT Barao, UV Mardolcar, and CA Nieto de Castro. Dielectric constant and dipole moments of 1, 1, 1-trifluoro-2, 2-dichloroethane (hcfc 123) and 1, 1-difluoroethane (hfc 152a) in the liquid phase. *Fluid phase equilibria*, 150:753–762, 1998.

[66] Erang Cho, Junyoung Mun, Oh B Chae, Oh Min Kwon, Hyung-Tae Kim, Ji Heon Ryu, Young Gyu Kim, and Seung M Oh. Corrosion/passivation of aluminum current collector in bis (fluorosulfonyl) imide-based ionic liquid for lithium-ion batteries. *Electrochemistry Communications*, 22:1–3, 2012.

[67] BJ Neudecker, NJ Dudney, and JB Bates. "lithium-free" thin-film battery with in situ plated li anode. *Journal of the Electrochemical Society*, 147(2):517–523, 2000.

[68] JB Bates, NJ Dudney, B Neudecker, A Ueda, and CD Evans. Thin-film lithium and lithium-ion batteries. *Solid State Ionics*, 135(1):33–45, 2000.

[69] Naoaki Kuwata, Junichi Kawamura, Keisuke Toribami, Takeshi Hattori, and Noriko Sata. Thin-film lithium-ion battery with amorphous solid electrolyte fabricated by pulsed laser deposition. *Electrochemistry Communications*, 6(4):417–421, 2004.

[70] Hui Xia, Li Lu, and Ying Shirley Meng. Growth of layered lini0. 5mn0. 5o2 thin films by pulsed laser deposition for application in microbatteries. *Applied Physics Letters*, 92(1):011912, 2008.

[71] Cheng-Lung Liao and Kuan-Zong Fung. Lithium cobalt oxide cathode film prepared by rf sputtering. *Journal of Power Sources*, 128(2):263–269, 2004.

[72] Kuppan Saravanan, Angelique Jarry, Robert Kostecki, and Guoying Chen. A study of room-temperature lixmn1. 5ni0. 5o4 solid solutions. *Scientific reports*, 5, 2015.

[73] E Peled and E Gileadi. The electrodeposition of aluminum from aromatic hydrocarbon i. composition of baths and the effect of additives. *Journal of The Electrochemical Society*, 123(1):15–19, 1976.

[74] A Brenner and CW Tobias. Advances in electrochemistry and electrochemical engineering. *Vol. 5Interscience, New York*, page 205, 1967.

[75] GM Haarberg, W Rolland, Å Sterten, and J Thonstad. Electrodeposition of titanium from chloride melts. *Journal of applied electrochemistry*, 23(3):217–224, 1993.

[76] IA Menzies, DL Hill, GJ Hills, L Young, and JO'M Bockris. The mechanism of the electrodeposition of titanium from fused salts. *Journal of Electroanalytical Chemistry (1959)*, 1(2):161–170, 1959.

[77] I Mukhopadhyay, CL Aravinda, D Borissov, and W Freyland. Electrodeposition of ti from ticl 4 in the ionic liquid l-methyl-3-butyl-imidazolium bis (trifluoro methyl sulfone) imide at room temperature: study on phase formation by in situ electrochemical scanning tunneling microscopy. *Electrochimica acta*, 50(6):1275–1281, 2005.

[78] Mordechay Schlesinger and Milan Paunovic. *Modern electroplating*, volume 55. John Wiley & Sons, 2011.

[79] E Chassaing, F Basile, and G Lorthioir. Study of ti (iii) solutions in various molten alkali chlorides. i. chemical and electrochemical investigation. *Journal of Applied Electrochemistry*, 11(2):187–191, 1981.